Meeting at the Membrane – Confined Water at Cationic Lipids & Neuronal Growth on Fluid Lipid Bilayers

Der Fakultät für Physik und Geowissenschaften
der Universität Leipzig eingereichte

DISSERTATION

zur Erlangung des akademischen Grades doctor rerum naturalium
Dr. rer. nat.
vorgelegt von

M. Sc. Lydia Woiterski

geboren am 30. Juli 1980 in Prenzlau

Gutachter:	Prof. Dr. Josef Käs
	Prof. Dr. Ben Fabry
Tag der Verleihung:	16. Dezember 2013

Bibliographische Beschreibung

Woiterski, Lydia

Meeting at the Membrane – Confined Water at Cationic Lipids & Neuronal Growth on Fluid Lipid Bilayers

Universität Leipzig, Dissertation
152 S., 330 Lit., 49 Abb., 11 Tab.

Referat:
Die Zellmembran dient der Zelle nicht nur als äußere Hülle, sondern ist auch an einer Vielzahl von lebenswichtigen Prozessen wie Signaltransduktion oder Zelladhäsion beteiligt. Wasser als integraler Bestandteil von Zellen und der extrazellulären Matrix hat sowohl einen großen Einfluss auf die Struktur von Biomolekülen, als auch selbst besondere Merkmale in eingschränkter Geometrie. Im Rahmen dieser Arbeit wurden zwei Effekte an Modellmembranen untersucht: Erstens der Einfluss des Gegenions an kationischen Lipiden (DODAX, X = F, Cl, Br, I) auf die Eigenschaften des Grenzflächenwassers und zweitens das Vermögen durch Viskositätsänderungen das Wachstum von Nervenzellen anzuregen sowie die einzelnen Stadien der Bildung von neuronalen Netzwerken und deren Optimierung zu charakterisieren.

Lipidmultischichten und darin adsorbiertes Grenzflächenwasser wurden mittels Infrarotspektroskopie mit abgeschwächter Totalreflexion untersucht. Nach Charakterisierung von Phasenverhalten und Wasserkapazität der Lipide wurden die Eigenschaften des Wassers durch kontrollierte Hydratisierung bei einem Wassergehalt von einem Wassermolekül pro Lipid verglichen. Durch die geringe Wasserkapazität können in diesem besonderen System direkte Wechselwirkungen zwischen Lipiden und Wasser aus der ersten Hydratationsschale beobachtet werden. Bemerkenswert strukturierte OH-Streckschwingungsbanden in Abhängigkeit des Anions und niedrige IR-Ordnungsparameter zeigen, dass stark geordnete, in ihrer Mobilität eingeschränkte Wassermoleküle an DODAX in verschiedenen Populationen mit unterschiedlich starken Wasserstoffbrückenbindungen existieren und sich vermutlich in kleinen Clustern anordnen.

Die zweite Fragestellung hatte zum Ziel, das Wachstum von Nervenzellen auf Membranen zu beleuchten. Auf der Ebene einzelner Zellen wurde untersucht, ob sich in Analogie zu den bisher verwendeten elastischen Substraten, die Viskosität von Membranen als neuartiger physikalischer Stimulus dafür eignet, das mechanosensitive Verhalten von Neuronen zu modulieren. Das Wachstum der Neuronen wurde auf substrat- und polymergestützten Lipiddoppelschichten mittels Phasenkontrastmikroskopie beobachtet. Die Quantifizierung der Neuritenlängen, -auswuchsgeschwindigkeiten und -verzweigungen zeigten kaum signifikante Unterschiede. Diffusionsmessungen (FRAP) ergaben, dass entgegen der Erwartungen, die Substrate sehr ähnliche Fluiditäten aufweisen. Die Betrachtung der zeitlichen Entwicklung des kollektiven Neuronenwachstums, also der Bildung von komplexen Netzwerken, offenbarte robuste „Kleine-Welt"-Eigenschaften und darüber hinaus unterschiedliche Stadien. Diese wurden durch graphentheoretische Analyse beschrieben, um anhand typischer Größen wie dem Clusterkoeffizienten und der kürzesten Pfadlänge zu zeigen, wie sich die Neuronen in einem frühen Stadium vernetzen, im Verlauf eine maximale Komplexität erreichen und letztlich das Netzwerk durch effiziente Umstrukturierung hinsichtlich kurzer Pfadlängen optimiert wird.

d

Contents

List of Figures

List of Tables

þetta er ágætis byrjun

Sigur Rós

1. Introduction

Membranes constitute a prerequisite for life. A eukaryotic cell is enclosed by the plasma membrane which naturally helps the cell to maintain its integrity. Additionally, its location at the first front to the outside world entails an important role in many cellular processes such as signal transduction, cell adhesion and selective permeability, i.e., transport across the membrane (Lodish, 2000). In the current picture plasma membranes form a two-dimensional liquid composed of a double layer of oriented lipids, which embed transmembrane and peripheral proteins. It is basically described by the fluid mosaic model (Singer and Nicolson, 1972) and was extended by the lipid raft hypothesis (Simons and Ikonen, 1997).

Lipid molecules have an amphiphilic character, i.e., they possess a hydrophilic polar headgroup and a hydrophobic tail group. When these molecules are exposed to an aqueous phase, the non-polar hydrocarbon chains disturb the hydrogen bond network of surrounding water molecules. However, the restructuring of water molecules is entropically unfavorable – a phenomenon which is called hydrophobic effect (Tanford, 1978). Therefore, lipids self-assemble to supramolecular structures to minimize their contact with water. The most abundant lipids in biological membranes are double-chained lipids. Depending on thermodynamic and geometrical factors they self-assemble to bilayer structures like vesicles (for large headgroup areas) or planar bilayers (for small headgroup areas) (Israelachvili et al., 1976).

The complexity of eukaryotic plasma membranes results from its different building blocks and their interactions with the surrounding environment. First, biological membranes exhibit a large variety of different phospholipids, sphingolipids, cholesterol and, in the case of neural tissues, cerebrosides (Yorek, 1993; van Meer et al., 2008). Their composition is asymmetric in both bilayer leaflets and varies substantially for different species, organelles or tissues (Yorek, 1993). Second, there are several classes of membrane proteins which are associated with different functions based on their attachment to the lipid bilayer, e.g., transmembrane proteins acting as ion channels or proteins that are attached the one leaflet only and are involved in signal transduction pathways (Alberts, 2002). The structure of a biological membrane is illustrated in figure 1.1.

The plasma membrane forms the cell's boundary between the extracellular matrix

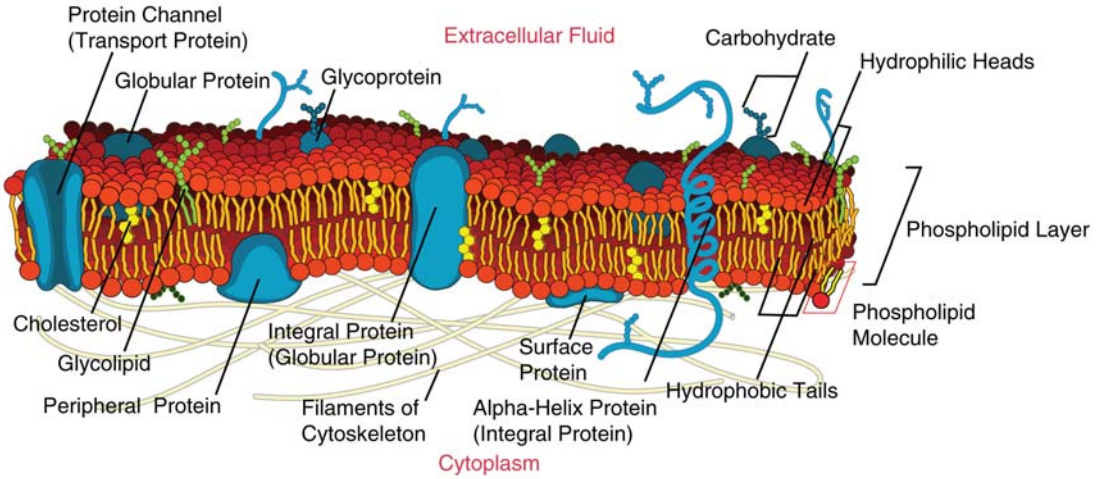

Figure 1.1.: Schematic of a plasma membrane - a two-dimensional fluid lipid bilayer with embedded membrane proteins. The membrane forms the cell's boundary to the external extracellular matrix and is linked to the internal actin cytoskeleton via complexes of transmembrane and adapter proteins (focal adhesions). Image from Wikimedia Commons.

(ECM) on the one side and the cytoplasm on the other side. These structures cannot be considered as separated entities, but can be tightly interconnected. The intracellular spectrin-actin web is coupled to the plasma membrane of red blood cell and creates a stiff cortex, which allows the cell to squeeze through tiny capillaries (Lux, 1979). Cell adhesion is orchestrated by the interplay of cell adhesion molecules/receptors, ECM proteins and cytoplasmic plaque/peripheral membrane proteins (Gumbiner, 1996). These multiprotein complexes are denoted as focal adhesions (Burridge et al., 1988). Cell adhesion receptors such as transmembrane proteins of the integrin and cadherin families mediate binding interactions at the extracellular surface and are, therefore, involved in cell-cell and cell-ECM interactions (Gumbiner, 1996). ECM proteins such as collagens, fibronectins and laminins are arranged in a complex macromolecular scaffold and can be strongly bound to the cell surface via adhesion receptors. The third component at the intracellular surface of the plasma membrane are anchor proteins (cytoplasmic plaque) and peripheral membrane proteins. They link adhesion molecules to the cytoskeleton and, thus, regulate the cytoskeletal organization, adhesions and are involved in signal transduction (Gumbiner, 1996; Alberts, 2002). The role of focal adhesion complexes in mechanosensation and -transduction will be described in section 2.2.

Both the extracellular matrix and the intracellular space contain a high fraction of water. While for the ECM a portion of 75 % - 90 % was reported (Comper and Laurent, 1978; Armstrong and Mow, 1982; The Histology Guide), water molecules contribute 70 % - 80 % to the cells' weight (Alberts, 2002; Mentré, 2012). In the last decade, the awareness of the importance of water in cell biology increased (Ball, 2008c) or to quote M. Chaplin it was recognized that "Liquid water is not a 'bit player' in the theater of life – it's the headline

act“ (Chaplin, 2006). Water has a profound impact on the structure and functioning of proteins and nucleic acids (Chaplin, 2006). Bulk water, which in the standard picture is described by fleeting hydrogen bonds (HBs) arranged in a tetrahedral network, exhibits many anomalous properties (Franks, 1972). Even more remarkably, in the vicinity of biomolecules the liquid is in part strongly confined and, therefore, displays a very different behavior from the bulk (Bhattacharyya, 2008). Thus, although the molecule is that ubiquitous and small, its comportment is so complex that “no one really understands water“, i.e., down to the present day there is no unified model which fully describes liquid water (Ball, 2008b).

The profound interactions of biomolecules and water lead to a strong ordering of the latter and certainly have a great impact on many cellular functions (Chaplin, 2006; Ball, 2008b). Reminiscing the picture of cell-cell contacts the question arises how membranes influence the behavior of neighboring cells. However, the complexity of the plasma membrane and its adjacent structures hinders the unraveling of individual factors that trigger cellular response. A remedy to this challenge was the utilization of artificial constructs like supported lipid membranes, i.e., a model lipid bilayer on a solid support, or self-assembled monolayers (SAMs) (Sackmann, 1996; Senaratne et al., 2005). The insertion of for example *single* receptor molecules in these substrates opened a new world for the investigation of cellular processes. To name a few early applications, supported bilayers (sBLs) were employed in immunological studies on membrane-mediated cell-cell communication of T-lymphocytes (McConnell et al., 1986) and cell adhesion (Chan et al., 1991; Groves et al., 2001), while SAMs were used to modulate neuronal development (Stenger et al., 1993).

A novel aspect in the utilization of lipid substrates is the study of cellular mechanosensitivity, which is the ability of cells to perceive and react on mechanical stimuli from their environment (Franze and Guck, 2010). Mechanical forces and deformations at cell-ECM contacts are converted into biochemical signals which modulates many cellular processes such as adhesion (Pelham and Wang, 1997), migration (Lo et al., 2000) and even influence stem cell differentiation (Engler et al., 2006) as reviewed in (Discher et al., 2005; Vogel and Sheetz, 2006; Geiger et al., 2009; Ladoux and Nicolas, 2012). The observed migration of cells towards stiffer substrates is called durotaxis (Lo et al., 2000), but there is evidence that not all cell types prefer a high rigidity. In brain tissue, neurons grow in close proximity to soft glial cells (Lu et al., 2006) and quantitative *in vitro* experiments showed enhanced neurite branching on soft substrates indicating an inverse durotactic behavior (Flanagan et al., 2002; Franze and Guck, 2010).

So far the mechanosensitivity has been studied using purely elastic poly(acrylic acid) (PAA) hydrogels (Pelham and Wang, 1997; Flanagan et al., 2002) as well as micropatterns

(Balaban et al., 2001) and -pillars (Tan et al., 2003; Ghibaudo et al., 2008). These substrates allow a systematic and reproducible control of the elastic properties. Their utilization in vast amount of experimental studies have lead to an enormous increase in the awareness of the importance of mechanical stimuli for a variety of cellular processes (for review see (Franze and Guck, 2010; Moore and Sheetz, 2011; Ladoux and Nicolas, 2012)). For example, cells cultured on elastic substrates of varying stiffness revealed that cell locomotion and focal adhesions are controlled by substrate rigidity (Pelham and Wang, 1997) and enabled the determination of traction forces and a colocalization of focal adhesions (Balaban et al., 2001; Beningo and Wang, 2002).

Despite this great work, it has to be noted that cells and also the extracellular matrix exhibit *viscoelastic* properties. Another point is that the hydrogels are permanently linked, while the cell's actin-cytoskeleton undergoes fast remodeling processes at the time scale of several minutes (Svitkina et al., 1986). Therefore, lipid substrates of tunable viscoelasticity provide a more physiologic approach for the mechanical stimulation of cells and better mimic cell-cell/ECM interactions than purely elastic substrates.

While mechanosensitive response of cells on lipid bilayers rather addresses the behavior of isolated cells, one may raise the question how do neuronal networks evolve on these substrates? Understanding the development of neuronal networks and hopefully once also the brain is an attractive playground for scientists. Although it has been known since the times of Ramón y Cajal that the brain is formed by a network (Boccaletti et al., 2006; Stam and van Straaten, 2012), only in the last two decades there has been a revival of complex network studies due to the seminal works by (Watts and Strogatz, 1998) and (Albert and Barabási, 2002). Graph theoretical approaches have become a powerful tool for investigating the architecture and dynamics of complex networks (Boccaletti et al., 2006) with the aim of a deeper understanding of the intricate relation of structural and functional networks (Stam, 2010; Bullmore and Bassett, 2011; Sporns, 2011). Many real and man-made networks such as neuronal networks or the power grid of the western United States, respectively, exhibit small-world properties (Watts and Strogatz, 1998).

Scope of this thesis

Part 1: Water bound to cationic lipid membranes

The first goal of this study is elucidating the interactions of water near lipid membranes with infrared spectroscopy. Depending on the phase state, phospholipid membranes bind between 6 and 30 water molecules per lipid at full hydration (Nagle and Tristram-Nagle, 2000; Gauger et al., 2001; Åman et al., 2003; Disalvo et al., 2008) which

give rise to broad infrared (IR) OH stretching absorption bands (Binder, 2003). Water molecules arrange around the lipids in a primary hydration layer (or shell) with five tightly bound water molecules (Arnold et al., 1983), a secondary hydration layer with six to seven molecules (Binder, 2007) and finally bulk water (Berkowitz et al., 2006).

In the present work, a bottom-up approach was used to study the structure of water in the vicinity of cationic lipid model membranes at a well-defined hydration. Cationic lipids are synthetic lipids and spontaneously form bilayer assemblies in aqueous media in analogy to naturally occurring phospholipids (Kunitake et al., 1977). There is a broad interest in studying this lipid class because of its potential application as gene transfection agents (Felgner et al., 1987; Rädler et al., 1997; Zuhorn et al., 2007; Bhattacharya and Bajaj, 2009). Despite their auspicious therapeutic benefit, the focus of this work is set on the extraordinary properties of the interfacial water of four particular cationic lipids, the dioctadecyldimethylammonium halides (DODAX, X = F, Cl, Br, I). They stand out due to their low water capacity which allows the direct examination of interactions between the lipid and water from the first hydration shell (see section 4.2). Hydrophilic water-anionic interactions within DODAX model membranes were studied by means of attenuated total reflection (ATR) Fourier-transform (FT) infrared (IR) spectroscopy and are presented in section 4.3. The technique has been proven to be a powerful tool to investigate molecular orientation and ordering of membranes and associated water and allows the detection of subtle changes in the lipid-bound water structure (Harrick, 1987; Goormaghtigh et al., 1999; Binder, 2007). The OH stretching band frequencies of DODAX bound water are assigned by comparison with spectra of aqueous salt solutions and small halide water clusters as well as results from MD simulations of water within DODAB (see section 4.4).

Part 2: Neuronal mechanosensitivity and network formation

The second part of this thesis is dedicated to the modulation of neuronal growth on different lipid bilayer systems in order to gain a deeper understanding of their peculiar mechanosensitive behavior. Two types of neurons – NG108 cells and primary mouse retinal ganglion cells (RGCs) – cultured on sBLs and polymer-tethered lipid bilayers (tBLs) were investigated using phase contrast microscopy. Neuronal growth of NG108 cells was quantified in terms of neurite length and branching (see section 5.1.1). Additionally, the extension of *single* neurites from RGCs was examined for two different time regimes as presented in section 5.1.2. First, long-term growth speeds of single neurites on both substrates were compared during two days of culture regarding the global neurite growth. Similarly, forward and retraction speeds within the first two hours were investigated

because growth events occurring on shorter time scales may be masked after two days *in vitro*. Finally, the results of NG108 and RGC growth are discussed in the light of an inverse neuronal durotaxis in section 5.3.4.

Lipid bilayer substrates had only little influence on the growth behavior of the neurons as discussed in sections 5.1.3 and 5.3.1. However, primary RGCs exhibited a dynamic growth behavior which was reflected by the formation of neuronal networks after several hours in culture (see section 5.2.1). To gain further insights in the temporal evolution of structural neuronal networks, in the last part of the present work a time-resolved analysis of RGC networks was carried out (see section 5.2.1). Topological graphs were abstracted from phase contrast images recorded by time-lapse video microscopy. The graph theoretical analysis of the connectivity, shortest path length and the edge length unveiled different network stages as presented in section 5.2.2. Moreover, it will be shown how RGC networks self-organize to optimized networks with robust small-world properties (sections 5.2.3 and 5.3.6).

2. Background

2.1. Interactions of lipid membranes and water

2.1.1. General remarks

In the introduction it has already been expounded that plasma membranes are built up of a 2D fluid containing a complex mixture of lipids and proteins and highlighted its role as a platform for a variety of cellular processes (Alberts, 2002). Water as ubiquitous solvent has a fundamental influence on biomolecules: the self-assembly of lipid membranes is entropically driven by the hydrophobic effect (Tanford, 1978) and structured water is associated with all proteins, DNA and cell membranes (Bhattacharyya, 2008). Furthermore, the hydration of lipid membranes crucially alters their structural and dynamical properties and consequently the membrane's functioning in cells. Thus, an all-embracing understanding of lipid-water interactions is important (Bonn and Campen, 2009; Berkowitz and Vácha, 2012).

In an aqueous environment lipids self-assemble to micelles, lamellar, cubic or hexagonal phases, which depends on intra- and intermolecular interactions as well as geometric packing constraints (Luzzati et al., 1968; Israelachvili et al., 1976; Seddon and Templer, 1995). However, in the following only lamellar aggregates will be considered for two reasons – firstly, biological membranes are in the fluid lamellar L_α phase (Bloom and Mouritsen, 1995) and, secondly, the double-chained lipids used in the experiments presented in this thesis assume the structure of planar bilayers. Phase transitions can be induced by changing the water concentration (lyotropic) or temperature (thermotropic). Furthermore, there are internal phase transitions which keep the aggregates' superordinate morphology unaffected and lead to conformational changes of the lipids as presented in section 4.1. A detailed characterization of the so-called lipid polymorphism and the physical properties of lipid membranes has been subject of plenty studies – an overview is given in (Marsh, 1990; Cevc, 1993; Mouritsen, 2005).

The effect of aqueous medium on the structural organization of lipid membranes has attracted constant attention for more than forty years and was studied by thermodynamic (differential scanning calorimetry) (Chapman and Urbina, 1974), scattering (x-ray and

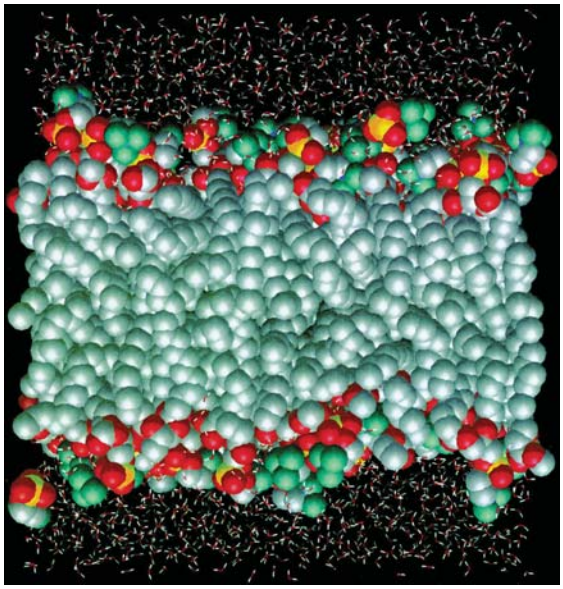

Figure 2.1.: Snapshot of an MD simulation of a DPPC bilayer containing 128 lipid and 3910 water molecules (drawn as sticks). Color coding: hydrogens are white, oxygens red, phosphorous yellow, carbons gray, the three methyl groups on the choline blue and nitrogens dark blue. Image from (Tieleman et al., 1997).

neutron diffraction) (Luzzati and Husson, 1962; Johnson et al., 1991; Nagle and Tristram-Nagle, 2000) as well as spectroscopic (nuclear magnetic resonance, NMR, and IR) methods (Bechinger and Seelig, 1991; Gawrisch et al., 1992; Casal and Mantsch, 1984; Zhang et al., 1997; Binder, 2007) (for review see (Milhaud, 2004)). In complement to these experimental techniques, molecular dynamics (MD) and Monte Carlo simulations have been used to investigate hydration forces (Marrink et al., 1993), the distribution and dynamics of water molecules in the vicinity of lipid bilayers (Åman et al., 2003), hydrogen bonding (PasenkiewiczGierula et al., 1997; Lopez et al., 2004) or isotopic effects (Rog et al., 2009) (reviewed in (Tieleman et al., 1997; Berkowitz et al., 2006)). Figure 2.1 displays a snapshot of a 1,2-dipalmitoyl-*sn*-glycero-3-phosphocholine (DPPC) lipid bilayer with adjacent water molecules (taken from (Tieleman et al., 1997)). Since both simulations and experimental techniques advance side-by-side, expedited gain of new insights can be expected in future (Berkowitz and Vácha, 2012).

2.1.2. Hydrogen bonding and the IR spectrum of liquid water

Compared to other simple liquids, water has well-known special properties. It exhibits a density maximum in the liquid state, a high heat capacity and a high boiling point. These properties arise from the presence of a dynamic intermolecular hydrogen (H) bonding network (Ball, 2008b; Bakker and Skinner, 2010). According to the International Union of Pure and Applied Chemistry (IUPAC), the hydrogen bond (HB) is "an attractive interac-

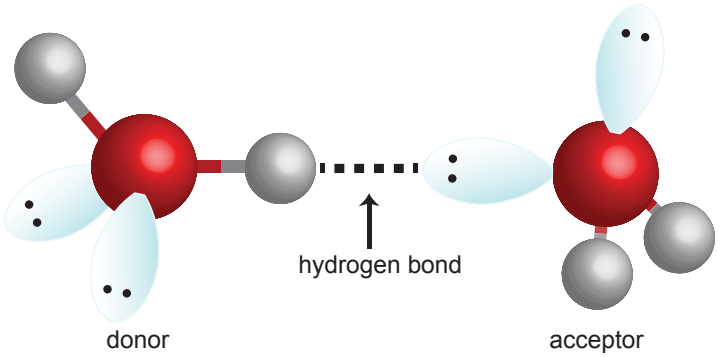

Figure 2.2.: Hydrogen bonding between two water molecules. Color coding: hydrogens are gray, oxygens red and the lone pairs light blue.

tion between a hydrogen atom from a molecule or a molecular fragment X–H in which X is more electronegative than H, and an atom or a group of atoms in the same or a different molecule, in which there is evidence of bond formation“ (Arunan et al., 2011a). Additionally, the authors specified criteria and attributes of HBs. Their nature is primarily electrostatic, but also has a partial covalent character and is influenced by dispersion forces. Moreover, HBs exhibit directionality and cooperativity (Arunan et al., 2011b). Water molecules in the liquid state are frequently reported to form between three and four HBs to neighboring water molecules on average (Ball, 2008a; Paesani et al., 2009). X-ray absorption spectroscopy data suggest the presence of only two HBs per water in the bulk (Wernet et al., 2004), however this work is highly controversial (Ball, 2008a). Figure 2.2 illustrates the HB formation between two water molecules. The oxygen atom with the covalently bound hydrogen acts as HB donor and the other one as HB acceptor.

IR spectroscopy has become a standard technique to study the interactions of water and lipids/proteins as well as the lipid phase behavior (Bonn and Campen, 2009; Binder, 2003; Tamm and Tatulian, 1997). Liquid water gives rise to a complex spectrum with a broad and strong spectroscopic absorption band reflecting a large variation of H bonding within measured water populations (Bertie et al., 1989; Brubach et al., 2005). This vibrational band can be decomposed into several overlapping Gaussian bands of different frequency and width (Paesani and Voth, 2009; Brubach et al., 2005; Liu et al., 2004) ascribed to different H bonded environments and/or vibrational modes derived from antisymmetric or symmetric stretching and to a bending overtone absorption (Paesani and Voth, 2009; Binder, 2007) (see table 2.1 and figure 2.3).

Assignment of the bands is challenging because relevant vibrational stretching modes involve complex intra- and intermolecular couplings (Bakker and Skinner, 2010; Brubach et al., 2005; Walrafen, 1967; Binder, 2003; Smith et al., 2005; Auer and Skinner, 2009; Eftekhari-Bafrooei and Borguet, 2010). Despite the large body of experimental data accumulated over the last decades and recent progress on the theoretical description, there

Vibrational mode	H_2O	D_2O
L, librations	500 - 800 cm^{-1}	
ν_2, bending	1643.5 cm^{-1}	1209.4 cm^{-1}
$\nu_2 + L$	2127.5 cm^{-1}	1555 cm^{-1}
$2\nu_2$, overtone of bending[a,b]	~3250 cm^{-1}	~2400 cm^{-1}
ν_1, symmetric stretching	~3450 cm^{-1}	~2500 cm^{-1}
ν_3, antisymmetric stretching[b]	~3600 cm^{-1}	~2600 cm^{-1}

Table 2.1.: Band positions and assignment of vibrational modes of liquid water (Venyaminov and Prendergast, 1997). [a]Enhanced by a Fermi resonance, [b]shoulder.

is still no consensus in the assignment of stretching bands of bulk liquid water (Paesani and Voth, 2009). H bonding environments in liquid water alternated by effects of temperature or solutes are easier to interpret in terms of localized interactions, if the OH/OD stretching band from uncoupled OH/OD oscillators occurring in dilute HOD in H_2O or D_2O is analyzed (Bergström and Lindgren, 1992; Auer and Skinner, 2008). Ultrafast vibrational spectroscopy methods for investigation of dilute HOD led to a significant increase of knowledge on the dynamical behavior of liquid water (Bakker and Skinner, 2010; Skinner, 2010).

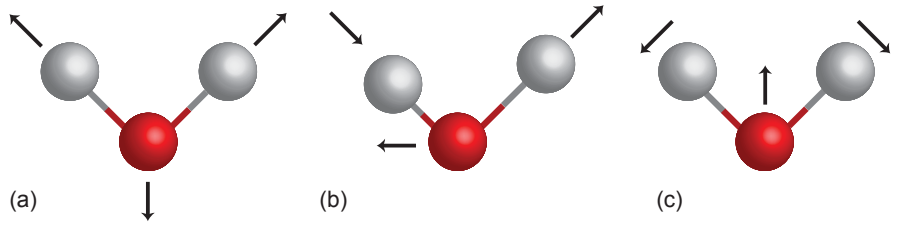

Figure 2.3.: Fundamental vibrations of an isolated water molecule: Symmetric (a) and antisymmetric (b) stretching, bending (c).

Lipid-water interactions have been often assessed by examining phospholipid headgroup IR absorptions such as carbonyl or phosphate bands (Binder, 2003; Hübner and Blume, 1998; Lewis and McElhaney, 2007; Casal and Mantsch, 1984; Binder and Pohle, 2000). Alternatively, the distinct bonding structures of lipid-bound water can be monitored by changes of water stretching IR absorptions. Water near lipid molecules is structured in layers from tightly bound water in close proximity to the lipids' carbonyl groups, over more weakly bound water in the first hydration shell at the lipids' phosphocholine groups up to water with bulk-like properties (Berkowitz et al., 2006). Although this was reported from MD simulations, differently H bonded water also leaves a detectable signature in the OH stretching spectrum as reported by (Binder, 2007). Strongly H bonded water molecules exhibit an OH stretching vibration that is shifted to lower frequencies in comparison to weakly H bonded water (Steiner, 2002). However, these changes are

relatively small leaving the stretch bands similar to those observed for pure liquid water. This resemblance indicates a related flexible H bonding network as proposed for the bulk liquid (Binder, 2007). Differences in the dynamics between water bound to the membrane and bulk water were demonstrated experimentally by recent ultrafast vibrational spectroscopy methods which particularly probe interfacial molecules (Volkov et al., 2007; Tielrooij et al., 2009; Bonn et al., 2010).

2.1.3. Confined water near lipid membranes

As mentioned above, water bound to biological membranes possesses special properties in comparison to the bulk liquid which shall be introduced briefly. Reduced rotational motion of confined water within low hydrated phospholipid and cationic lipid membranes was revealed by ultrafast vibrational and IR spectroscopy (Volkov et al., 2007; Zhao et al., 2008; Tielrooij et al., 2009; Bonn et al., 2010). Two different water species were detected: the first ("irrotational water") exhibited stronger H bonding, a decreased energy transfer rate and fast orientational relaxation accompanied by an OH stretching frequency shift to lower frequencies (Bonn et al., 2010; Volkov et al., 2007; Tielrooij et al., 2009). A second small fraction of water molecules with fast reorientation and a reduced number of HBs (1 - 2 instead of 4) was attributed to weak H bonding (Tielrooij et al., 2009). However, Zhao *et al.* ascribed the irrotational water to water molecules surrounding the phosphate group of the phosphocholine headgroup (Zhao et al., 2008), which is in contrast to the finding by Rezus and coworkers who reported a similar reduced reorientation due to hydrophobic methyl groups (Rezus and Bakker, 2007). This shows that most of the experimental techniques cannot determine unambiguously to which lipid groups the water molecules are bound, i.e., whether they are located at the phosphate or at the choline group region (Tielrooij et al., 2009).

The just given example underlines how valuable insights from complementary MD simulations can be to clarify the water structure near lipid membranes. Firstly, they unveiled also a slow down of translational motion of water bound to phospholipid bilayers, e.g., from $10^{-5}\,\mathrm{cm}^2/\mathrm{s}$ for the bulk liquid to $\sim 2 \cdot 10^{-7}\,\mathrm{cm}^2/\mathrm{s}$ for DMPC (1,2-dimyristoyl-*sn*-glycero-3-phosphocholine) (Lopez et al., 2004). The simulated density and electron density of water bound to phospholipids showed various regimes assigned to different locations of water, i.e., at the backbone and carbonyl groups, in the first external shell near the phosphocholine group, in secondary hydration shells and in bulk water (Berkowitz et al., 2006; Bhide and Berkowitz, 2005). In the latter study the number of HBs was found to decrease from ~ 3.7 to ~ 3.0 which is compensated by energetically stronger bonds and was confirmed by IR spectroscopic measurements (Berkowitz and Vácha, 2012; Binder,

2007). Furthermore, the strength of HBs decreases from water–phosphate O to water–carbonyl O and is lowest between two water molecules (Berkowitz and Vácha, 2012; Bhide and Berkowitz, 2005).

These properties cover only few aspects of lipid/water interactions and are not meant to give a full description. Further details about interfacial water confined at lipid membranes are given in several reviews (Milhaud, 2004; Berkowitz et al., 2006; Binder, 2007; Disalvo et al., 2008).

2.1.4. Molecular orientations of cationic lipid membranes studied by ATR FTIR Spectroscopy

Attenuated total reflection (ATR) Fourier-transform (FT) infrared (IR) spectroscopy is a powerful technique with many advantages – it does not need any marker molecules, it is fast, provides a strong signal and requires only few amounts of sample. Its most outstanding feature is that it allows the determination of molecular ordering and orientation (Harrick, 1987; Goormaghtigh et al., 1999). The method has been first applied to study ordering in biological lipid membranes (Fringeli et al., 1972) and later to examine the interactions of lipids and water (Binder, 2003, 2007).

Many amphiphilic lipid molecules spontaneously assemble to oriented molecular structures on a solid support. This property allows to prepare oriented multibilayer stacks by simply spreading an organic stock solution on the ATR crystal. After solvent evaporation, cast films with an average thickness of a few micrometer remain on the surface of the ATR crystal (Binder, 2003). Polarized ATR FTIR spectroscopic measurements are classified by the sample thickness, d, with respect to the penetration depth, λ_d, of the evanescent wave of the IR light. Thick films are formed by samples for which the relation $d > \lambda_d$ holds. Their properties together with their advantage over thin films were extensively discussed regarding the calculation of the mean-square electric field components (Picard et al., 1999). Phase behavior and molecular ordering of the film's first few bilayers may be influenced by the solid support. This can be circumvented by using thick films where really bulk properties are probed (Binder, 2003).

Vibrational spectroscopy is based on the absorption of electromagnetic IR radiation by matter due to the interaction of the electric field with oscillating permanent dipoles of the atomic groups. The transition dipole moment, $\vec{\mu}$, is a vector and the square of its projection on the electric field vector is directly proportional to the absorption (see figure 2.4). Hence, the IR absorption of an oriented film depends on the polarization of the incident electromagnetic radiation. This property is called linear dichroism and can be determined by means of ATR FTIR spectroscopy (Binder and Schmiedel, 1999). The

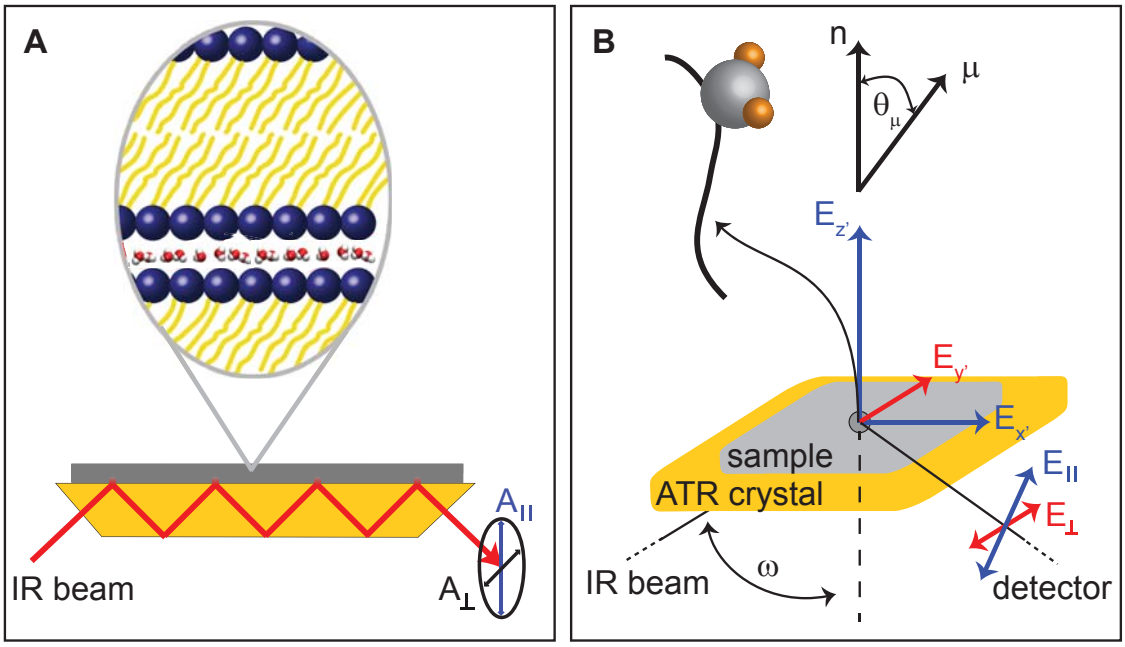

Figure 2.4.: *A*: Total reflection in the ATR crystal (orange) covered with a thick lipid film consisting of multilayers (gray). The absorbance is measured with parallel and perpendicular polarized light. *Section*: interfacial water molecules in close proximity to the lipid headgroups. *B*: Geometry of the ATR experiment. The lipid sample is irradiated with a polarized IR beam. The absorbances $A_{\parallel}$ and $A_{\perp}$ are determined by the projections of electric field amplitudes $E_{x'}$, $E_{y'}$ and $E_{z'}$. The orientation angle θ_{μ} is enclosed by the normal of the ATR crystal $\vec{n}$ and the transition dipole moment $\vec{\mu}$ of the IR active group. Image adapted from (Binder, 2003).

polarized incident IR beam is totally reflected in the ATR crystal coated with a lipid film. A part of the polarized beam impinges the sample, the so-called evanescent wave which is attenuated and finally absorbed at a penetration depth of approximately one micron (cf. figure 2.4) (Harrick, 1987; Mirabella and Harrick, 1985).

Molecular ordering and orientation are determined from the IR order parameter S_{IR}. It can be obtained from the absorbances $A_{\parallel}$ and $A_{\perp}$ measured using parallel and perpendicular polarized light. The derivation of S_{IR} was described by Harrick and later by Binder and is briefly outlined in appendix A (Harrick, 1987; Binder, 2003). It depends on the dichroic ratio, R, as follows (Harrick, 1987; Fringeli and Günthard, 1981):

$$S_{\mathrm{IR}} = \frac{R - K_1}{R + K_2} \qquad \text{and} \qquad R \equiv \frac{A_{\parallel}}{A_{\perp}} \tag{2.1}$$

with the optical constants $K_1 = 2$ and $K_2 = 2.54$ for the case of a ZnSe ATR crystal and thick lipid films (Binder and Schmiedel, 1999).

The mean orientation of an individual transition dipole moment $\vec{\mu}$ is determined from the definition of the IR order parameter as (Saupe, 1964):

$$S_{\mathrm{IR}} = \frac{1}{2}\left\langle 3\cos^2\theta_{\mu} - 1 \right\rangle \tag{2.2}$$

θ_μ is the angle enclosed by the transition dipole moment $\vec{\mu}$ of the oscillating group and the normal of the ATR crystal $\vec{n}$ (see figure 2.4). Furthermore, the tilt order parameter S_θ of polymethylene chains is given as a linear combination of the IR order parameters of the symmetric and antisymmetric CH_2 stretching mode (Binder and Schmiedel, 1999):

$$S_\theta = -\left[S_{\mathrm{IR}}\left(\nu_{\mathrm{s}}(\mathrm{CH_2})\right) + S_{\mathrm{IR}}\left(\nu_{\mathrm{as}}(\mathrm{CH_2})\right)\right] \tag{2.3}$$

Equations 2.1 to 2.3 allow a detailed characterization of the molecular ordering and orientations of both the lipid membranes and adjacent water molecules.

The model membranes investigated in the framework of this thesis were composed of dioctadecyldimethylammonium halides (DODAX, X = F, Cl, Br, I). These are structurally simple two-chain lipids spontaneously forming bilayer assemblies in aqueous media – a behavior related to that of naturally occurring phospholipids (Kunitake et al., 1977). Thermotropic and lyotropic phase behavior of DODAB and DODAC model membranes of different morphology have been addressed previously by various methods (Umemura et al., 1984; Kawai et al., 1986; Laughlin et al., 1990; Schulz et al., 1998; Feitosa et al., 2000; Saveyn et al., 2009; Wu et al., 2009). Water molecules adhered to DODAX model membranes can only form HBs to other water molecules or to the halide counterions. The water capacity of DODAX (X = Cl, Br) phases under controlled laboratory conditions was found to range between one and three water molecules per lipid (Kawai et al., 1986; Laughlin et al., 1990). This is very low in comparison to phospholipids, where values between 6 and 30 were reported (see chapter 1). Thus, the presence of bulk water can be ruled out as only interfacial water can be accommodated in the DODAX multilayers – which provides a peculiar model system for a spectroscopic study of confined water within lipid membranes.

2.2. Neuronal mechanosensitivity

2.2.1. Mechanosensation – feeling for the substrate

Although most of the living organisms are single cells, obviously these smallest units are able to proliferate and communicate with each other to form complex multicellular aggregates such as tissues, mammals or human bodies, which consist of approximately 10^{13} cells (Alberts, 2002). The organization of cells in higher structures requires for example adhesion to other cells or the extracellular matrix (ECM) and involves growth and pathfinding. These processes are directed by external signals denoted as guidance cues in the case of neuronal growth (Franze and Guck, 2010). They can be divided into two

classes: *chemical signals* comprise gradients of diffusing molecules and molecules bound to cellular or extracellular surfaces. *Physical stimuli* include external forces, substrate topography, electrical, optical and mechanical cues (Franze and Guck, 2010; Ladoux and Nicolas, 2012). Their conversion into biochemical signals is followed by an activation and amplification of intracellular signal cascades which entail a cellular response (Ladoux and Nicolas, 2012).

Evidence for the cell's susceptibility to mechanical stimuli like a modified substrate stiffness was observed for a broad range of cellular processes, e.g., the cell cycle (Janmey et al., 2009), spreading (Guo et al., 2006), cell motility and traction forces (Pelham and Wang, 1997; Lo et al., 2000; Koch et al., 2012), shape (Pelham and Wang, 1997; Ghibaudo et al., 2008; Tee et al., 2011), differentiation (Engler et al., 2006), the assembly of focal adhesions (Pelham and Wang, 1997) and the cell's ability to match its internal stiffness with that of the external substrate (Solon et al., 2007). Tissue cells like fibroblasts and epithelial cells showed a higher spreading area and increased traction forces on hard substrates and weaker adhesions on soft substrates, respectively (Lo et al., 2000; Guo et al., 2006). Furthermore, they turned away from soft areas in order to migrate towards regions of higher substrate stiffness (Lo et al., 2000). The designation for this phenomenon was coined by Lo and coworkers – the so-called "durotaxis".

Neurons, which are interesting in the light of the present thesis, also showed a mechanosensitive response regarding altered substrate rigidity. Beside morphological parameters like the number of neurites (Gunn et al., 2005) and branching points (Flanagan et al., 2002), neurite length (Norman and Aranda-Espinoza, 2010) and axonal extension rates (Balgude, 2001; Kostic et al., 2007; Norman and Aranda-Espinoza, 2010), also traction forces (Koch et al., 2012) and the survival rate (Georges et al., 2006) were found to change with substrate stiffness. However, in contrast to other cells, preferred neuronal growth was found on soft substrates with a Young's modulus of 230 Pa (Flanagan et al., 2002) or those of intermediate stiffness (870 -1000 Pa) (Norman and Aranda-Espinoza, 2010; Koch et al., 2012). Even more strikingly, Georges *et al.* reported that in co-cultures of neurons and astrocytes on hard substrates, the neurons preferentially grew on top of the soft astrocytes (Georges et al., 2006) – a behavior which strongly resembles the situation *in vivo*. In the brain, neurons grow and migrate along glial cells which were measured to be by a factor of two softer than for example primary neurons of hippocampus and retina (Lu et al., 2006; Franze and Guck, 2010).

Although so far these findings appear very convincing, it has to be noted that the large body of studies on neuronal mechanosensitivity has not converged to a clear picture yet. This was attributed to varied cell culture conditions and the choice of analyzed growth parameters which frequently purveyed ambiguous results (Franze and Guck,

2010). Three years after the review of Franze and Guck, it has to be added that also the neuron type influences the results as discussed more thoroughly in chapter 5.

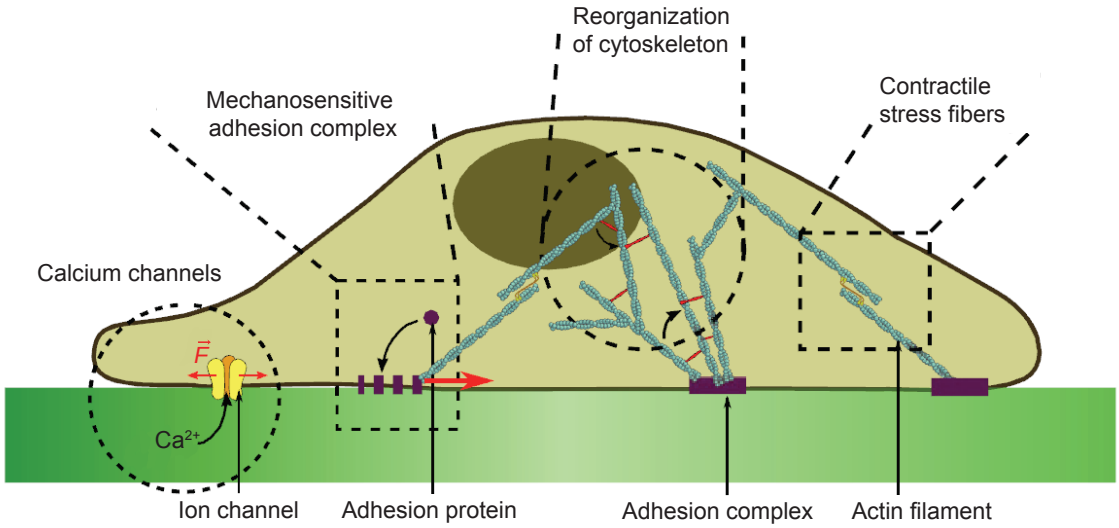

Figure 2.5.: Schematic of mechanosensing units in a tissue cell. Image adapted from (Ladoux and Nicolas, 2012).

Apart from the missing unified parameter space which can be probed to measure the mechanosensitive response of neurons, the mechanisms involved in sensing of substrate rigidity are not yet fully understood – neither for tissue cells (Ladoux and Nicolas, 2012) nor for the origin of the peculiar mechanosensitive behavior of neurons (Moore and Sheetz, 2011; Franze and Guck, 2010). Figure 2.5 illustrates different units of a tissue cell that are involved in mechanosensing (Ladoux and Nicolas, 2012) and also partly apply to neurons. When a cell is exposed to external stresses, it can respond via mechanisms involving the assembly or disassembly of adhesion complexes (Pelham and Wang, 1997; Geiger et al., 2009), a remodeling of the contractile acto-myosin apparatus (Mitrossilis et al., 2009; Zemel et al., 2010) and the activation of calcium ion channels (Lo et al., 2000; Vogel and Sheetz, 2006; Kobayashi and Sokabe, 2010). Another proposed mechanism is that surface adhesion molecules like cadherins and integrins are mechanically coupled to the nucleus via the cytoskeleton and, therefore, modulate gene expression after stimulation (Wang et al., 2009).

The cellular structures that are able to receive such signals from the exterior are focal adhesions (FAs). They are involved in the mechanotransduction and the motility of various cell types such as tissue cells (Bershadsky et al., 2003). As shown in figure 2.6, they are protein complexes consisting of transmembrane receptors from the integrin family which mediate cell-substrate adhesions by linking actin filaments (stress fibers) to the ECM. FAs are large, i.e., up to several micrometers long and structurally polarized (Bershadsky et al., 2006). Their function not only includes the exertion of traction from the

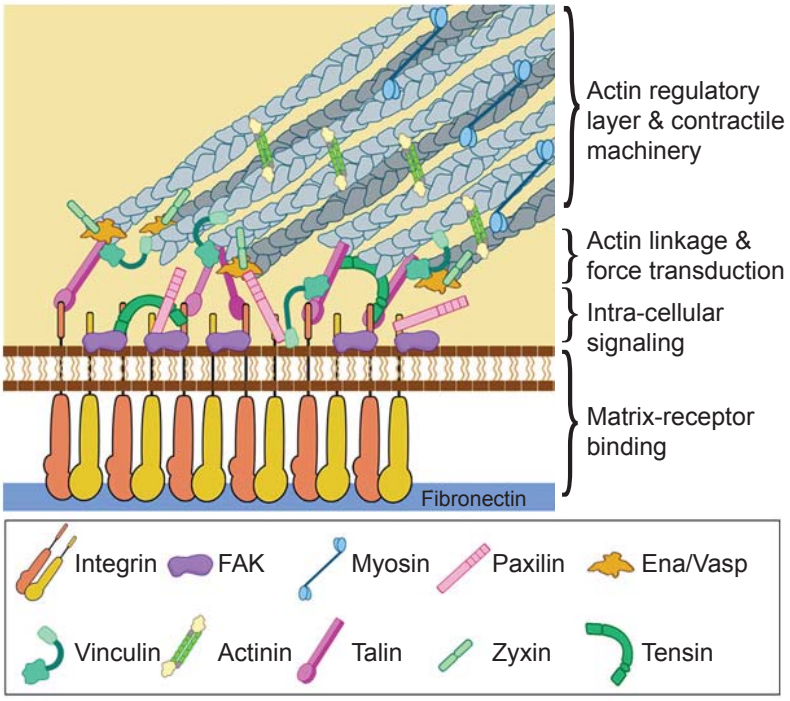

Figure 2.6.: Illustration of a mature FA which contains hundreds of proteins that are grouped based on their contribution to four basic processes: receptor/matrix binding, linkage to actin cytoskeleton, intracellular signal transduction and actin polymerization. Both actin polymerization and actomyosin contractile machinery generate forces that affect mechanosensitive proteins in the actin linking module, the receptor module (e.g., integrins), the signaling module and the actin polymerization module. The combined activity of the mechanosensitive components form the mechanoresponsive network. Used by permission from MBInfo: www.mechanobio.info; Mechanobiology Institute, National University of Singapore.

ECM to the cytoskeleton, but they also constitute a platform for integrin-based signaling (Geiger et al., 2009).

For neurons a different scenario was unveiled – instead of strong FAs, nerve cells exhibit so-called *point contacts* (McKerracher et al., 1996) (see also figure 2.7). The neuronal architecture comprises a cell body with cytoplasm, organelles and the nucleus, but in contrast to other cells also a long axon and fine, branched dendrites both also referred to as processes or neurites *in vitro* (Bear et al., 2007). The leading tip of these processes – the neuronal growth cone – plays a pivotal role in the process formation. It provides the machinery to move forward and exert traction as well as guiding elements for a directed movement using integrin-dependent adhesion sites (Lowery and van Vactor, 2009; Santiago-Medina et al., 2012). These point contacts are uniformly distributed over the cell and they are smaller and have shorter lifetimes than FAs (Tawil et al., 1993; Santiago-Medina et al., 2012).

In the context of growth cone motility, the complexes of coupling proteins between the substrate and the cell's cytoskeleton are referred to as *molecular clutch* (Mitchison and Kirschner, 1988; Suter and Forscher, 2000). If the clutch is engaged, the retrograde flow

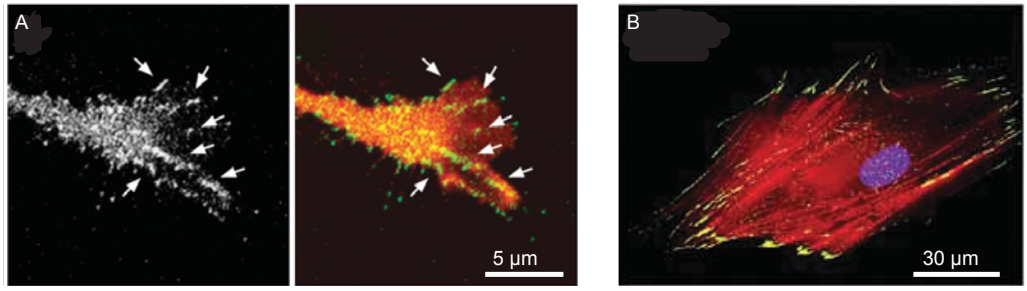

Figure 2.7.: Adhesion sites in nerve and tissue cells. While neurons exhibit small uniformly distributed point contacts (left), tissue cells couple to the substrate via strong FAs located at the end of stress fibers (right). *A*: Growth cone of *Xenopus laevis* on laminin fluorescently labeled with GFP-dSH2 to show phosphotyrosine within the point contacts (left) and overlay of a live stain with tetramethylrhodamine-conjugated dextran (red) and phosphotyrosine (green). (Images adapted from (Robles and Gomez, 2006)). *B*: Human foreskin fibroblast (HFF) on a substrate coated with fibronectin. The HFF cells express paxillin-YFP (green) which is associated with FAs and were additionally stained with TRITC-phalloidin (red) for actin stress fibers and DAPI (blue) for the nucleus. Image adapted from (Prager-Khoutorsky et al., 2011).

is blocked by mechanical coupling to the ECM and the growth cone moves forward due to actin polymerization (Suter and Forscher, 2000). It has to be emphasized that this link is important for the transmission of forces as the latter play an essential role in growth cones (Franze and Guck, 2010; Suter and Miller, 2011). Already in the late 1970s and early 1980s it was shown that neurites are under tension and that externally applied forces are sufficient to cause neurite extension (Bray, 1979, 1984). Furthermore, neurons are able to generate traction forces in dependence on the substrate stiffness, i.e., highest forces on soft substrates of approximately 1 kPa (Chan and Odde, 2008; Koch et al., 2012). Due to the crucial interplay of forces, adhesion sites and growth events it was proposed that traction forces at point contacts or FAs can also act as mechanosensors (Moore et al., 2010; Schwarz and Gardel, 2012).

Moore and Sheetz pictured three mechanisms for neuronal rigidity sensing based on traction forces – "protein stretching", "catch bond formation" and "clutch slippage" as illustrated in figure 2.8 (Moore and Sheetz, 2011). The first involves the *stretching of proteins* under mechanical tension which undergo conformational changes that can alter the protein's activity (Moore and Sheetz, 2011). An example is the higher opening probability of mechanosensitive ion channels in dependence on mechanical tension (Yoshimura and Sokabe, 2010). Due to this model on stiffer substrates larger protein stretching occurs and causes a strengthening of the ECM/receptor link, i.e., larger forces on stiffer substrates (Moore and Sheetz, 2011). The *catch bond* is characterized by a counterintuitive prolongation of the bond's lifetime under force (Kong et al., 2009). It was observed within certain ranges of forces and was reported for linkages between integrin and fibronectin (Kong et al., 2009) as well as myosin II and actin filaments (Guo and Guilford, 2006). Thus, the model applies to systems were highest traction forces were found at intermediate rigidity

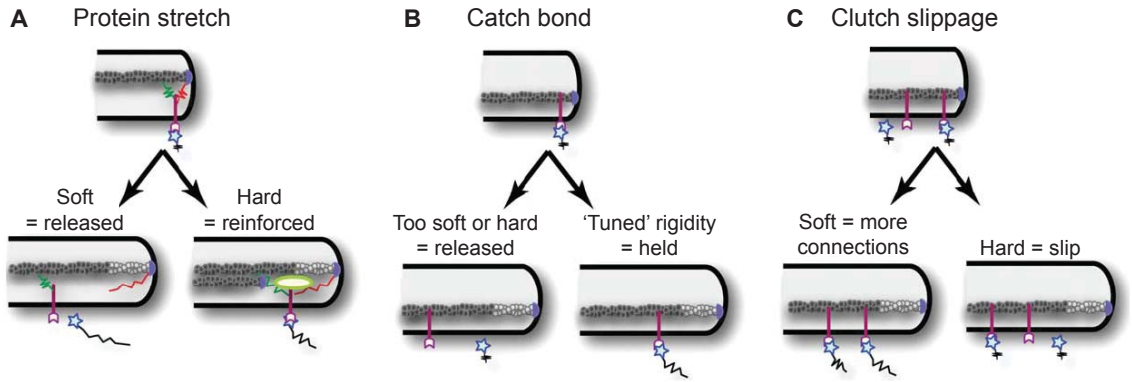

Figure 2.8.: Three possible ways of mechanosensing at the linkage of ECM/adhesion sites. *A:* On hard substrates proteins in the adhesion sites undergo conformational changes such as the opening of ion channels leading to a reinforcement of the ECM-cytoskeleton connection and, thus, to higher traction forces on stiffer substrates. *B:* A catch bond between ECM and adhesion molecule is related to a force-induced prolonged lifetime of the bond. It is strengthened within a specific interval of rigidities. *C:* In the clutch slippage model the retrograde actin flow is coupled to the ECM at the adhesion sites, i.e., on harder substrates faster loading rates decrease the number of receptor/ECM linkages. Image adapted from (Moore and Sheetz, 2011).

regimes (Moore and Sheetz, 2011). The last proposed mechanism explains the high traction forces of neurons on soft substrates (below 1 kPa) (Chan and Odde, 2008). The *clutch slippage* (or frictional slippage) is related to the molecular clutch mentioned above. The coupling of ECM and adhesion molecule leads to a high retrograde actin flow and low traction forces on harder substrates and an inverse behavior on soft substrates. Thus, on hard substrates a decreasing lifetime of the actin/clutch linkage results in fewer effective coupling sites, i.e., weaker traction (Chan and Odde, 2008).

A detailed knowledge about neuronal growth including the underlying mechanisms as well as the possibilities of stimulation and controlled guidance is important at least for two reasons. Certainly one is to understand how the nervous system develops (Lowery and van Vactor, 2009). The second one concerns the treatment of injured nerves and diseases related with cellular dysfunction in consequence of modified stiffness (Franze and Guck, 2010; Janmey and Miller, 2011). A damaging of brain tissue is followed by the formation of a glial scar due to reactive astrocytes which was shown to inhibit the regrowth of axons (Silver and Miller, 2004). Franze and Guck suggest that the altered mechanical properties of the scar contributes to the hindrance of axonal recovery (Franze and Guck, 2010). Future research will also have to focus open questions such as the dimensionality – 3D vs. 2D substrates (Cukierman et al., 2001) as well as distances at which a cell is still able to sense differences in the substrate rigidity and corresponding time scales (Janmey and Miller, 2011; Ladoux and Nicolas, 2012).

2.2.2. Soft or fluid? – In search of optimal substrates for delicate neurons

The study of each biological system relies on the utilization of adequate model systems because many interactions cannot be accessed in the complex environment *in vivo*. High demands are made on the substrates and matrices for cell culturing in order to mimic physiologic conditions regarding parameters like stiffness (Flanagan et al., 2002) or coating proteins (Sun et al., 2012), but also with respect to a convenient preparation and characterization.

Flanagan and coworkers outlined the early development of using substrates different from glass or plastic used in conventional cell culture dishes (Flanagan et al., 2002). Over 40 years ago Bard and Hay observed striking differences in the morphology of epithelial cells and fibroblasts in 3D collagen gels which resembled the behavior in intact tissue (Bard, 1975; Hay, 1982). In the late 1990s pioneering studies by Pelham and Wang revealed that epithelial cells and fibroblasts not only showed different morphologies but also motility rates on deformable gels in dependence of substrate stiffness (Pelham and Wang, 1997). This work was followed by another seminal study on the guidance capability of gradients in substrate stiffness, namely the migration of fibroblasts towards regions of higher stiffness (Lo et al., 2000).

The utilization of polyacrylamide (PAA) hydrogels enables a controlled elasticity by varying the fraction of bisacrylamide acting as cross-linker. In the first studies, hydrogels were characterized by determining the Young's modulus, E, macroscopically by applying a well-known force to a sheet of defined size and measuring the change in elongation (Pelham and Wang, 1997) as well as microscopically by deforming the thin PAA sheets with microneedles as described in (Lee et al., 1994). Nowadays, elastic properties of hydrogels are commonly probed by means of rheology experiments (Koch et al., 2012), where E is calculated from the measured storage modulus, G', and the Poisson ratio, ν, using the relation $E = 2G'(1+\nu)$. The elasticity of hydrogels can be tuned over several orders of magnitude with a Young's modulus between several pascals up to hundreds of kilopascals (Pelham and Wang, 1997; Jiang et al., 2007). Thus, these substrates can be used to mimic a variety of cells and tissues ranging from soft brain cells (0.1 - 10 kPa), over muscle cells (12 - 100 kPa) and stiff tissue cells (600 - 1000 kPa) (Moore et al., 2010).

So far only hydrogels have been introduced, however, they are not the only representatives of elastic scaffolds to study the mechanosensitive behavior of cells. Further approaches include micropatterns (Balaban et al., 2001; Geiger et al., 2009) and micropillars (Ghibaudo et al., 2008). Different methods for the preparation of micropatterns comprise for example soft and photolithography, jet patterning or procedures based on photoim-

mobilization and photochemistry (Falconnet et al., 2006). Micropillars and -needles are similarly fabricated using soft photolithography (Le Digabel et al., 2010). They can be adjusted regarding radius and length and yield a Young's modulus in a similar regime as hydrogels – from 1 up to 150 kPa (Ghibaudo et al., 2008).

A common feature of all these elastic substrates is that they allow the determination of traction forces (Balaban et al., 2001; Beningo and Wang, 2002; Chan and Odde, 2008; Ghibaudo et al., 2008). However, the striking difference is that hydrogels are in contrast to pillars/patterns continuous substrates with fixed linkers as illustrated in figure 2.9. It shows a schematic of a cell and a phase contrast image of a fibroblast on a deformable PAA gel (figure 2.9, a and b) and a corresponding sketch on micropillars supplemented by a scanning electron micrograph of an epithelial cell (figure 2.9, c and d), respectively. A disadvantage of continuous substrates with fixed cross-links is that cellular FAs which mediate forces are located at discrete adhesion sites (Le Digabel et al., 2010). Therefore, patterned substrates are additionally suitable to probe distances relevant for mechanosensing (Janmey and Miller, 2011).

To summarize this part, *elastic substrates* have been proven to be suitable for studying cellular mechanosensitivity and unveiled invaluable insights in the specific response of many cell types with regard to physical stimulation (Moore and Sheetz, 2011; Ladoux and Nicolas, 2012) (see also section 2.2.1). However, these substrates do not account for *viscous interactions* neither of the cell itself nor of the ECM. Future work will also have to consider this aspect to gain a complete picture of the mechanisms that govern mechanosensation.

An intriguing approach in this field which allows to modify the substrate viscosity is the utilization of tethered lipid membranes (Minner, 2010). It has to be admitted that the idea of plating cells on lipid bilayers is not new, though the scientific goal was different. Since the 1980s and 1990s supported lipid bilayers have been used in immunological studies to shed light on cell adhesion and cell-cell communication (McConnell et al., 1986; Chan et al., 1991; Grakoui et al., 1999; Groves and Dustin, 2003). Furthermore, at the same time hippocampal neurons were cultured directly on self-assembled monolayers (SAMs) with different chemical and physical properties like charge, film thickness and contact angle (Stenger et al., 1993). The authors report that neuronal growth was promoted by positively charged amine/amide groups and found striking differences in size and morphology of cell bodies, neurite extension and branching as well as cell polarity (Stenger et al., 1993).

Applying altered substrate viscosity as novel physical stimulus can be achieved by tethered bilayer (tBL) constructs of varying polymer tether density (Naumann et al., 2002) or multiple bilayer stacks (Minner, 2010). These systems stand out due to mobile cell ad-

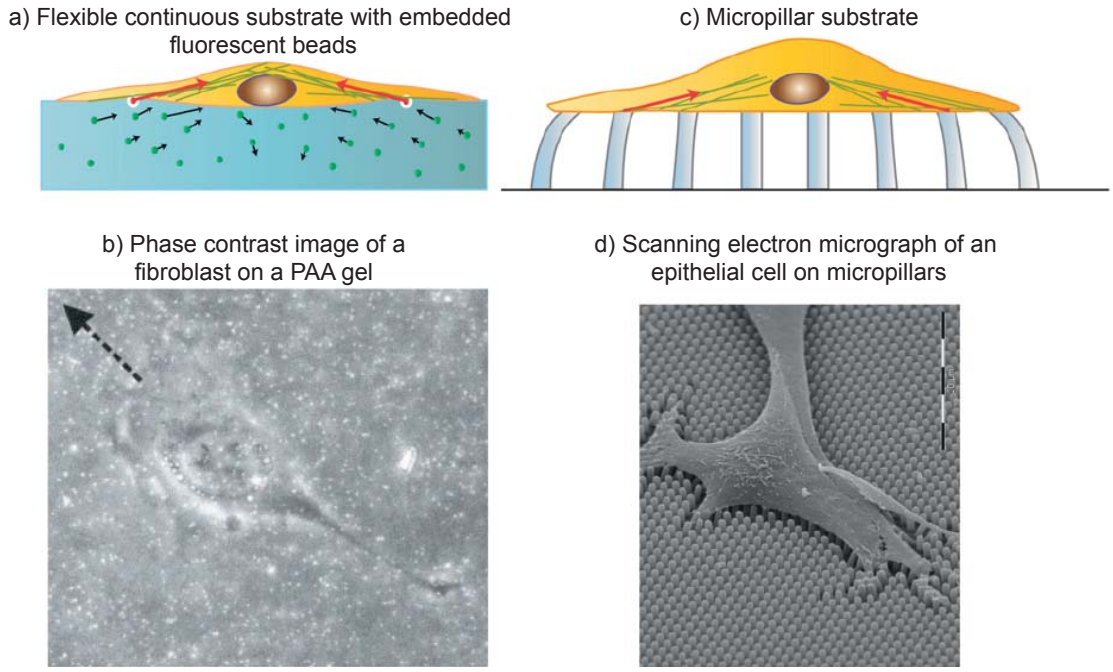

Figure 2.9.: Mechanosensation on elastic substrates: continuous hydrogels (a, b) vs. micropillars (c, d). Cells are able to deform the substrates which allows the calculation of traction forces. Image adapted from (Ladoux and Nicolas, 2012).

hesion molecules in the upper bilayer leaflet which can be translocated to form clusters of integrin receptors by the adhered cells and, therefore, play an important role in contact or focal adhesion formation (LaFlamme et al., 1992). Another feature of lipid bilayer substrates is the possibility of controlled ligand density and spacing that were reported to affect the adhesion, spreading and motility of cells (Maheshwari et al., 2000; Reinhart-King et al., 2005) but also neurite outgrowth (Gunn et al., 2005; Leach et al., 2007). Schematics of a supported lipid bilayer and multibilayer stack, respectively, are given in figure 2.10.

The characterization of these substrates bases on the work by Evans and Sackmann who theoretically derived an expression for the viscous drag coefficient, λ, which characterizes the coupling of a fluid planar bilayer to a rigid substrate (Evans and Sackmann, 1988). One year later this work was extended by the same group (Merkel et al., 1989). The viscous drag coefficient was shown to depend on the viscosity, η_m, and thickness, z_m, of the membrane as follows (Evans and Sackmann, 1988; Merkel et al., 1989):

$$\lambda = 4\pi\eta_m z_m \left(\frac{\epsilon^2}{2} + \frac{\epsilon K_1(\epsilon)}{K_0(\epsilon)} \right), \tag{2.4}$$

where K_0 and K_1 are modified Bessel functions of the second kind and ϵ is a dimensionless parameter given by the relationship (Evans and Sackmann, 1988; Merkel et al., 1989):

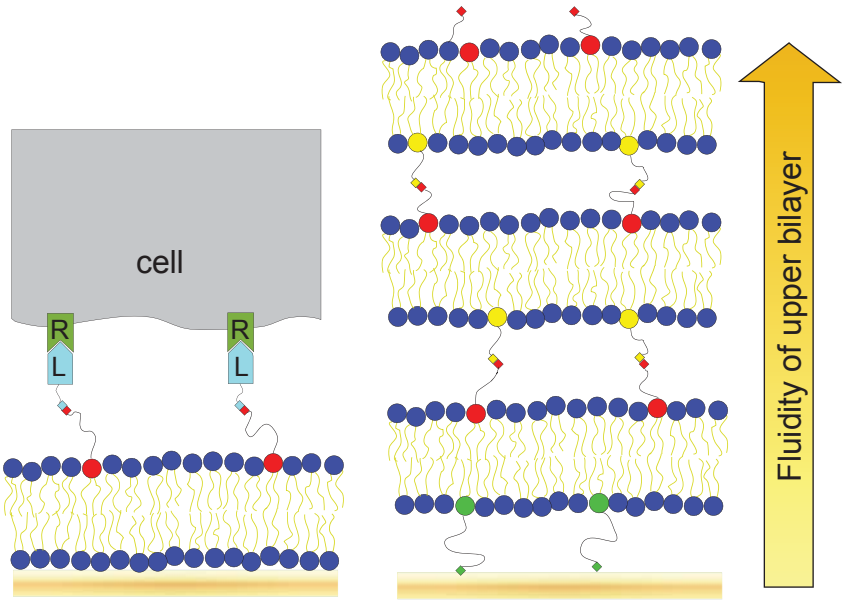

Figure 2.10.: *Left*: Schematic of a supported bilayer coated with ECM proteins (blue) that promote cell adhesion to contact points or FAs via receptor molecules (green). *Right:* Schematic of a polymer-tethered (multiple) bilayer system. The lateral mobility can be varied by changing the lipopolymer (green) concentration in the bottom layer or by using multiple bilayer stacks (Minner, 2010).

$$\epsilon = a\left(\frac{b_s}{\eta_m z_m}\right)^{1/2} \approx a\left(\frac{\alpha\eta_w}{\eta_m z_m d}\right)^{1/2}. \tag{2.5}$$

Here, a disk–like diffusant of radius a is assumed and b_s is the friction coefficient, η_w is the viscosity of water (forming a thin lubricating water film between bilayer and support), α is a constant and d the thickness of the water film (Evans and Sackmann, 1988; Merkel et al., 1989). The diffusion coefficient, D, of a particle laterally diffusing within a 2D fluid, e.g., a lipid bilayer, is given by the Einstein relation $D = k_B T/\lambda$, where k_B is the Boltzmann constant and T the temperature. Since D depends on the viscous drag coefficient, a higher lateral mobility can be achieved by increasing the spacing between bilayer and solid support.

Translating this principle to practical applications, for fluid *supported* lipid bilayers (sBLs) typical diffusion coefficients, D, were found in the order of $5\text{-}7\,\mu m^2/s$ (Tamm and McConnell, 1985; Köchy and Bayerl, 1993). In contrast, single *polymer-tethered* lipid bilayers (tBLs) exhibited a significantly higher mobility (Naumann et al., 2002). The authors showed that by decreasing the lipopolymer concentration to 5 mol% in the lower leaflet, the lipid mobility increased to $D = 17.7\,\mu m^2/s$. This augmentation is based on a decrease of frictional coupling of the bilayer to the substrate due to a larger gap distance between membrane and solid support (Naumann et al., 2002).

In the lab of C. A. Naumann (IUPUI, Indianapolis, IN) the investigation of the diffusiv-

ity in various tBL systems has a long standing tradition. They showed that the diffusion coefficient of a tBL with 5 mol% extends the corresponding value at 30 mol% by one order of magnitude (Naumann et al., 2002) and that there is a strong transbilayer coupling independent of the tether-concentration (Deverall et al., 2008). Furthermore, they reported the occurrence of different buckling patterns in the upper leaflet of the tBL depending on the properties of the polymer-tether molecule (Siegel et al., 2010). Ongoing research addresses the design and characterization of more sophisticated substrates – multiple bilayer systems (see figure 2.10, right). A stepwise increase of the mean-square displacements (MSD, directly proportional to D) was reported for a single (0.138 μm^2), double (0.196 μm^2), triple (0.265 μm^2) and quadruple (0.324 μm^2) bilayer system (Minner, 2010).

These results show that polymer-tethered lipid bilayer substrates constitute a suitable tool to modify the substrate viscosity. Firstly, this can be realized by varying the tether length and concentration of the lipopolymer in the lower bilayer leaflet of single bilayers (the latter approach was used in the present work) (Naumann et al., 2002; Tanaka and Sackmann, 2005). Secondly, modulation of substrate viscosity can be carried out by using multistacks with different number bilayers (Minner, 2010). First results indicate that cells are able to detect differences in the substrate viscosity: while fibroblasts on single bilayers showed the typical strong stress fibers, these vanished on quadruple layer systems and cortical actin structures formed instead accompanied by a stronger polarization of the cells (Minner, 2010). One aim of the present thesis is to elucidate the neuronal response on altered substrate viscosity in order to gain deeper insights in the observed "inverse" mechanosensitive behavior.

Lastly, a few technical aspects are outlined. SBL and tBL substrates are commonly prepared by vesicle spreading (Cremer and Boxer, 1999; Kalb et al., 1992) or Langmuir-Blodgett/Langmuir-Schäfer transfer (Tamm and McConnell, 1985). The advantage of the latter technique is that it enables the deposition of asymmetric bilayer leaflets which is the basis for the fabrication of polymer-tethered lipid bilayers (Wagner and Tamm, 2000; Naumann et al., 2002). Adding a lipopolymer to the first leaflet results in a decrease of the frictional coupling to the substrate and increases the bilayer's fluidity as described above. The second leaflet can be enriched with membrane proteins or receptor molecules that in turn bind proteins. These cell-surface model systems open a large variety of applications, e.g., for the study of immunological reactions and cell adhesion on micropatterned sBLs (Groves and Dustin, 2003). Furthermore, they can be electrophoretically manipulated or placed on semiconductors to measure electrochemical properties of membranes and detect protein function (Tanaka and Sackmann, 2005) or used for the design of novel sensors (Castellana and Cremer, 2006).

The membrane fluidity is characterized by measuring the lateral diffusion within the

bilayer. As for other membrane structures (monolayers, vesicles), single particle tracking (Schütz et al., 1997; Kiessling et al., 2006) and fluorescence correlation spectroscopy (Benda et al., 2003) were successfully used. However, fluorescence recovery after photobleaching (FRAP) is more commonly applied (Purrucker et al., 2004; Naumann et al., 2002; Kalb et al., 1992; Axelrod et al., 1976) and was also chosen to evaluate the substrates used in the present work. Therefore, both the utilization of FRAP and the preparation of sBLs and tBLs are described in more detail in the sections 3.4 and 3.5.

2.3. Complex neuronal networks

2.3.1. Living in a complex world

The previous section highlighted the growth behavior of neurons on suitable substrates. However, it has to be considered that neurite outgrowth is a dynamic process and leads to the formation of neuronal networks. Thus, it is important to shed light on the question how these complex networks form and by which means they can be characterized.

Complex networks are ubiquitous – be it the internet, transportation networks, social networks like scientific coauthorships or those of the family of biological networks such as protein, metabolic or neural networks (Boccaletti et al., 2006). Three examples of a electric power grid, a food web and a functional brain network, respectively, are illustrated in figure 2.11. Stimulated by two pioneering works about small-world networks (Watts and Strogatz, 1998) and scale-free networks (Albert and Barabási, 2002), the interest in these networks has grown tremendously within the last two decades. Advances in the description of complex networks led to a resurgence of graph theoretical approaches which constitute a powerful tool for studying the network's architecture and dynamics (Barthélemy, 2011; Rubinov and Sporns, 2010; Humphries et al., 2008; Boccaletti et al., 2006; Strogatz, 2001).

In neuroscience, this is reflected by numerous topology studies on wiring diagrams, also known as connectomes, reaching from the neural network of the nematode worm *Caenorhabditis elegans* (*C. elegans*) (Watts and Strogatz, 1998; Varshney et al., 2011) over 2D neuronal networks grown *in vitro* (Downes et al., 2012; Bonifazi et al., 2009; Bettencourt et al., 2007; Shefi et al., 2002b), networks of macaque and cat cerebral cortex (Hilgetag and Kaiser, 2004; Sporns et al., 2004, 2000) up to the human brain (Bullmore and Bassett, 2011; Stam, 2010; He et al., 2006). The nature of these networks is small – not in the sense of length scales, but in terms of the network class. Small-world networks stand out due to *high clustering coefficients* similar to regular lattices and at the same time they exhibit *short characteristic path lengths* like random graphs (Watts and Strogatz, 1998) (see also fig-

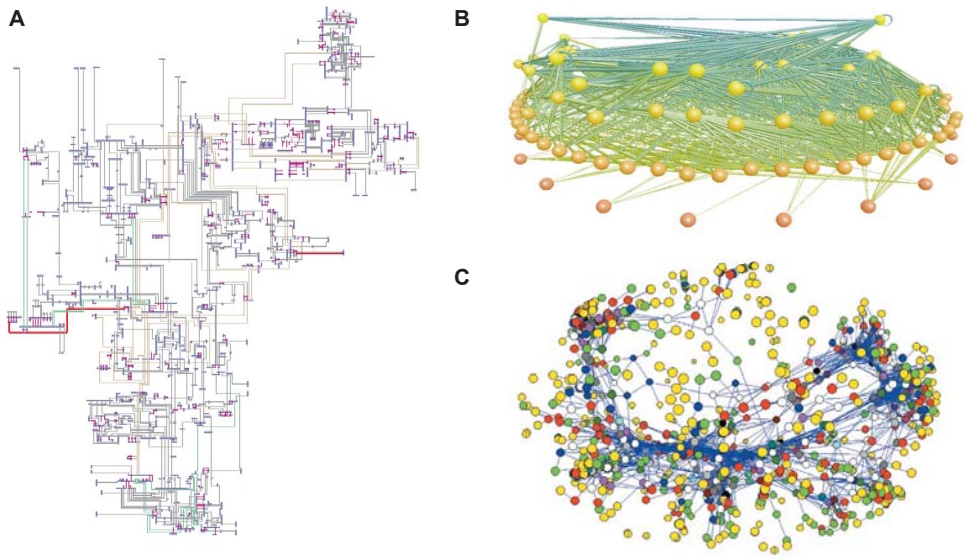

Figure 2.11.: Examples of complex networks. *A*: New York State electric power grid. Generators and substations are shown as small blue bars. The lines connecting them are transmission lines and transformers. Line thickness and color indicate the voltage level: red, 765 kV and 500 kV; brown, 345 kV; green, 230 kV; grey, 138 kV and below. Pink dashed lines are transformers. *B*: Food web of Little Rock Lake (Wisconsin, USA). Nodes mark functionally distinct trophic species containing all taxa that share the same set of predators and prey. Height indicates trophic level with mostly phytoplankton at the bottom and fishes at the top. Cannibalism is shown with self-loops, while omnivory (feeding on more than one trophic level) is shown by different colored links to consumers. Images adapted from (Strogatz, 2001). *C*: Reconstructed functional brain network (Sporns et al., 2004) from human fMRI data (Eguíluz et al., 2005). Vertices are colored according to their degree (yellow = 1, green = 2, red = 3, blue = 4, other colours > 4).

ure 2.12 for definitions). In neural networks in particular, these two characteristics were shown to allow a high signal propagation speed combined with coherent oscillations (Lago-Fernández et al., 2000).

For graph theoretical analysis, networks are represented as vertices (or nodes) that are linked by edges (or connections) as illustrated in figure 2.12. Both denotations are used equivalently. The process of reducing a real network to a network graph requires a careful choice of vertices and edges in order to be able compare the results with other studies (Kaiser, 2011). Regarding the present work, the question arises whether a single neuron is defined as a vertex or if all branching points of neurites are considered as vertices – the latter way was chosen to compare the neuronal networks with a previous study on frontal ganglion cells (FGCs) (Shefi et al., 2002b). Another example is the parcellation of the brain into vertices which should give non-overlapping brain regions as well as assort the vertices such that they exhibit similar connections to other parts of the brain (Honey et al., 2009).

Graphs are differentiated by being directed or undirected, in the latter case it is not distinguished between incoming and outgoing connections. Weighted graphs addition-

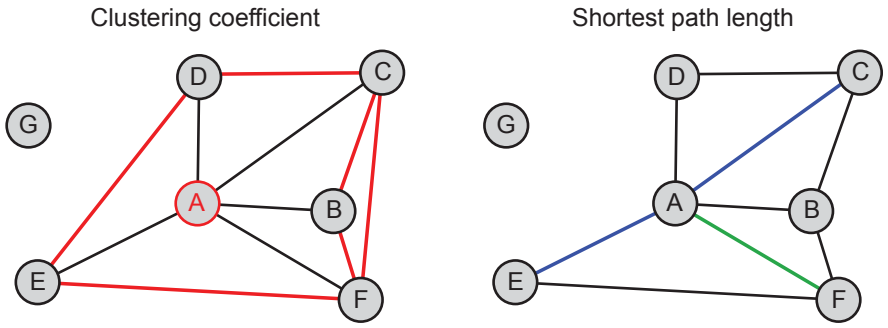

Figure 2.12.: Representation of a network graph composed of vertices (circles) and edges (lines) illustrating the network measures. *Left*: The clustering coefficient C_v of a vertex v is defined by $C_v = 2l_v/k_v(k_v - 1)$, where k_v is the number of neighbors of v and l_v the actual number of connections between the k_v neighbors (Watts and Strogatz, 1998). For vertex A this yields $C_A = 3/5$. *Right*: The shortest path length L is defined as the minimal number of connected vertices that has to be passed between two vertices. In the example, one has for the shortest paths between C & E and A & F, respectively: $L_{C\to E} = 2$ and $L_{A\to F} = 1$. Image adapted from (Kaiser, 2011).

ally include information about the strength of connections (Kaiser, 2011). The basis for the graph theoretical analysis is the mapping of a network to the binary adjacency matrix with entries '1', if a pair of vertices is connected, or '0', if there is no edge (Bollobás, 1998). For undirected and unweighted graphs, this binary matrix is directly obtained. More complex topologies necessitate the additional step of thresholding, which has to be carried out as critically as choosing of vertices and edges (Kaiser, 2011; Bullmore and Sporns, 2009).

Complex networks are characterized by local and global measures (Watts and Strogatz, 1998; Newman, 2003) which are outlined in the following. The local clustering coefficient C_v of a vertex v describes the cliquishness of a neighborhood and the shortest path length L is the smallest number of vertices that has to be passed between two arbitrary vertices, which is a global property (Watts and Strogatz, 1998) (see figure 2.12). These parameters are essentially useful to classify networks regarding their small-world properties in comparison to random or regular networks (Watts and Strogatz, 1998). Further network parameters are the degree or connectivity k_v of a vertex v, i.e., the number of neighbors of v (Strogatz, 2001) and the edge density as the actual number of edges in a network divided by the highest possible number of edges (Kaiser, 2011). Of interest, it was reported that the connectivity of all vertices within small-world networks yields a connectivity distribution and allows a more specific categorization as scale-free, broad-scale and single scale networks (Amaral, 2000). Moreover, the long tails of the distributions point to highly connected vertices – the network hubs, which play an important role in the efficient communication (Bullmore and Sporns, 2009; Freeman, 1977).

New methods in analyzing topological graphs enable the exploration of network mod-

ularity (Girvan and Newman, 2002), hierachy (Ravasz and Barabási, 2003) and centrality (Barthélemy, 2004). These properties of complex networks were also found in brain networks (Bullmore and Sporns, 2009). The *small-worldness* introduced by Humphries *et al.* relates small-world properties to those of random graphs (cf. equation 3.4) (Humphries et al., 2008). M. Kaiser also introduced a correction factor for C_v to specify additionally the "connectedness" of a graph, since the clustering coefficient is not well-defined for a degree of zero or one (Kaiser, 2008). This feature of sparsely connected networks is often ignored in the description, however, for the neuronal networks studied in the present thesis, the correction factor was incorporated in the analysis (see section 5.2.3). The presented parameters give only a short overview of the properties of complex networks. Deeper insights are given in the following reviews (Barthélemy, 2011; Bullmore and Sporns, 2009; Boccaletti et al., 2006; Newman, 2003; Dorogovtsev and Mendes, 2002; Strogatz, 2001).

2.3.2. Understanding neuronal networks – a brain-teaser

As introduced in the previous section, neuronal elements that form the brain belong to the complex networks and, to be more precise, they form small-world networks. The complexity of the brain manifests in the intricate relation of structural and functional networks which challenges researchers from many fields (Sporns, 2011; Stam, 2010; van den Heuvel and Hulshoff Pol, 2010; Bullmore and Sporns, 2009; Chen, 2006; Strogatz, 2001). The vertices of *structural networks* can be imagined as neurons or cortical areas linked by axons or fiber tracts acting as edges that define structural connectivity. In *functional networks*, the edges correspond to correlations in the activity patterns of vertices (different areas in the brain) and give rise to functional connectivity (Kaiser, 2011). A comparative overview of data acquisition and mapping for both types of networks is given in figure 2.13. Although to date it is not yet possible to predict the brain's global functionality from the anatomical connectivity (Bassett and Gazzaniga, 2011), a recent work by Honey and coworkers proclaims auspicious progress in large-scale computational models that were used to relate functional brain dynamics and structural connectivity patterns (Honey et al., 2010).

Beside the aspect of predicting functionality of the brain from structural considerations, there are still many other open questions which is reflected by the manifold applications of network analysis in modern neuroscience (Bullmore and Sporns, 2009; Sporns, 2011). They include the normal development of the brain and effects of aging (Salvador et al., 2005; Fair et al., 2009; Meunier et al., 2009) and the organization of communication in the brain, particularly alterations in disorders like schizophrenia, multiple sclerosis,

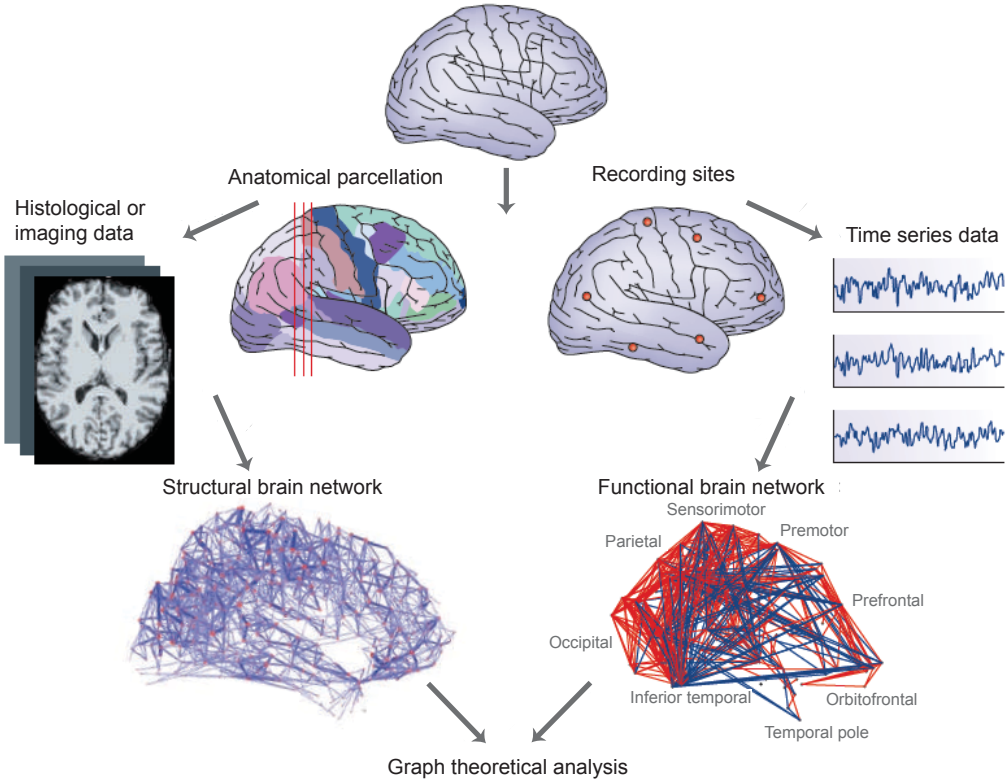

Figure 2.13.: Studying structural and functional brain networks using graph theory. Vertices are defined as anatomical regions of histological, MRI or diffusion tensor imaging data or as electroencephalography or multi-electrode array electrodes. Then a continuous measure of association between vertices has to be estimated, e.g., inter-regional correlations in cortical thickness or spectral coherence between two magnetoencephalography sensors. Compiling all pairwise associations between vertices yields an association matrix, which is often transferred to a binary adjacency matrix or undirected graph by applying a threshold to each matrix element. The adjacency matrix finally allows the calculation of network parameters. Image adapted from (Bullmore and Sporns, 2009).

Alzheimer's disease or epilepsy (van den Heuvel and Hulshoff Pol, 2010). The latter two may be related to "hub failure" (Stam and van Straaten, 2012). Other studies focus on the brains's reaction to injury and its recovery (Nakamura et al., 2009; Wang et al., 2010), network optimization regarding the wiring efficiency (Bassett et al., 2010; Bullmore and Sporns, 2012), the formation of network hubs and long-distance connections (Varier et al., 2011) as well as individual differences such as the intellectual performance (van den Heuvel et al., 2009) or cognitive fitness (Bassett et al., 2009).

The importance of resolving all these questions manifests in a recently launched initiative funded by the European Union – the "Human Brain Project" [1]. It unites researchers from over 80 institutions coordinated by H. Markram. The aim of the project is to simulate the human brain based on three columns: (i) the development of new supercom-

[1] http://www.humanbrainproject.eu

puting technologies and integration of novel results from (ii) neuroscience regarding the structure and function of the brain as well as from (iii) medicine, particularly the investigation of brain diseases. Interestingly, American scientists are planning the start of a project with similar dimensions for the next year – the "Brain Research through Advancing Innovative Neurotechnologies (BRAIN) Initiative" [2] to establish a map of brain activity.

Since studying the human brain in its totality is at least today unimaginable, simpler model system have been frequently used. One of them is the nematode *C. elegans* – it represents the only example of a completely mapped neural network (White et al., 1986). It is built up of 302 neurons connected via 6393 synapses and 890 electrical junctions (Stam, 2010). Among the neuronal networks, the one of *C. elegans* has also been the first for which small-world properties have been demonstrated, i.e., a high clustering coefficient of 0.28 (0.05) and a small shortest path length of 2.65 (2.25) (values in parentheses correspond to values of random networks) (Watts and Strogatz, 1998). The nature of neuronal networks was found to be similar in terms of their complex network properties despite of their origin from different species (Stam, 2010).

A further reduction of the model system consists in the utilization of *in vitro* neuronal networks. They have been used to gain new insights in the principles of self-organization (Shefi et al., 2002a,b) and functional organization (Downes et al., 2012; Bettencourt et al., 2007) (cf. figure 2.14, left). More strikingly, the existence of functional network hubs has been proven for the first time in brain slices (Bonifazi et al., 2009). Advantages are that these systems allow non-invasive, optical long-term observations for up to several weeks (Shefi et al., 2002a) as well as a direct manipulation via electrophysiological stimulation (Downes et al., 2012; Bonifazi et al., 2009). Complete control of the neuronal network properties is still challenging. Nevertheless, Zeck and Fromherz demonstrated that by placing approximately ten cells in a minimal nerve cell circuit on a semiconductor device controlled connections of axons, synapses and dendrites can be achieved (Zeck and Fromherz, 2001) (cf. figure 2.14, middle).

One of the aims of the present work is the characterization of the small-world properties of structural neuronal networks from mouse retinal ganglion cells. Of particular interest was the temporal evolution of the network parameters during the early stages of network formation. Shefi *et al.* described in detail the outgrowth behavior and formation of locust FGC networks (Shefi et al., 2002a). They observed increasing complexity with a maximum between 2 and 3 days *in vitro* followed by a simplification of the net-

[2] http://www.nih.gov/science/brain/

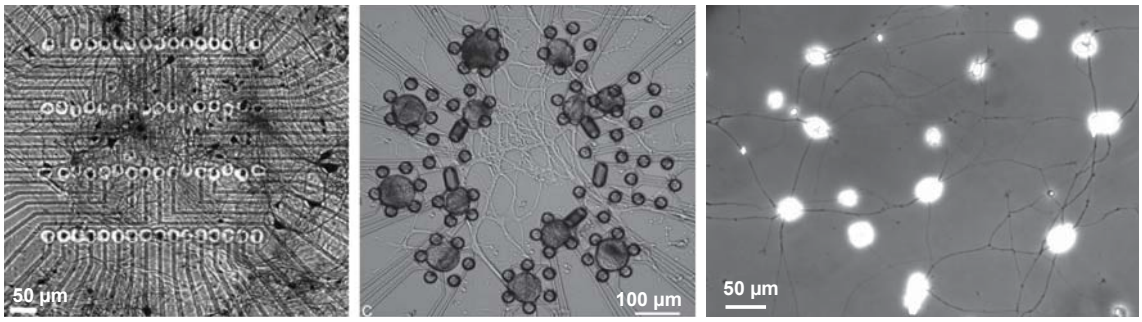

Figure 2.14.: *In vitro* neuronal networks. *Left*: Dense cortical network cultured on a multi-electrode array with a uniform grid of points showing electrodes where neuronal activity is measured for to analyze functional connectivity by means of graph theory. Image from (Bettencourt et al., 2007). *Middle:* Neuronal circuit consisting of eleven synaptically connected cells on a silicon coated semiconductor chip after 2 days in culture. Image from (Zeck and Fromherz, 2001). *Right*: Sparsely connected retinal ganglion cell (RGC) network on a lipid bilayer substrate after 2 days in culture.

work after 1 week. In a second study, they characterized the morphological properties of clustered 6-day-old FGC networks and found that cultured neuronal networks exhibit small-world properties (Shefi et al., 2002b). Recently, functional networks of pre-natal rat dissociated cortical cultures on multi-electrode arrays (MEA) were shown to develop from random networks after 2 weeks *in vitro* to small-world networks after 4 to 5 weeks *in vitro* (Downes et al., 2012). Based on this, the authors extensively discussed the changes of the small-world parameters during network maturation and related them to activity changes such as reduced bursting times.

Finally, a few remarks about the behavior of primary retinal ganglion cells (RGCs) shall be made as they were used as model system in the present study. *In vivo* RGCs alone never were observed to form networks. Instead the cells connect their dendritic arborization to bipolar and amacrine cell axons on the one side and form the optic nerve via fasciculation of long RGC axons on the other side (Bear et al., 2007). Defasciculation and branching only occur when RGCs reach their targets in the brain. Thus, *in vivo* external signals (from glia cell precursors, surrounding neurons, guidance molecules) block the formation of the homologous connections between RGCs that can be observed *in vitro* (cf. figure 2.14, right). From previous studies it is known that RGCs recover from the dissection and regrow neurites *in vitro* between 2 and 4 days after plating (Claudepierre et al., 2008).

3. Materials and Methods

3.1. Preparation of DODAX multilayers for ATR spectroscopy

Chloroform ($CHCl_3$) and potassium iodide (KI) (purity ≥ 99.5 %) were purchased from Merck (Darmstadt, Germany). Dioctadecyldimethylammonium bromide (DODAB) and 1,2-Dimyristoyl-*sn*-Glycero-3-Phosphocholine (DMPC) were obtained from Sigma-Aldrich (≥ 98 %, Schnelldorf, Germany). The other three DODA halides were either not commercially available or not of adequate purity. Therefore, DODAC and DODAI were produced from DODAB in a water-isopropanol solution with up to twentyfold excess of potassium chloride (KCl, > 99.5 %, Roth, Karlsruhe, Germany) or KI, respectively. Analog ion exchange failed for DODAF, probably due to strongly bound water molecules which shield the fluoride charge preventing substitution of bromide ions. Instead, it was prepared by precipitation of insoluble AgBr after addition of an equimolar amount of AgF (≥ 99 %, Fluka, Buchs, Switzerland). This behavior already points to the different properties of DODA's counterions and will be discussed in sections 4.2 and 4.3. Detailed protocols for the preparations of DODAC, DODAI and DODAF as well as analytical energy dispersive x-ray (EDX), matrix-assisted laser desorption/ionization time of flight (MALDI-TOF) and nuclear magnetic resonance (NMR) spectroscopy data are given in appendix B.1 for all lipids. The structure of DODAX lipids is given in figure 3.1. Chloroformic solutions for all lipids were prepared at a concentration of 10 mg/mL and stored at -20 °C.

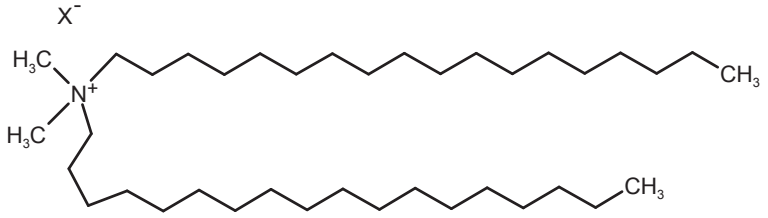

Figure 3.1.: Chemical structure of DODAX (Okuyama et al., 1988).

3.2. ATR FTIR spectroscopic measurements

A schematic of the setup for ATR experiments is shown in figure 3.2. For all experiments a zinc selenide (ZnSe) ATR crystal with the dimensions 72 x 10 x 6 mm^3 and an incident angle of 45° (LOT Oriel, Darmstadt, Germany) was used. The crystal was carefully cleaned to avoid scratching using tissue soaked with $CHCl_3$, methanol (CH_3OH) and ethanol (C_2H_5OH). Lipid bilayer multistacks were prepared by spreading of 80 µL chloroformic DODAX solution on the clean ATR crystal yielding a film thickness of 2 µm. The crystal with the sample was mounted on a horizontal Benchmark unit (Specac, Orpington, UK). After evaporation of the solvent, ATR FTIR measurements were carried out by a Digilab Excalibur FTS 3100 spectrometer (Agilent, Böblingen, Germany) equipped with a globar source and a DTGS detector working at ambient temperature. The interior of the spectrometer was flushed with nitrogen to reduce water vapor absorptions. Data acquisition was performed automatically by a Visual Basic routine using the software Resolutions Pro 4.0 (Agilent).

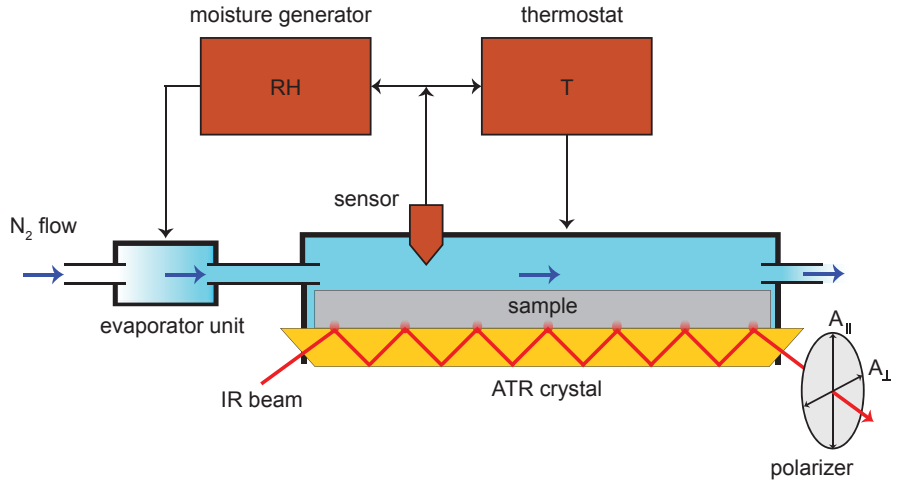

Figure 3.2.: Schematic of the setup for temperature- and hydration-dependent ATR experiments. The ATR crystal is mounted on a holder unit and covered by a copper block thermostated by flowing water. The closed sample compartment is exposed to a flow of nitrogen (~ 100 mL/min). The lipid film (thickness does not refer to scale) on the ATR crystal is hydrated at a well-defined temperature and humidity, which are both adjusted by a moisture generator (HumiVar). Image adapted from (Binder, 2003).

ATR Spectra were recorded under parallel and perpendicular polarization with regard to the incident angle of the IR beam using a motorized KRS-5 wire grid polarizer (LOT Oriel, Darmstadt, Germany). Before taking the absorbance spectra $A_{\parallel}$ and $A_{\perp}$ of the sample, background and water vapor (for later subtraction) spectra were taken each by co-adding 256 scans and with a resolution of 4 cm^{-1}. The relative humidity (RH) was adjusted between 2 - 98 % RH using a moisture generator (HumiVar, Leipzig, Germany) with $\Delta RH = \pm 0.5$ % and $\Delta T = \pm 0.1$ K (Binder, 2003). The sample temperature was

controlled by a circulating water bath (Julabo, Seelbach, Germany) with an accuracy of $\Delta T = \pm 0.05\,K$. Further details of the setup were described by H. Binder (Binder, 2003). Lipid films were hydrated with either Millipore water or D_2O (Chemotrade, Leipzig, Germany). The low hydration of DODAX lipids impeded the study of isotopically diluted (HOD) water's structure. Even at highest hydration, the intensity of the HOD stretching bands in the ATR spectra was so low that it was impossible to determine molecular orientations.

The lipids were treated as described in table 3.1 to assure reproducible experimental conditions.

Category	Experimental conditions
***O* Initial:** freshly prepared lipid film	Immediately after preparation and solvent evaporation, $\theta = 25\,°C$, relative humidity (RH) was 50 %
***A* Heating:** dry lipid film after drying by heating	Stepwise heating to $\theta = 65\,°C$, $\Delta T = 2$ - 5 K, 60 min equilibration time, RH 50 % (In DODAF, a small amount of water remained at 65 °C. Thus, the sample was heated to 85 °C.)
***B* Cooling:** dry lipid film after heating and consequential cooling	Stepwise cooling to $\theta = 25$ °C, $\Delta T = 2$ - 5 K, 60 min equilibration time; DODAB and DODAI were used at the room's RH $\leq$ 50 %, DODAC and DODAF were used at RH $\leq$ 3 % (at higher humidity water will be adsorbed)
***C* Rehydrated:** lipid film after being hydrated again	Hydration at 80 % RH, 4 h equilibration time, $\theta = 25\,°C$, hydration band not observed for DODAI

Table 3.1.: Differently treated thick films for ATR FTIR spectroscopic measurements

3.3. Evaluation of dichroic data

Prior to the analysis of molecular orientations, Resolutions Pro was used to subtract water vapor and CO_2 absorptions from the spectra and perform an ATR correction ($n_{ZnSe} = 2.40$, $n_{lipid} = 1.42$, $\omega = 45°$) followed by a baseline correction. Band fitting was carried out with the Multipeak Fitting package of Igor Pro 5.03 (WaveMetrics, Portland, OR). The positions of absorption band maxima were determined by band fitting of the non-polarized spectra with an absorbance $A(\nu) = A_{\parallel}(\nu) + 2.54\,A_{\perp}(\nu)$ corresponding to the integral absorbance of the isotropic sample (Binder and Schmiedel, 1999). Initial fit parameters like peak positions, widths and intensities of OH stretching bands based upon a study by Liu and coworkers (Liu et al., 2004) (see section 4.3.1). Additional shoulders and bands were only included in the analysis, if they were already visible in the original spectra.

All band components were fitted by a Gaussian profile. The errors given correspond to errors resulting from the fit. For the peak positions errors were found to be $< 0.2\,\mathrm{cm}^{-1}$ for the narrow CH_2 stretching bands. For the broader ν(OH) bands and ν(OD) bands, errors of $< 20\,\mathrm{cm}^{-1}$ for peak 1 and $< 5\,\mathrm{cm}^{-1}$ for peak 2 - 6 (see chapter 4) were determined.

From the measured absorbances $A_{\parallel}$ and $A_{\perp}$ the dichroic ratio R and IR order parameter S_{IR} were determined using equations 2.1. The molecular orientation angle θ_{μ} of water and lipid molecules with regard to the normal of the ATR crystal as well as the lipid's chain order parameter S_{θ} were calculated using equations 2.2 and 2.3. The values of S_{θ} are given for lipid films in the state D (cf. table 3.1) which were heated at least once above the main transition – a procedure commonly used to reduce inhomogeneities when preparing the lipid membranes (Lewis and McElhaney, 2007; Feitosa et al., 2000) .

3.4. Preparation of tethered and supported lipid bilayers as substrates for neuronal growth

Neuronal outgrowth, most notably in conjunction with mechanosensitive behavior, is frequently studied on polyacrylamide (PAA) hydrogels with tunable elasticity (Franze and Guck, 2010). Here a different approach was followed: neuronal cells were seeded on lipid bilayers distinguished by their membrane fluidity. Therefore, tethered lipid bilayers (tBLs) were used as substrates with high membrane fluidity. These bilayers constitute a model system which mimics cell-cell contacts and allows the variation of the substrate viscosity as well as the linker mobility (Minner, 2010). Results were compared with data from neuronal growth on conventional supported lipid bilayers (sBLs). Both bilayer types were deposited on glass substrates by Langmuir-Blodgett (LB) / Langmuir-Schäfer (LS) transfer using a Langmuir trough (Nima, Espoo, Finland) as illustrated in figure 3.3. This device is equipped with a Wilhelmy pressure detector, movable barriers for the compression of the lipid monolayer and a dipper unit for the substrate coating.

The phospholipid 1-palmitoyl-2-oleoyl-*sn*-glycero-3-phosphocholine (POPC) was purchased from Avanti Polar Lipids (Alabaster, AL) and used as provided. The lipopolymer 1,2-distearoyl-*sn*-glycerol-poly(2-methyl-2-oxazoline)$_{50}$ ($PMOx_{50}$) was synthesized by the group of Professor R. Jordan (TU Dresden, Germany) as described previously (Purrucker et al., 2005; Jordan et al., 2001) and dissolved in $CHCl_3$. 1,2-distearoyl-*sn*-glycero-3-phosphoethanolamine-*N*-[succinimide ester (polyethylene glycol)-2000] (PEG2000-NHS) was prepared by hydrogenation (Alker et al., 1997) of PEG2000-Maleimide by the group of Professor C. A. Naumann (Purdue University, Indianapolis, IN). tBLs were deposited on round glass coverslips (∅ 4 cm, 631-0177, VWR International,

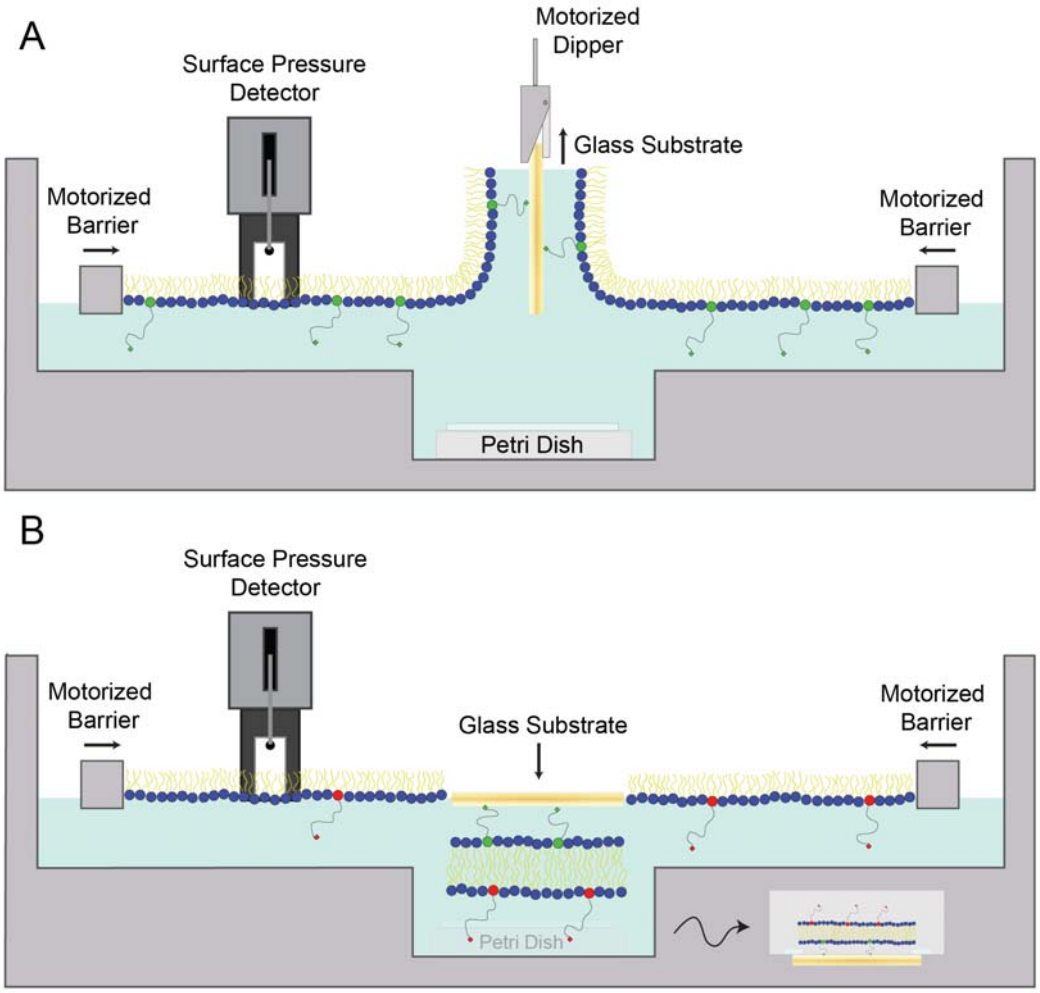

Figure 3.3.: Preparation of a tethered lipid bilayer by Langmuir-Blodgett (A) and Langmuir-Schäfer (B) transfer

Dresden, Germany), which were cleaned with Hellmanex solution (Sigma-Aldrich, Schnelldorf, Germany) in a sonicating water bath (Branson Ultrasonics, Danbury, CT) at 40 °C for 60 min. Afterwards, they were extensively rinsed with Millipore water, hydrophilized in a plasma cleaner (Harrick, Ithaca, NY) for 2 min and finally stored until use in Millipore water (not longer than two days).

The composition of the inner leaflet of the bilayer can be used to vary the bilayer fluidity by changing the lipopolymer concentration. Two "extreme" cases were chosen, i.e., a very low lipopolymer concentration for the most fluid membranes (POPC + 5 mol % $PMOx_{50}$) and no lipopolymer at all for the the most viscous substrates (pure POPC). The outer leaflet for each bilayer system contained POPC + 5 mol % PEG2000-NHS. The latter compound allows the binding of laminin, an ECM protein that promotes cell attachment as illustrated in figure 3.4. All solutions were prepared by dilution in $CHCl_3$ to yield final concentrations of approximately 1 g/L.

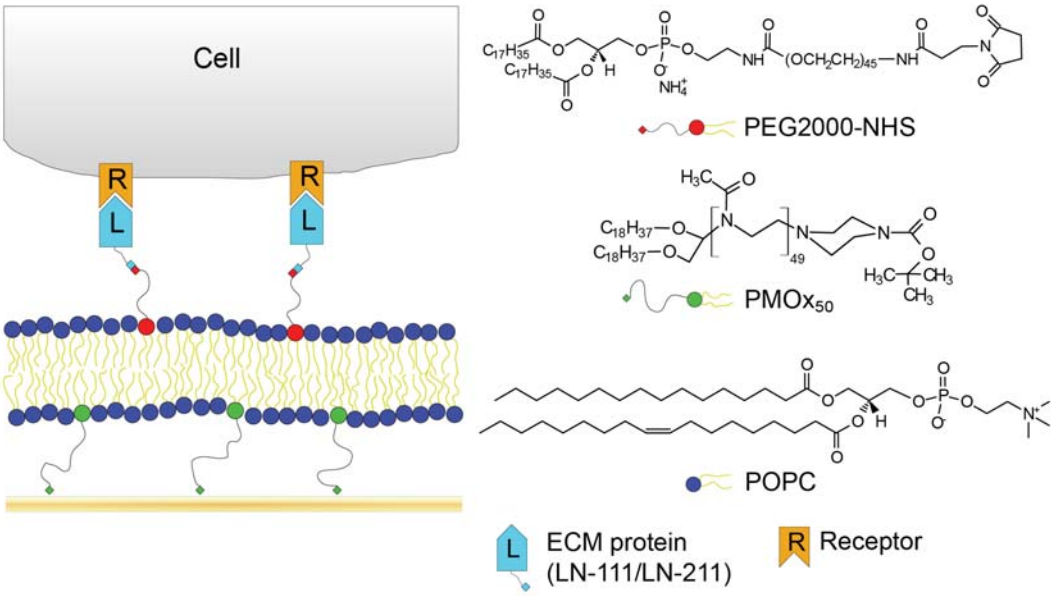

Figure 3.4.: Schematic of tBL as cell substrate

Since tBLs and sBLs were used as substrates for cell growth, the coated glass substrate had to be combined with a Petri dish. Therefore, a hole of ∅ 3 cm was cut into the bottom part of a Petri dish (∅ 52 mm, VWR, 391-8033). Furthermore, a ring of vacuum grease was added at the inner rim of the hole for later sealing. Then the Petri dish was placed upside down on the bottom of the dipping unit's cavity as indicated in figure 3.3 A. Prior to the bilayer fabrication, the teflon surface of Langmuir trough was thoroughly cleaned with $CHCl_3$, CH_3OH and C_2H_5OH. The purity of the subphase was controlled by compression of the subphase's surface in the absence of lipid molecules. The trough was regarded as clean if the surface pressure did not increase more than 0.1 mN/m after full compression. Otherwise, it was cleaned using Hellmanex solution followed by repeated thoroughly rinsing with Millipore water. tBLs and sBLs were prepared by spreading the lipid solution for the inner leaflet (100 nmol) on the Langmuir trough filled with Millipore water. The amphiphilic molecules self-assemble to a *Langmuir monolayer* by pointing the hydrophilic polar head groups and polymer moieties of the lipopolymers into the aqueous subphase whereas the hydrophobic chain groups are exposed towards the air. Lipid monolayers were compressed to a surface pressure of 30 mN/m, which corresponds to an average area per lipid of 63 $Å^2$, and were allowed to stabilize for 20 min. LB transfer to the glass coverslip as shown in figure 3.3 A was carried out at a dipping speed of 1 mm/min. A slow transfer to the substrate was important to prevent a lipid/lipopolymer phase separation (Seitz et al., 2011; Purrucker et al., 2005).

For the outer leaflet, the Millipore subphase was exchanged, new lipid solution was

spread on the trough and allowed to equilibrate as before. The bilayer was completed by LS transfer (see figure 3.3 B), i.e., the coverslip with the LB layer was pushed horizontally through the air/water interphase and stuck to the Petri dish. The final sample was turned below the water surface and lifted off the trough such that the bilayer was covered with enough Millipore water (~ 8 mL). Keeping the tBL permanently in an aqueous environment is essential to maintain the tBL intact. Then the dish was pressed down on a kimwipe to form a good seal and assure a flat attachment of the coverslip. In the last step, tBLs were coated with ECM-proteins, laminin-1 (LN-111) for both NG108 cells and RGCs as well as laminin-2 (LN-211) for RGCs only. Of interest, LN-211 is also known as merosin, but here the new term is used according to an agreement for the simplification of laminin nomenclature (Aumailley et al., 2005). Thus, an excess of LN-111 (and where needed LN-211) diluted in 2 ml phosphate buffered saline (PBS) was carefully added to the Petri dish and incubated for 1 h at 37 °C. Unbound LN molecules were removed by rinsing twice with PBS. The coating protocol is given in appendix C.2.1. After this step, the substrates were ready for plating of cells.

3.5. Analysis of the substrate mobility

Fluorescence recovery after photobleaching (FRAP) experiments were performed to roughly estimate the lateral lipid diffusion within tBL and sBL substrates (see figure 3.5). Bilayers were in principle prepared as described above (section 3.4) with the modification of adding a fluorescent dye to the outer leaflet. Therefore, 0.5 mol% of Texas Red® 1,2-dihexadecanoyl-*sn*-glycero-3-phosphoethanolamine, triethylammonium salt (TR-DHPE) or *N*-(7-nitrobenz-2-oxa-1,3-diazol-4-yl)-1,2-dihexadecanoyl-*sn*-glycero-3-phosphoethanolamine, triethylammonium salt (NBD-PE) (both Molecular Probes/Invitrogen, Darmstadt, Germany) were mixed to the lipid solution. Experiments were carried out at room temperature on an inverted microscope (DMIRB, Leica Microsystems, Wetzlar, Germany) equipped with a cooled EMCCD camera (iXon DV887 back-illuminated, Andor Technologies, Belfast, UK) and a 63x oil immersion objective (HCX PL, NA 1.25, Leica Microsystems). Bleaching was achieved by a conventional mercury lamp and an iris diaphragm mimicking "uniform disk illumination". Image acquisition and shutter control were performed using the Andor software.

The bleaching time t_{bleach} was 1 min for tBLs and 2 min for sBLs, exposure times were 20 - 35 ms for tBLs and 100 - 150 ms for sBLs. The observation increment varied between 10 s and 20 s. Due to the simplicity of the experimental setup, a simple model was used evaluate the experimental data. It assumes Brownian motion with an immobile fraction

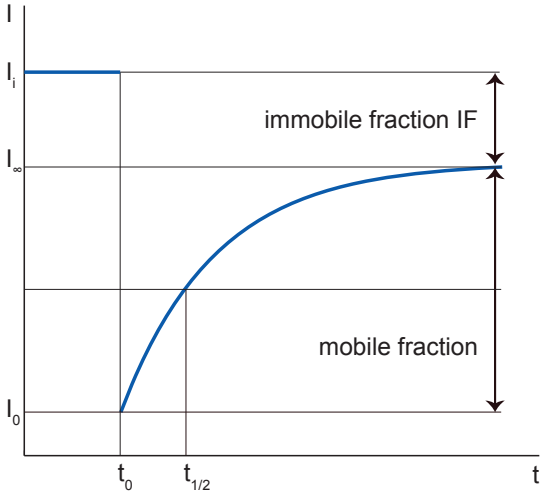

Figure 3.5: Schematic of fluorescence recovery after photobleaching (FRAP). When a spot in a fluorescent lipid bilayer is bleached at time t_0, the intensity decreases to from I_i to I_0. Unbleached lipid molecules undergoing Brownian motion diffuse into the bleached area and lead to a recovery of the fluorescent signal until its full recovery (I_∞). The characteristic diffusion time, $t_{1/2}$, defined as the time at which half of the fluorescence has recovered, is used to determine the diffusion coefficient D. Image adapted from (Reits and Neefjes, 2001).

of lipids, *IF*, (Axelrod et al., 1976) (see figure 3.5). FRAP curves were normalized such that $I(t{=}0) = 1$ before the bleaching and $I(t_{\text{bleach}}) = 0$ directly after bleaching. The normalized fluorescence curves were fitted by a single-exponential function to obtain the half-time of the fluorescence recovery, $t_{1/2}$, and the immobile fraction $IF = [1 - I(t \to \infty)] \cdot 100\,\%$. The lateral diffusion coefficient, D, was determined using the relationship:

$$D = 0.224 \cdot \frac{r^2}{t_{1/2}} \tag{3.1}$$

where r is the radius of the bleaching spot (Axelrod et al., 1976). Its size was 102 µm for sBLs and 54 µm for tBLs.

The accurate determination of $t_{1/2}$ requires a full recovery of the fluorescence signal to I_∞. However, the observation time of FRAP experiments is limited. Thus, I_∞ can only be determined from the fitted curves which leads to a high error of both absolute values of I_∞ and $t_{1/2}$ (up to 10%). Another error source is the weak illumination of the bleach spot, which can be determined with an accuracy of ~ 5 pixel (corresponding to 10 % for sBLs and 20 % for tBLs). Thus, the absolute values of the diffusion coefficients exhibit significant experimental errors.

3.6. Neuronal cells

In the framework of the present thesis, two different types of neurons were cultured on tethered bilayers. These neuronal cells are briefly introduced in the following. Detailed protocols of the cell culture procedures and compositions of the growth media are given in appendix B.4.

3.6.1. The NG108-15 cell line

The NG108-15 cell line is an immortalized mouse neuroblastoma cell line, which was developed by Hamprecht and coworkers (Hamprecht et al., 1985). It was formed by fusing mouse N18TG2 neuroblastoma cells with rat C6-BU-1 glioma cells in the presence of inactivated Sendai virus. Neuroblastoma is a malignant tumor derived from ganglion cells which are interneurons that convey information from retinal cells to the brain. Glioma is a tumor derived from glial cells. NG108-15 cells spontaneously grow neurites in culture (see figure 3.6, left). Furthermore, NG108 cells are known to form synapses that are at least functional on the presynaptic side. NG108 cells are very convenient model neurons since, first, they are a quite robust cell line, i.e., the cells slightly more tolerate suboptimal culture conditions during the measurements. Second, NG108 cells do not require growth factors such as NGF for neurite outgrowth which instead can be enhanced by using a serum-reduced growth medium (Wu et al., 1998). Therefore, for normal NG108 cell culture a growth medium with 10 % fetal bovine serum (FBS) was used, whereas for experiments the FBS content was decreased to 2.5 % (cf. appendix B.4).

3.6.2. Primary retinal ganglion cells

Primary neurons constitute the most physiologic model system. The primary cells are fully differentiated, do not divide and can be cultured only for several weeks. Furthermore, they are more delicate than cells from cell lines. However, they better resemble the cells' behavior *in vivo* and are, therefore, widely studied to confirm experimental results obtained from cell lines. Today many different types of neurons from both the central nervous system (CNS) as well as the peripheral nervous system (PNS) can be prepared. Here, primary retinal ganglion cells (RGCs) of mice were used (see figure 3.6, right). They belong to the CNS and project visual information from the retina to the brain via the optic nerve (Bear et al., 2007). RGCs can be highly purified ($\sim$ 99 %), well maintained in the absence of glial cells and are able to regrow neurites and form 2D neuronal networks *in vitro* (Steinmetz et al., 2006). The primary cells were extracted from mice according to the guidelines of the Laboratory Animal Care and Use Committee of the University of Leipzig and kindly provided by Professor T. Claudepierre (Augenklinik, Medizinische Fakultät, Universität Leipzig). It has been shown that LN-211 which is present in the retina and the optic nerve during early development promotes neurite outgrowth in RGCs (McKerracher et al., 1996; Morissette and Carbonetto, 1995; Cohen and Johnson, 1991). However, first experiments with a pure LN-211 coating showed that the neurites were attached very loosely. Thus, mixtures of LN-211 and LN-111 were used to avoid a detachment of the cells (see appendix C.2.1).

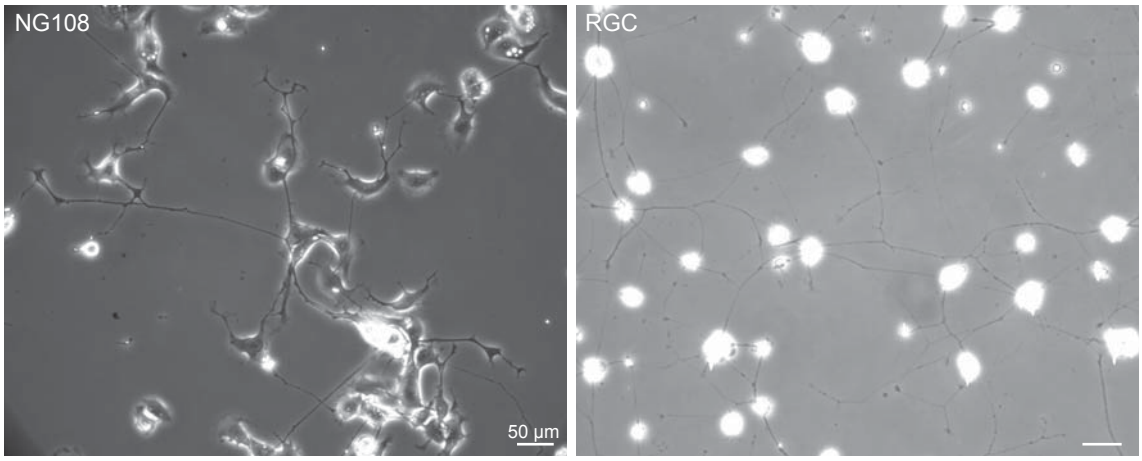

Figure 3.6.: Phase contrast images of investigated neuronal cells. *Left:* NG108 cell line. *Right:* Primary retinal ganglion (RGCs) from mice. Scale bars are 50 µm.

3.7. Image acquisition

In the present work, first the mechanosensitive response of *single* neurons was investigated by analyzing different aspects of neurite outgrowth. The second question addressed the *collective* cell growth, i.e., the formation of complex networks. Phase contrast microscopy, a standard technique to study living cells, was used for both set of experiments. Therefore, the sample was mounted on an inverted microscope (DMIRB, Leica Microsystems). A Petri dish was placed in a custom-made heater to keep the cells at 37 °C and closed with a special teflon top. The latter was developed in our laboratory and had two connections to apply a gentle flow of moistened synthetic air (Air Liquide, Düsseldorf, Germany) with 5 % CO_2 over the medium in the dish. Images were taken for all experiments using a 20x (N PLAN L, NA 0.40 CORR PH1) phase contrast air objective (Leica Microsystems).

First experiments were carried out with NG108 cells on tBL and sBL substrates, respectively, after approximately three days in culture. At this time, cells had grown neurites and formed small networks. Single images at ~ 100 different positions were taken with a Dalsa DS-21-02M30 CCD camera (Dalsa Cooperation, Krailling, Germany) controlled by a LabVIEW (National Instruments, Austin, TX) program. A 0.5 C-mount was used to get a large overview of the Petri dishes.

In the second set of experiments, the growth of primary RGCs on lipid bilayer substrates was examined by time-lapse video microscopy. The inverted microscope was now additionally equipped with a motorized x-y-stage (DMSTC, Leica Microsystems) and an E-660 Piezo Driver (PI Physik Instrumente, Karlsruhe, Germany) for the adjustment of the objective height. Since primary RGCs grow neurites faster than NG108 cells,

measurements started 17 - 20 h after plating and ended after 38 - 41 h *in vitro* when complete networks had formed. Images were taken every 3 or 5 min with an ORCA-285 IEEE 1394-based CCD camera (Hamamatsu Photonics Deutschland, Herrsching am Ammernsee, Germany). A LabVIEW program controlling camera and movable stage was used for an automated image acquisition of long-term image series of neuronal networks at ten different positions of the same Petri dish. Cells were viable for at least three days *in vitro*, which was apparent from the steadily outgrowth of new processes. However, sometimes neuronal beading was observed, which is discussed in section 3.8.3.

3.8. Quantification of neurite growth and network formation

When analyzing neuronal growth at cellular or network level, one encounters two difficulties which complicate a fully automated tracking of nodes and edges or even make it impossible. The first consists in the exact tracing of axonal and dendritic arbors, which is extraordinarily essential to understand neuronal morphology and functionality (Cuntz et al., 2010). For this reason, scientists from allover the world launched the DIADEM challenge (short for DIgital reconstruction of Axonal and DEndritic Morphology) (Brown et al., 2011). However, in these data sets the visualization often is improved by utilizing dye molecules. Against it, in the present study phase contrast microscopy was used which makes the image analysis more difficult but has the advantage of being a non-invasive technique. The second difficulty concerns the extraction and analysis of the connectivity information. Also this question unified brain power and stimulated the setting up of the Matlab-based Brain Connectivity Toolbox which provides an extensive collection of complex network measures (Rubinov and Sporns, 2010). An extension is the recently published Graph-Theoretical Analysis Toolbox (GAT) which focuses on the comparison of structural and functional brain networks (Hosseini et al., 2012) and underlines the high activity in this research area. In the next sections, the tracing and mapping procedures used within this work are presented.

3.8.1. Neurite length and branching

The outgrowth behavior of neurites in dependence of the substrate viscosity was characterized by evaluating the maximal neurite length and number of branches per outgrowth. Therefore, the processes where traced using *NeuronJ* (Meijering et al., 2004), a plug-in of ImageJ (National Institutes of Health, Bethesda, MD). Although the program was origi-

nally written for fluorescence data, it also allows to change the neurite appearance from white to dark making it suitable for phase contrast data. In a first step, the program automatically determines the likelihood of being part of a neurite for each single pixel in the image. In the second step, the user defines a neurite starting point from which the trace is computed by connecting consecutive pixels which most likely form the centerline of the neurite (Meijering et al., 2004). The parameters used for the tracing procedure were: Hessian smooth scale: 2, Cost weight factor: 0.7, Snap window size: 9 x 9, Path-search window size: 2500 x 2500, Tracing smoothing range: 4, Tracing subsampling factor: 4. Since not all cells had grown extensive processes, traces were setup for approximately 90 - 100 cells with long neurites cultured on both substrates.

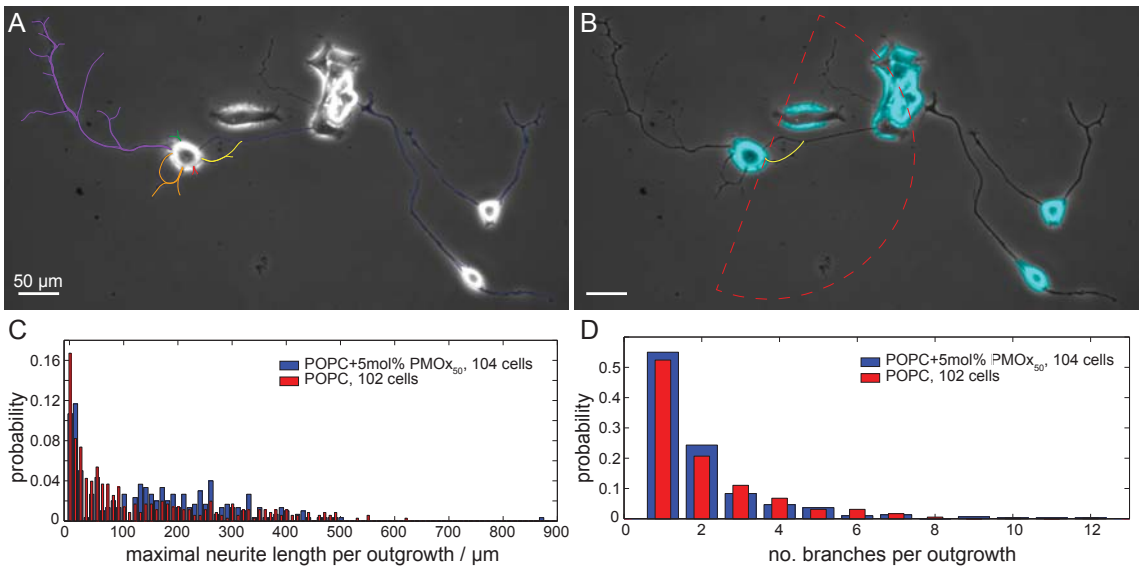

Figure 3.7.: Quantification of neurite growth. *A:* Neurites of NG108 cells were traced using *NeuronJ* (blue). Growth parameters were analyzed per outgrowth (shown in different colors). *B:* Definition of a semi circle in direction of each extending neurite and fitting of the neurons' somatic areas (cyan overlay). *C* and *D*: Distributions of the maximal neurite length and branching per outgrowth. Scale bars correspond to 50 µm.

Figure 3.7 A displays three NG108 cells whose neurites were traced with NeuronJ (shown in blue). Moreover, the NeuronJ determines the coordinates of each individual neurite which constituted the basis for further analysis with a Matlab (The MathWorks Inc., Natick, MA) program developed together with M. Knorr. It assorted the traces to the corresponding outgrowth and calculated the maximal neurite length and number of branches per outgrowth (figure 3.7 C and D). Furthermore, the program determined the areas of the cell somata and allowed to define a radius of a semi circle in direction of the growing neurite or full circle (see figure 3.7 B) and computed for each neurite the area covered with other cells within that circle. This quantity was used to investigate whether the neurite length is dependent on the cell density, i.e., the free space available

for extending processes. The statistical significance of the differences between the results on tBLs and sBLs was determined with ANOVA tests for normally distributed data and Kolmogorov-Smirnov tests for not normally distributed data using a significance level of $p < 0.05$.

3.8.2. Growth speed analysis

Analysis of the neurite outgrowth speeds required neurite tracing in successive image frames. Therefore, the software *NeuronGrowth*, in particular the function *Neurite Tracings*, was used which is also a plug-in of ImageJ (Fanti et al., 2008, 2011). The tracking procedure was described in detail by (Fanti et al., 2011). In brief, the first frame of an image series is used to trace neurites by ridge detection similar to the algorithm of (Meijering et al., 2004). After manually defining a starting point of the neurite, the cursor is roughly moved along the neurite. The plug-in computes the optimal centerline of the neurite by means of a so-called live-wire algorithm which optimizes the path between the starting point and the actual cursor position as well as the critical points that characterize the neurite. Tracing for the entire image series is realized by first computing a neurite's initial point in the successive frame and then transferring the critical points to the next frame. Based on these data, the positions of the new critical points are adapted using an active contour (snake) and, afterwards, the live-wire algorithm is applied to trace the neurite in the successive frame. All neurites were traced by employing the pre-defined default settings (*Live wire* - gamma: 14, smooth: 9; *Snake* - elastic energy: 1, curvature ernergy: 3, image energy: 11, search window size: 7; *Descriptor* - size: 5, search window size: 21; *Ridge tracking* - curvature: 8, tracking angle: 20).

In this study, the growth behavior of RGCs was investigated with regard to the long-term outgrowth speed on one hand and short-term outgrowth and retraction rates on the other side. The first was examined between 17 - 20 h and 38 - 41 h after plating of the cells. During this time, the neurites grow considerably as shown in figure 3.8 A. Neurite tracking was carried out for images acquired in time intervals of one hour. The speed of individual neurites was calculated as ratio of the neurite length and the growth time corresponding to the neurite's age. The growth time was considered to be 0 at the beginning of the observation, i.e., "offset times" when samples where still in the incubator were not taken into account. Note that neurites naturally start growing at any time. Thus, a neurite like N13 (cf. figure 3.8 B), which started growing out later, was only traced for 10 h. Furthermore, the outgrowth and retraction rates of young neurites were analyzed during the first 2 h of observation. Therefore, neurites were traced in every frame, i.e., in intervals of 3 or 5 min. The rates were determined as ratio of the change of neurite length between

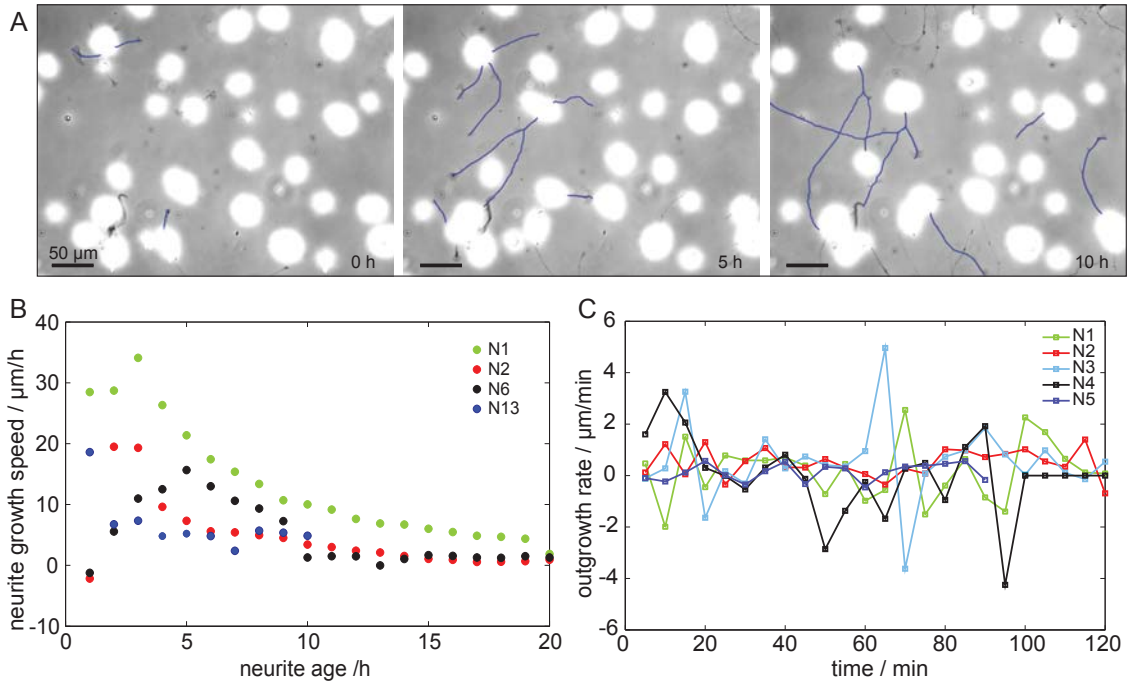

Figure 3.8.: *A:* Phase contrast images of RGCs cultured on tBLs at the beginning of the observation, after 5 h and 10 h, respectively (from left to right) with traces (blue) generated using *Neuron Growth*. Scale bars are 50 µm. *B:* Long-term outgrowth speed of single neurites in dependence of the neurite age. *C:* Retraction and protrusion rates of single neurites during the first two hours of observation.

to successive image frames and the time interval. Thus, positive rates correspond to a neurite growth, while negative rates indicate a retraction (cf. figure 3.8 C).

3.8.3. Graph theoretical analysis of the network formation

In this study, the properties of neuronal RGC networks were characterized using graph theory as described previously (Barthélemy, 2011; Boccaletti et al., 2006; Strogatz, 2001). Therefore, the topology of the networks was mapped using the Adjacency Matrix GUI (Chuang, 2005) from Matlab. The original program enabled the definition of vertices and edges and returned the adjacency matrix A. It was modified to load phase contrast images of arbitrary size in the background (overlaid with vertices and edges). Furthermore, it was extended to also determine the coordinates of the vertices for the analysis of distances between vertices. It might be intuitive to define neurons as vertices and synapses as edges; nevertheless, in this study neurons, synapses, synapse-like connections between neurites of the same cell, growth cones and all branching points were considered as vertices of the network (see figure 3.9). This approach is in agreement with a previous study on morphological 2D neuronal networks (Shefi et al., 2002b). Since all these structures contribute to the network's complexity, it can be assumed that they also

influence the information processing through the network. The temporal evolution of the networks was examined by graphically mapping frames in intervals of 90 min. In ambiguous cases, previous and successive image frames were considered to define real vertices and edges.

During the development of RGC networks, neurons underwent effects of aging. The first observation was that retracting neurites showed enhanced occurrence of neuronal beading, i.e., the formation of bulbous structures. However, the cells continued the outgrowth of neurites with large growth cones and many filopodia. This indicated that the neurons were still viable. Secondly, some neurites thinned out and finally disappeared. Therefore, neurites were included in the analysis as long as there was still visible retrograde transport along the neurite.

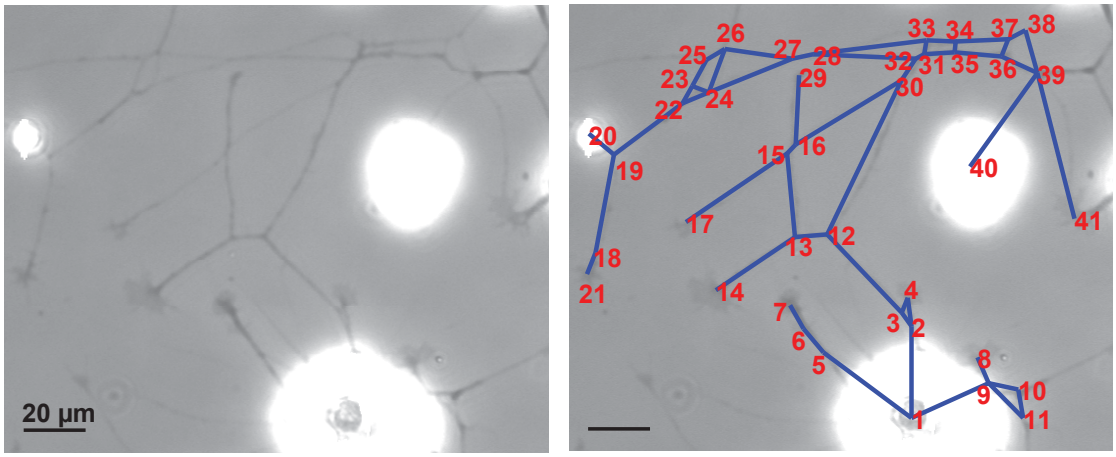

Figure 3.9.: *Left:* Phase contrast image of a small section of an RGC network. *Right:* Corresponding topological graph. Somata, synapses, growth cones and all branching points are defined as vertices (red numbers). Two neighbored vertices are connected by an edge as illustrated by the blue lines.

For the mapping of topological graphs, all vertices and edges between two adjacent vertices were assumed to be identical, i.e., any directionality information was neglected. Further, multiple connections between two vertices were disregarded (Shefi et al., 2002b). Hence, resulting graphs were undirected and unweighted. Let $v_1, v_2, \ldots, v_n$ be the vertices of the graph abstracted from the neuronal network images. Then, the adjacency matrix $A = a_{ij}$ of order n, which characterizes the graph, is symmetric and given by (Bollobás, 1998):

$$a_{ij} = \begin{cases} 1 & \text{if } v_i \text{ and } v_j \text{ are directly connected by an edge} \\ 0 & \text{otherwise} \end{cases} \tag{3.2}$$

The network is characterized by several parameters such as the degree k of a vertex v_i, the shortest path length L between a pair of vertices v_i and v_j, the clustering coefficient

C_v and the so-called small-worldness S. The degree k of a vertex v_i describes the node connectivity, i.e., the number of all other directly connected vertices. $k(v_i)$ is determined from the adjacency matrix A by summing up all elements in a row (or column) i. The shortest path length L is defined as the minimum number of edges which has to be passed through from v_i to v_j. The clustering coefficient C_v is a measure for the cliquishness of a neighborhood (Watts and Strogatz, 1998). For a vertex v with k_v neighbors the maximal possible number of edges between its neighbors is given by $k_v(k_v\text{-}1)/2$. When l_v denotes the actual number of edges l_v between the neighbors of v, then the clustering coefficient C_v is defined as (Watts and Strogatz, 1998):

$$C_v = \frac{2l_v}{k_v(k_v - 1)} \tag{3.3}$$

Here, average clustering coefficients $\bar{C}$ of entire graphs are compared. Both L and C were calculated from A using available MATLAB routines (Kleder, 2005; Gleich, 2009). The small-worldness S draws a link between the small-world parameters (C_{small} and L_{small}) and corresponding values for random networks with the same number of vertices and edges (see section 5.2.3). It is given by (Humphries et al., 2008):

$$S = \frac{C_{\text{small}}/C_{\text{rand}}}{L_{\text{small}}/L_{\text{rand}}} \tag{3.4}$$

Finally, the edge length d is analyzed as the path length does not correspond to a physical length. It corresponds to the Euclidean distance between a pair of vertices v_i and v_j.

4. Oriented Confined Water Induced by Cationic Lipids

Water bound at biological surfaces often denoted as "biological water" has very different properties in comparison to the bulk liquid, for example a higher density or less mobility. The interactions of water and biomolecules such as proteins or lipid membranes have been often examined by infrared spectroscopy (Barth, 2007; Binder, 2007). In particular, polarized attenuated total reflection (ATR) Fourier transform (FT) infrared (IR) spectroscopy allows the study of molecular orientation and ordering (Goormaghtigh et al., 1999).

In this chapter the results of a detailed ATR FTIR spectroscopy study of the lipid-associated water structure as a function of counterion will be presented. The quaternary dioctadecyldimethylammonium halides DODAX (X = F, Cl, Br, I), which belong to the cationic lipids, constitute the membrane matrix for the adhered water. Of interest, only DODAB could be purchased with an appropriate purity. Thus, the other three lipids had to be prepared as described in appendix B.1. Analytical characterization was performed by means of energy dispersive x-ray (EDX) spectroscopy, matrix-assisted laser desorption/ionization time-of-flight (MALDI-TOF) mass spectrometry and nuclear magnetic resonance (NMR) spectroscopy. The data are given in appendices B.2 - B.4.

Knowledge about temperature and water adsorption behavior is a prerequisite for a structural study of membrane-bound water. Therefore, in the first section the phase behavior of the cationic DODAX lipids is briefly characterized. The second section is dedicated to the lipid's water capacity. Both the phase behavior and the water capacity show a strong dependence on the counterion present. The four counterions form part of the Hofmeister series which originally ranked the ions according to their ability to modify the hydrogen (H) bonding network of bulk water (Hofmeister, 1888). Current research aims at unraveling direct interactions between ions and water molecules of the first hydration shell of macromolecules (Zhang and Cremer, 2006). However, the Hofmeister series is not further discussed within the present work.

In the third section the OH/OD stretching absorptions of water at DODAX membranes

were analyzed at low hydration of approximately one water molecule per lipid. The orientation of water molecules was determined for both H_2O and D_2O by evaluating IR order parameters and tilt angles of transition dipole moments with regard to the normal of the ATR crystal (cf. section 2.1.4). Deconvolved subbands were attributed to differently H bonded water populations. Band assignment was conducted by relating peak wavenumbers to stretching bands observed for pure water and small halide-water clusters as discussed in the last section. Furthermore, the picture will be completed by a glimpse on the results obtained by molecular dynamics (MD) simulations of the DODAB-water system. The simulations were set up and performed by Dr. C. Selle and, therefore, will not be discussed in full detail.

The results of this study are published which will lead to some coincidences between the current chapter and (Woiterski et al., 2012). In the following this will not always be cited explicitly.

4.1. The phase state of DODAX membranes

DODAX multistacks were prepared by depositing the lipids dissolved in $CHCl_3$ on a clean ATR crystal as described in section 3.2. ATR spectra were recorded under reproducible experimental conditions as summarized in table 3.1. Typical IR absorptions assigned to the alkyl chains of the four DODA halides are listed in table 4.1 and agree well with previous data (Wu et al., 2009; Myrzakozha et al., 1999; Schulz et al., 1998; Laughlin et al., 1990; Kawai et al., 1986; Umemura et al., 1984). The use of specific known IR spectroscopic features permits a phase identification of DODA halide films.

Assignment	Wavenumber / cm^{-1}	Symbol
Methyl symmetric stretching	2870 - 2872	$\nu_s(CH_3)$
Methyl antisymmetric stretching	2954 - 2957	$\nu_{as}(CH_3)$
Methylene symmetric stretching	2849 - 2850	$\nu_s(CH_2)$
Methylene antisymmetric stretching	2915 - 2917	$\nu_{as}(CH_2)$
Methylene scissoring	1470	$\delta_{sciss}(CH_2)$
Methylene rocking	717 - 721	$\gamma_{rock}(CH_2)$
Ammonium symmetric stretching	880 - 930	$\nu_s(CNC))$

Table 4.1.: Assignment of typical IR modes of the DODAX alkyl groups.

In order to determine chain melting transition temperatures, T_m, the cationic lipid films were hydrated at 50 % RH (relative humidity) and gradually heated starting from 25 °C. Figure 4.1 shows absorption spectra of DODAB recorded below (black) and above (red)

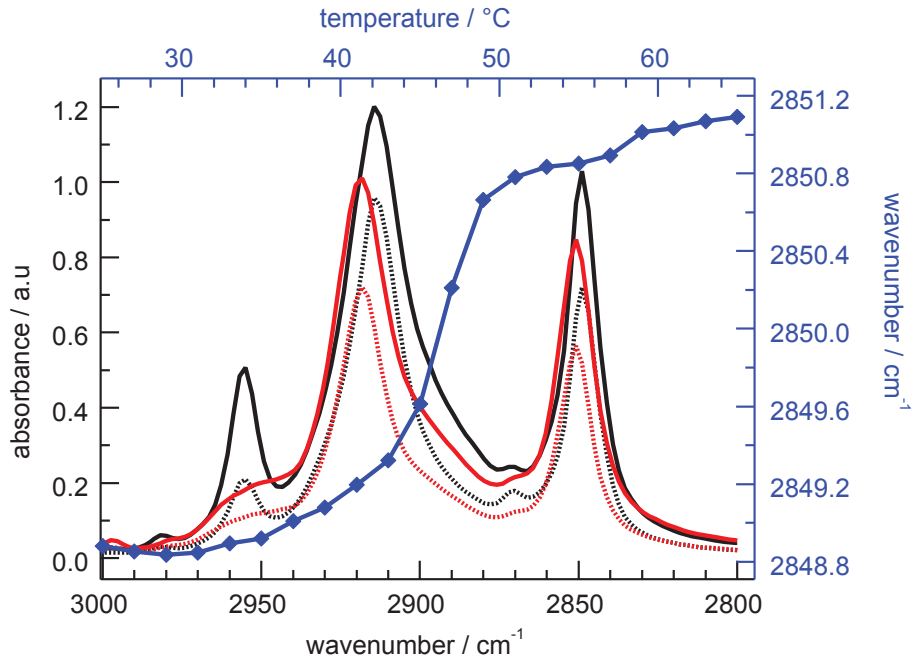

Figure 4.1.: Characteristic IR spectra for the main transition of an oriented DODAB film. *Blue*: the methylene symmetric stretching band maximum depicted during heating (steps of 2 °C). The blue solid line is to guide the eye. The main transition occurs at the steepest increase at (47 ± 1) °C for DODAB. *Solid black and red lines*: Spectra of the CH stretching IR absorption bands below and above, respectively, the main transition at p-polarization. *Dotted lines*: corresponding spectra at s-polarization. Image as published in (Woiterski et al., 2012).

T_m with p- and s-polarized IR light (solid and dotted line), respectively. Furthermore, it displays the temperature dependence of the $\nu_s(CH_2)$ peak wavenumber resulting from DODAB's alkyl chains. Its steep frequency displacement of approximately 2 cm^{-1}, which was also observed for the other DODA halides (cf. table 4.2), is in agreement with other lipids undergoing the main transition (Lewis and McElhaney, 2007; Casal and Mantsch, 1984). T_m was determined at the point of maximal slope (at the band maximum) and found to be 65 ± 1 °C for DODAF, 50 ± 1 °C for DODAC and 47 ± 1 °C for DODAB, which is for DODAC slightly higher and for DODAB in good accordance with previous results (Laughlin et al., 1990; Feitosa et al., 2000; Cocquyt et al., 2005).

For DODAB and DODAC the observed wavenumber increase at the main transition occurs within a broader temperature range than reported for fully hydrated lipid membranes of DPPC and DODAC (Umemura et al., 1984; Fringeli and Günthard, 1981). This can be attributed to the loss of the small amount of water during heating as exemplarily shown for DODAB in figure 4.2. Water desorption was monitored by the decrease of the OH stretching absorption intensity. Reduced hydration commonly leads to a tighter chain packing in lipid membranes invoking a higher chain order. Thus, the result of dehydration is a higher transition temperature (Seddon and Cevc, 1993).

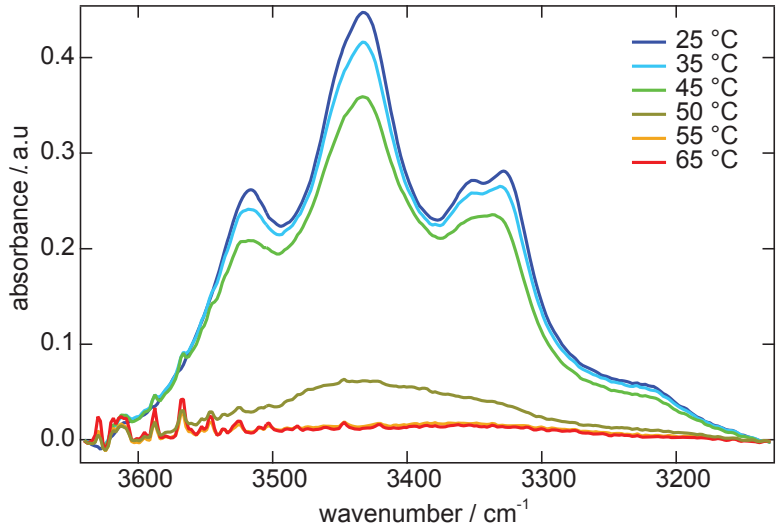

Figure 4.2.: Water desorption from DODAB multistacks during heating. The decreasing band intensity of the OH stretching absorption (non-polarized ATR spectra) illustrates the loss of interbilayer water due to heating from 25 °C to 65 °C.

In contrast to the other three DODA halides, DODAI demonstrated a continuous and relatively small wavenumber increase for the $\nu_s(CH_2)$ band during heating suggesting that DODAI has less ordered alkyl chains at all temperatures. The low water capacity of DODAI impeded the study of associated water making a detailed characterization of the phase behavior unnecessary.

Further temperature-induced discontinuous changes were observed for intensity, bandwidth and peak frequencies of other methylene and methyl group IR absorption bands in accordance with previous studies (Lewis and McElhaney, 2007; Mantsch and McElhaney, 1991; Fringeli and Günthard, 1981). Hydrated samples of the fluoride, chloride and bromide analogs at 25 °C exhibited a $\delta_{sciss}(CH_2)$ peak frequency of 1470 cm^{-1}, indicating a gel phase. The presence of a previously reported coagel phase (Wu et al., 2009) can be excluded here because the $\delta_{sciss}(CH_2)$-coagel phase absorption band maximum for DODAB and DODAC was observed between 1471.2 cm^{-1} and 1473 cm^{-1} (Wu et al., 2009; Kawai et al., 1986; Umemura et al., 1984). Furthermore, the band shape of the OH stretching absorption (cf. section 4.3) as well as the wavenumber of the water deformation mode ν_2(HOH) (data not shown) for DODAC agree with previous results for the DODAC gel phase (Umemura et al., 1984).

Chain order parameters S_θ and tilt angles θ_μ of the alkyl chains with regard to the normal of the ATR crystal were determined from the dichroic ratio R using equations 2.1 to 2.3. Together with the peak wavenumber of the $\nu_s(CH_2)$ absorption they are given in table 4.2. The states A and C refer to the experimental conditions given in table 3.1. Briefly, in *state A* DODAX lipids were heated above the transition temperature and interbilayer

Lipid	State A: $\nu_s(CH_2)$ / S_θ / θ_μ	State C: $\nu_s(CH_2)$ / S_θ / θ_μ
DODAF	$2852.25\,cm^{-1}$ / 0.34 / 41.7°	$2850.27\,cm^{-1}$ / 0.39 / 39.7°
DODAC	$2851.79\,cm^{-1}$ / 0.25 / 45.0°	$2850.47\,cm^{-1}$ / 0.22 / 46.3°
DODAB	$2850.93\,cm^{-1}$ / 0.35 / 41.2°	$2850.13\,cm^{-1}$ / 0.37 / 40.4°
DODAI	$2852.30\,cm^{-1}$ / 0.29 / 43.4°	$2850.80\,cm^{-1}$ / 0.34 / 41.9°

Table 4.2.: Characteristic parameters of dry DODAX films above the transition temperature (65 - 80 °C, state A) as well as after cooling and rehydration (25 °C, 80 % RH for DODAC/DODAB and 3 % RH for DODAF, state C). SE less than: $\pm 0.5\,cm^{-1}$ ($\nu_s(CH_2)$), ± 0.10 (S_θ), $\pm 12°$ (θ_μ).

water was completely desorbed from the multistacks. This is reflected by the shifted $\nu_s(CH_2)$ wavenumbers to higher values and slightly lower values of S_θ compared to state C. Lipids in *state C* were used for the analysis of water structure (see section 4.3). For this purpose, the films were transferred again to the gel phase by cooling down to 25 °C followed by the rehydration at 80 % RH (DODAC and DODAB) and 3 % RH (DODAF), respectively, to obtain a similar hydration of one water molecule per lipid. An equal water per lipid ratio is important for a proper comparison as described in the next sections. The measured chain tilt angle at 25 °C for DODAB agrees well with earlier data (Okuyama et al., 1988; Ionov and Angelova, 1996).

The decrease of the IR or chain order parameter S_{IR} (S_θ) at the main transition is caused by alternated average methylene group orientations with regard to the ATR crystal (Fringeli and Günthard, 1981). For various phospholipids, a substantial reduction of S_θ by approximately 0.2 was observed (Binder, 2003), which is in clear contrast to the finding for DODAX. A possible explanation for those nearly constant chain order parameters of lipids undergoing the main transition is that on one side the thermally induced disorder of the average methylene group orientation increases. On the other side, for DODAX there is a counteracting increase in order associated with the changed tilt angle of the entire chain caused by the vanishing of the octadecyl chain's kink. A recent small-angle x-ray scattering study supports this interpretation (Saveyn et al., 2009). The authors determined a bilayer thickness difference of 0.1 nm for DODAB between the liquid phase (bilayer thickness $d = 3.32$ nm) and the gel phase ($d = 3.42$ nm), which is small compared to the corresponding difference of 1.3 nm reported for DPPC (Janiak et al., 1976). Thus, the moderate change in the DODAB bilayer thickness could be the cause of the small change in the average orientation of the methylene groups.

Beside the IR spectroscopic signatures of the alkyl chains, phospholipid polar headgroup absorptions were reported to change during chain melting and/or at varied hydration (Binder, 2003; Okamura et al., 1990; Pohle et al., 1998). The small polar headgroup of DODAX has few vibrational groups that are sensitive to interactions with adsorbed

water. Absorptions between 880 cm^{-1} and 930 cm^{-1} were assigned to the symmetric CNC stretching vibrations due to the quaternary ammonium ion and strongly depend on hydration (Binder, 2003; Pohle and Selle, 1996; Gradolnik et al., 1991). As shown exemplarily for DODAB in figure 4.3, the ν_s(CNC) stretching bands of hydrated DODAX (X = F, Cl, Br) gel phase samples (0 and C) exhibited two peaks at 910 cm^{-1} and 920 cm^{-1} which were not observed for dehydrated samples at the same temperature (B). At the cost of those two bands, the integral intensity of the band at 889 cm^{-1} increased when the samples were dehydrated above as well as below T_m (A and B). Pronounced changes in headgroup absorptions of DODAF, DODAC and DODAB point to a direct interaction of the lipid headgroup with interbilayer water. In contrast, DODAI headgroup absorptions did not exhibit any change. Although IR absorptions of the DODA headgroup were shown to be sensitive to adjacent water molecules, an effect of the large monovalent quaternary ammonium cation on the water stretching band can be expected to be significantly weaker than that of the present anions (Bergström and Lindgren, 1992), as described in the following section 4.2.

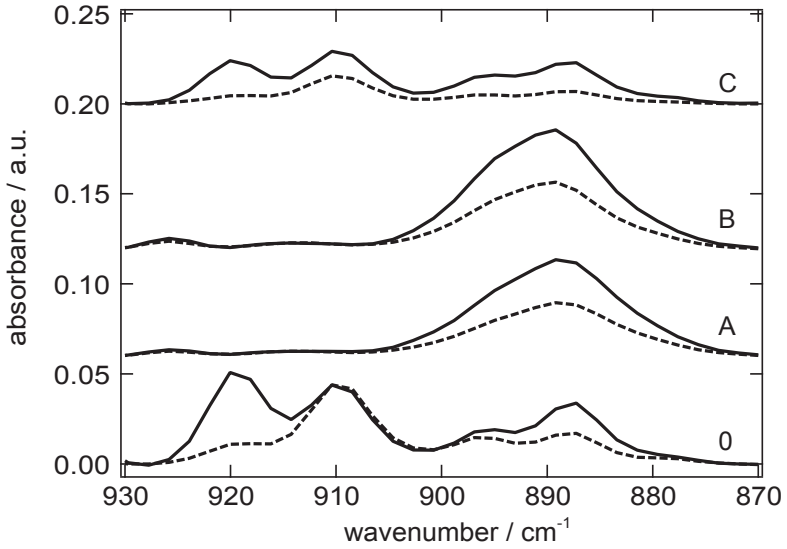

Figure 4.3.: IR spectra in the range of the ν_s(CNC) vibration of DODAB representative for DODAX (X = F, Br, Cl). ATR spectra of a DODAB sample were recorded with p-polarization (solid lines) and s-polarization (dashed lines), respectively, at *O*: 25 °C, hydrated at 50 % RH; *A*: 65 °C (above the phase transition), dehydrated; *B*: at 25 °C, dehydrated; *C*: at 25 °C, 80 % RH, rehydrated. For clarity, the base lines of spectra A - C were shifted by 0.06, 0.12 and 0.2 absorbance units, respectively. DODAI head group absorptions did not exhibit any change.

4.2. Water capacity of DODAX membranes

The ability of DODAX to adsorb water was studied at a hydration of 80 % RH and 25 °C. Figure 4.4 shows spectra of the OD stretching absorption of D_2O associated to DODAX

samples and the phospholipid 1,2-dimyristoyl-*sn*-glycero-3-phosphocholine (DMPC). Pronounced differences of ν(OD) absorption intensities, band structures and bandwidths were observed. H_2O stretching bands from samples hydrated by pure H_2O demonstrated analog properties. However, H_2O absorptions of DODAF samples overlap with CH_2 and CH_3 stretching bands due to alkyl residues and are, therefore, not shown.

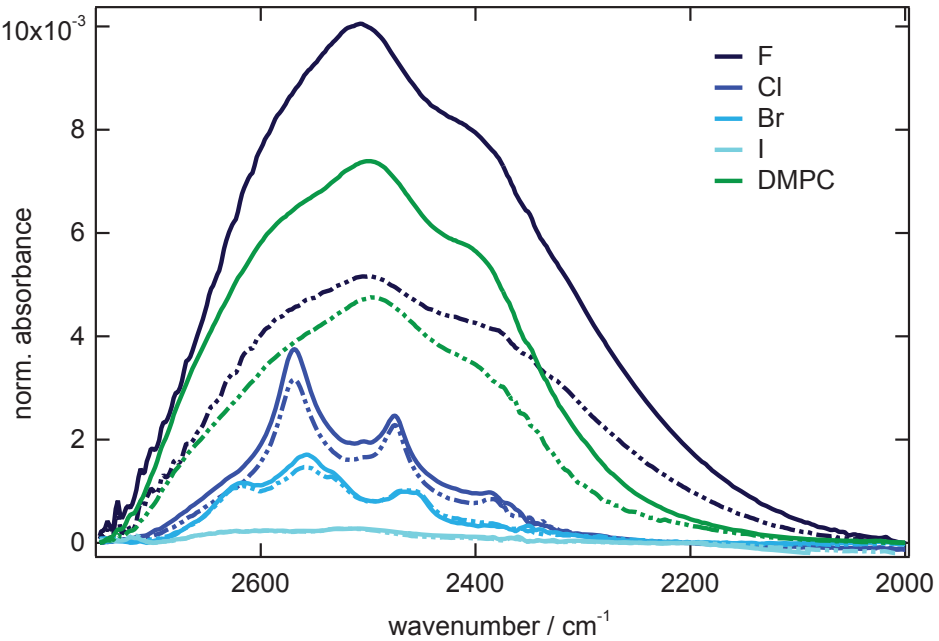

Figure 4.4.: ATR spectra of ν(OD) absorptions from D_2O bound to oriented DODAX multilayers (X = F, Cl, Br, I) and DMPC at 25 °C and 80 % RH recorded with p-polarization (solid lines) and s-polarization (dotted), respectively. All spectra were normalized to the lipids' CH stretching intensities to compare for the water content of the different lipids.

The intensities of the broad OH stretching band at 3400 cm^{-1} and the CH stretching bands at 3000 cm^{-1} due to the lipid alkyl chains can be used to quantify the amount of membrane adsorbed water (Gauger et al., 2001; Kint et al., 1992). Therefore, the ratio of the integrated absorbances of ν(OH) and ν(CH) absorptions is approximated by a linear function for the membrane adsorbed water concentration (Gauger et al., 2001). Due to the comparably low hydration of DODAX samples, the effect of membrane swelling is considered small and was ignored in the estimations of the water content. Using this ratio in combination with earlier published data on the hydration of phospholipids by Karl-Fischer titration (Gauger et al., 2001) provided an average hydration of 11.0 ± 2.6 water molecules/lipid for DODAF, 1.2 ± 0.2 for DODAC and 0.8 ± 0.2 for DODAB. DODAI samples at 25 °C and 80 % RH did not adsorb significant amounts of water and were, thus, not included in the further analysis. The water capacity monotonically decreases as a function of increasing halide radius. This water adsorption behavior is solely attributed to the nature of the anions present within the lipid samples. It correlates with the halide

anions' hydration free energies, which rise from fluoride to iodide, with the smallest hydration free energy gain found for the iodide ion (Lamoureux and Roux, 2006). Of interest, it was impossible to completely remove water from DODAF samples under the experimental conditions – a fact which indicates that hydrated DODAF is energetically strongly preferred.

The band structures of water at DODAX also revealed strong alterations dependent on the anion. DODAF-bound water displays a strong ν(OD) band centered at 2501 cm^{-1} and a shoulder at 2395 cm^{-1}, attributed to the second and to higher hydration shells (see figure 4.4). However, it does not show substantial differences compared to spectra at low hydration (2 water/lipid, cf. figure 4.5). In contrast, the corresponding band of water bound to DODAC (DODAB) exhibits three visible distinct peaks at 2569 cm^{-1} (2617 cm^{-1}), 2475 cm^{-1} (2560 cm^{-1}) and 2385 cm^{-1} (2463 cm^{-1}) and a shoulder at 2370 cm^{-1} (DODAB only). These results agree with earlier published IR spectra of the low-hydrated DODAC-water system (Laughlin et al., 1990; Kawai et al., 1986) and previous measurements of DODAB-associated water, where a clearly split ν(OH) band was found (Britt et al., 2003). The striking substructures visible in the OD/OH stretching bands of water at DODAC and DODAB were never observed for phospholipid samples (e.g. DMPC in figure 4.4), even at very low hydration (Tielrooij et al., 2009; Binder, 2003). DODAB vesicles dispersed in excess water displayed a slightly structured ν(OH) band typical for the solvent (Schulz et al., 1998). The narrow bandwidths of the subbands suggest underlying water populations which are confined and differ in their H bonding and mobility (Sammon et al., 1998).

Concerning the bandwidth, as exemplified in figure 4.4, the largest width of the OD stretching band was observed for water within DODAF membranes (2000 cm^{-1} to 2700 cm^{-1}). The IR spectrum resembles the one of pure bulk water (Venyaminov and Prendergast, 1997). However, the ν(OH) bandwidths found for DODAC- and DODAB-associated water (2200 cm^{-1} to 2700 cm^{-1}) are significantly smaller. The fraction of absorption intensity at lower wavenumbers is concomitantly less prominent. This difference is clearly dependent on the anions interacting with water.

Summarizing it can be noted that these three features indicate special properties of water adsorbed to DODA cationic lipids regarding H bonding and mobility. A detailed analysis of the dichroic measurements of the structured ν(OH) and ν(OD) bands is presented in the next section. The peculiar properties of water adsorbed at DODAX membranes may help to better interpret the features of membrane-associated water's IR absorption bands.

4.3. Stretching bands of water adsorbed to DODAX

4.3.1. General remarks on samples and band assignment

To compare counterion effects, spectra of DODAX samples with a constant hydration of ~ 1 water/lipid were analyzed. These were measured at a temperature of 25 °C and a sample dependent humidity (DODAF 3 % RH, DODAC and DODAB 80 % RH).

But before evaluating the individual DODAX water spectra, some general aspects on the analysis of water stretching bands are given. Phospholipid water IR stretching bands at varied water concentrations have been frequently reported to exhibit similar band maxima at about 3400 cm^{-1} and shapes as found for bulk liquid water (Tielrooij et al., 2009; Volkov et al., 2009; Zhao et al., 2008; Binder, 2003; Pohle et al., 1998). H bonded water within the bulk liquid was suggested to give rise to collective stretching normal modes comprised of linear combinations of symmetric and antisymmetric stretching vibrations (Lappi et al., 2004). The observed stretching bands were deconvolved using up to five Gaussian subbands attributed to differently coordinated water and H bonded vibrational groups (Brubach et al., 2005).

Initial fit parameters like peak positions, widths and intensities of OH stretching bands were used according to a work by Liu and colleagues (Liu et al., 2004). They measured ATR FTIR spectra of neat water and aqueous sodium halide solutions and assigned ν(OH) subbands at 3249, 3420 and 3591 cm^{-1} to an intermolecularly coupled symmetric stretching vibration within a symmetric HB (hydrogen bond) network, to a weaker coupled asymmetric HB network and to coupled antisymmetric ν(OH) modes, respectively (Liu et al., 2004). An additional Gaussian subband was added for the OD spectra of water at DODAF and three more peaks for OH/OD spectra of DODAC and DODAB, which were clearly recognizable due to their distinct and narrow shape.

ATR spectra of the ν(OH) and ν(OD) regions recorded for DODAX samples (X = F, Cl, Br) together with their fitted Gaussian subbands are shown in figure 4.5 for the p- (black solid lines) and s-polarization (dotted), respectively. Differences between the D_2O and H_2O stretching absorptions reflecting the dissimilar properties due to isotopic substitution will be discussed for individual DODAX results. They have been a widely investigated phenomenon and are still not completely understood (Bakker and Skinner, 2010; Paesani and Voth, 2009; Brubach et al., 2005; Venyaminov and Prendergast, 1997). All band fitting results including order parameters derived from polarized measurements are given in table 4.3. Details of these results are reported in the order of increasing DODAX halide mass, i.e., starting with DODAF, followed by DODAC and DODAB.

The measurements of DODAF samples with a minimal water content of about 2 water

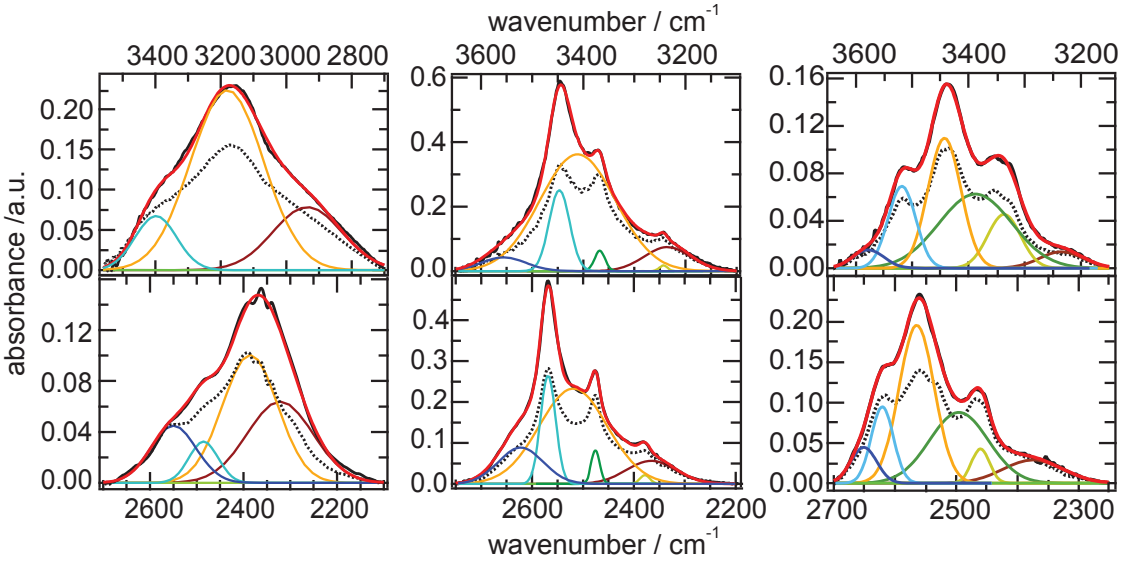

Figure 4.5.: Band-fitting results for OH (top) and OD (bottom) stretching bands of water bound to DODAF (at 25 °C, 3 % RH), DODAC and DODAB (both at 25 °C, 80 % RH) from left to right. ATR spectra were recorded with p-polarized (black solid) and s-polarized (dotted) light, respectively. Deconvolved Gaussian subbands were depicted for spectra measured with p-polarized light together with their sums drawn by solid red lines. Image as published in (Woiterski et al., 2012).

		DODAF				DODAC				DODAB			
		ν_{max}/ cm^{-1}	$\Delta\nu_{1/2}$/ cm^{-1}	S_{IR}	θ/°	ν_{max}/ cm^{-1}	$\Delta\nu_{1/2}$/ cm^{-1}	S_{IR}	θ/°	ν_{max}/ cm^{-1}	$\Delta\nu_{1/2}$ cm^{-1}	S_{IR}	θ/°
H_2O	1	2928	248	-0.13	60.2	3238	117	-0.17	62.0	3237	105	-0.19	63.0
	2	3188	278	-0.05	56.8	3244	25	-0.44	78.5	3338	66	-0.11	59.3
	3	3409	174	-0.14	60.7	3368	29	-0.47	81.9	3394	155	-0.17	62.0
	4					3411	162	-0.05	56.8	3444	65	-0.06	57.2
	5					3446	41	0.22	46.1	3519	60	-0.14	60.7
	6					3549	137	0.22	46.1	3580	67	-0.16	61.6
D_2O	1	2307	198	0.16	48.4	2368	123	-0.15	61.1	2379	104	-0.22	64.4
	2	2385	153	-0.21	63.9	2380	26	-0.15	61.1	2461	37	-0.26	66.4
	3	2484	40	0.69	27.0	2475	23	-0.42	76.6	2489	108	-0.19	63.0
	4	2546	129	-0.24	65.4	2524	168	-0.09	58.5	2561	73	-0.13	60.2
	5					2569	34	0.01	54.3	2623	42	-0.11	59.3
	6					2622	87	0.13	49.6	2657	42	-0.21	63.9

Table 4.3.: Band-fitting results of ν(OH) and ν(OD) absorptions of DODAX-bound water.

molecules/lipid were used for band fitting and analysis. Further removal of water by heating was avoided because water stretching band structure was shown to be affected by temperature changes (Riemenschneider et al., 2009; Brubach et al., 2005).

4.3.2. Band analysis and orientation measurements for DODAF

DODAF's water stretching band (figure 4.5) is less resolved into subbands than those of DODAC and DODAB and apparently more similar to bulk water absorption. This similarity justifies the comparison with bulk water stretching bands reported previously. The low ν(OH) and ν(OD) band maxima at approximately 3190 and 2330 cm^{-1} indicate stronger H bonding than in bulk water at 25 °C with a band maximum at $\sim$3400 cm^{-1} (Liu et al., 2004). The broad ν(OH) and ν(OD) bands extending to frequencies as low as 2800 cm^{-1} and 2100 cm^{-1}, respectively, observed in this study were sometimes reported to show features similar to spectra of solid ice (Riemenschneider et al., 2009; Buch and Devlin, 1999) in the past. However, Bonn and coworkers recently carried out IR measurements on isotopic H/D solutions and explicitly state that water at biological membranes is not ice-like, but influenced by intramolecular coupling (Bonn et al., 2012).

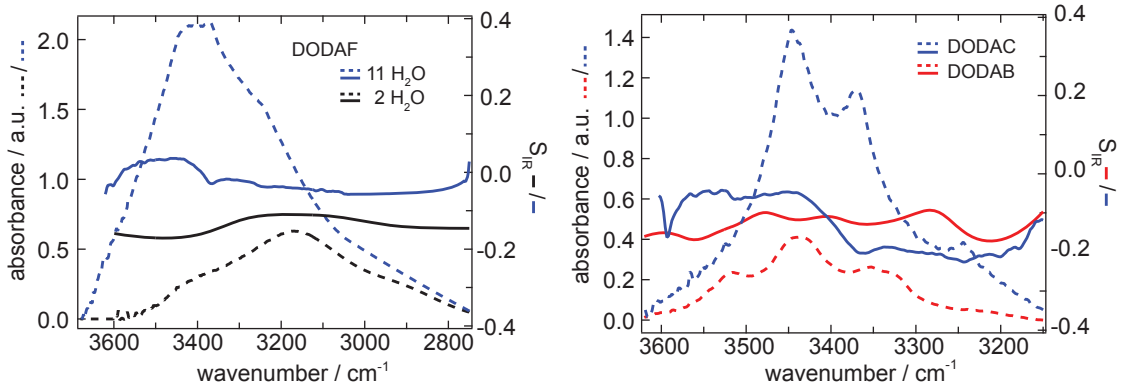

Figure 4.6.: S_{IR} of DODAX (solid lines) as function of the wavenumber. Corresponding unpolarized OH stretching spectra are given additionally as dashed lines. *Left:* Low- (black) and well-hydrated (blue) DODAF at 2 and 11 water/lipid, respectively. *Right:* DODAC (blue) and DODAB (red) at $\sim$ 1 water/lipid. The negative values of S_{IR} for low-hydrated DODAF, DODAC and DODAB reveal strongly oriented water molecules within the lipid membranes.

From polarized ATR FTIR measurements of low-hydrated DODAF (2 water/lipid), the dependence of the order parameter S_{IR} on the frequency was analyzed (figure 4.6, left). It was nearly constant at approximately -0.13 with slight fluctuations over almost the entire range of the OH stretching absorption. In contrast, for well-hydrated DODAF (11 water/lipid), anisotropically oriented water within the bilayers was not found as the corresponding S_{IR} function within that spectral range was zero. The value of S_{IR} = -0.12 indicates an average orientation of transition dipoles for OH and OD stretching modes of about 60° with respect to the bilayer plane's normal.

Fitting of the bands was carried out for low-hydrated DODAF samples and resulted in three and four subbands for H_2O and D_2O, respectively (see table 4.3). The low frequency wing of the ν(OH) band (3050 - 2800 cm^{-1}) overlaps with methylene/methyl stretching bands. Thus, analysis of the ν(OH) band required prior subtraction of the alkyl absorp-

tions leading to a higher error in the resulting ν(OH) band and in fitted subbands within this spectral range. Apparent differences of the D_2O and H_2O IR stretching bands can arise from this correction. The strongest peaks (no. 2) occur at 3188 (H_2O) and 2385 cm^{-1} (D_2O) with corresponding orientation angles of 56.8° and 63.9° with regard to the bilayer normal, respectively. The peaks at 3409 (H_2O, no. 3) and 2546 cm^{-1} (D_2O, no. 4) with average orientation angles of 60.7° and 65.4° approximately agree in their order parameters, suggesting analog vibrational groups for these components. Observations for DODAC and DODAB samples support this interpretation (see below). A relatively high error can be expected for S_θ and θ_μ of peak no. 3 (D_2O) due to its poor absorbance signal-to-noise ratio. Occurrence of the additional weak peak no. 3 can be connected to specific properties of D_2O (Riemenschneider et al., 2009).

4.3.3. Band analysis and orientation measurements for DODAC

DODAC bilayer stacks on an ATR crystal adsorbed ~1 - 2 water/lipid at the experimental conditions. Water spectra were fitted with six Gaussian components (cf. figure 4.5, table 4.3). Subbands were assorted into two different peak systems: peak system I comprises the three broader components (no. 1, 4 and 6). The three remaining narrower components (no. 2, 3 and 5) are denoted in the following as peak system II. Due to the high similarity of the H_2O and D_2O stretching spectra, analog peak systems I and II were found for the observed ν(OD) bands.

Within the entire water stretching regions of D_2O and H_2O, the S_{IR} dependency on the wavenumber fluctuated between -0.1 and -0.2 (see figure 4.6, right). This indicates an anisotropic orientational order of water adsorbed to DODAC as found for low-hydrated DODAF. However, S_{IR} values obtained for individual Gaussian band components deviate strongly from this value and will be discussed below.

The ν(OH) component wavenumbers of peak system I deviate only slightly from values reported for NaCl solutions (Liu et al., 2004). The three peaks represent 72 - 87 % of the integral absorbance of the entire ν(OH) or ν(OD) stretching bands. This can reflect a major water fraction within DODAC bilayers which retains similar properties or interactions as water within aqueous chloride solutions. The broad central peaks (no. 4) at 3411 and 2524 cm^{-1} contribute 60 - 75 % to the entire stretching bands and strongly correlate with each other as reflected by similar order parameters and average orientation angles. The smaller ν(OH) and ν(OD) components (no. 1 and 6) contribute 15 - 20 % to the entire stretching absorption intensity. The ν(OH) and ν(OD) orientation angles agree well with each other, but show a large difference between components no. 1 and 6. This supports a strong correlation to the fundamental symmetric (no. 6) and antisymmetric stretching

(no. 1) vibrations of water (Liu et al., 2004).

The narrow ν(OH) and ν(OD) components of peak system II match in their widths, intensities and order parameters. Therefore, only the results for ν(OH) are discussed. Small widths indicate a narrow distribution of H bonding of involved vibrational groups. Peak no. 5 with highest integral intensity (8.6 %) at 3446 cm^{-1} can be assigned to less H bonded water molecules due to its comparatively higher peak frequency, which is supported by its high value of S_{IR}. In contrast, the other two peaks (no. 2 and 3) exhibit very low order parameters of -0.44 and -0.47. Furthermore, the large order parameter differences between peak no. 5 and peaks nos. 2 and 3 are accompanied by a drastic change in orientation of the related vibrational transition moments. Thus, components nos. 2 and 3 can be linked to oscillators belonging to a uniformly oriented but differently H bonded water fraction, varying in accepted HBs.

4.3.4. Band analysis and orientation measurements for DODAB

DODAB associated water (water/lipid ratio $\sim$1) exhibits very similar IR spectroscopic properties as water within DODAC membranes (cf. figure 4.5). As for DODAC, peaks and additional visible shoulders were summarized in peak systems I and II including the broader (nos. 1, 3, 6) and narrower subbands (nos. 2, 4, 5), respectively.

For the entire water stretching region, the wavenumber dependence of S_{IR} slightly fluctuated between -0.1 and -0.2 which indicates anisotropic orientation of dipole moments (see figure 4.6). In contrast to DODAC, the S_{IR} values for the DODAB subbands agreed with the generally measured S_{IR} value.

The ν(OH) spectra agree mostly with ν(OD) spectra regarding the widths, intensities and order parameters (cf. table 4.3). Peak system I peaks contributes $\sim$39 - 53 % to the entire integral stretching absorption.

The order parameters of the band components and average orientations of the water molecules within DODAB appear more homogeneous than found for DODAC. A possible explanation for this behavior is that water molecules embedded within DODAC samples could be sterically less confined than in DODAB giving rise to more variation in orientation compared with bromide ions which require more room than chlorides. The higher water capacity of DODAC supports this assumption.

4.4. Discussion

4.4.1. Comparison of water stretching bands from aqueous salt solutions, ion-water clusters and DODAX membranes

DODAF

DODAF ν(OH) component no. 3 resembles the peak at 3412 cm^{-1} recorded for aqueous sodium fluoride (NaF) solutions (fluoride molar fraction $x = 0.015 \approx 0.83$ M) regarding its frequency and bandwidth (Liu et al., 2004). As the latter showed little deviations from neat water, weakly modified H bonding can also be assumed for water at DODAF (Liu et al., 2004). Furthermore, salt solutions with isotopically diluted water exhibited ν(OD) absorptions similar to D_2O adhered to DODAF multilayers. IR spectra of NaF solutions (0.642 M in 8 % D_2O/H_2O) showed a fluoride hydration band at 2472 cm^{-1} which was interpreted as marker of an anion-bonded isolated OD stretching oscillator within HOD molecules (Bergström et al., 1991). In another study, concentrated NaF solutions (molar fraction $x = 0.25$) in 4 % D_2O/H_2O mixtures yielded an OD stretching band at about 2460 cm^{-1} with a larger bandwidth than observed for neat water (Nickolov and Miller, 2005). Thus, the findings for the DODAF water stretching bands indicate the presence of a significant fraction (16 - 22 % of adsorbed water) of similar vibrational groups as reported for bulk aqueous fluoride solutions.

Due to the high proportion of water in DODAF exhibiting vibrations similar to that of bulk fluoride solutions, few water molecules should exist confined at the polar surfaces between DODAF bilayers. Therefore, the formation of cluster-like fluoride-water structures at the membrane's polar regions can be expected. A comparison with IR spectroscopic data especially of stretching band frequencies reported for fluoride-water clusters allows an interpretation of the measured ν(OH) spectra. Water-fluoride (1:1) complexes exhibit very low water stretching band frequencies (Roscioli et al., 2006). $(H_2O)_2 \cdot F^-$ and $(H_2O)_3 \cdot F^-$ clusters gave rise to stretching absorptions at 2490 and 2890 cm^{-1}, respectively, which were assigned to IHBs (ionic hydrogen bonds) (Cabarcos et al., 1999; Robertson and Johnson, 2003). $F^- \cdot (H_2O)_4$ and $F^- \cdot (H_2O)_5$ clusters exhibited IHB stretching bands at 3072, 3143 and 3389 cm^{-1}, respectively, and little or no indications for H bonding between water molecules were found (Cabarcos et al., 1999).

Fluoride clusters with 3 - 5 water molecules have strongest vibrational absorptions in the range of 2890 and 3143 cm^{-1}. IR absorptions of DODAF water in this region (H_2O, peaks no. 1 and 2) which comprise 77 - 84 % of adsorbed water may belong to a major fraction of similar structure within DODAF bilayers.

DODAC

The strongest peak of H_2O (no. 4) is similar to a ν(OH) component at 3396 cm^{-1} reported for bulk water which was assigned to a stretching absorption of a weaker coupled asymmetric HB network (Liu et al., 2004). The corresponding ν(OD) component agrees well with a sodium chloride (NaCl) hydration band (0.442 M NaCl in 8 % D_2O/H_2O) and an uncoupled ν(OD) stretching band (4 % D_2O/H_2O at high chloride concentrations) which were both found at 2530 cm^{-1} (Nickolov and Miller, 2005; Bergström et al., 1991). This suggests that either a large fraction of water molecules in DODAC includes uncoupled OH or OD oscillators or that asymmetric H bonded water in these samples exhibits similar spectral features as decoupled OH or OD oscillators.

In analogy to DODAF, the measured spectra of water at DODAC are compared with spectra of water-chloride clusters because similar water-chloride interactions can be assumed. Absorption bands at 3408 and 3441 cm^{-1} reported for $Cl^-\cdot(H_2O)_4$ and $Cl^-\cdot(H_2O)_5$ clusters were assigned to IHB water stretching vibrations, respectively, and highly agree with the ν(OH) components no. 4 and 5. Related $Cl^-\cdot(H_2O)_3$ clusters showed three bands in the range from 3200 - 3400 cm^{-1}. An increasing number of associated water molecules was correlated with a blue shift (Choi et al., 1998). IR spectra of $Cl^-\cdot(H_2O)_2\cdot Ar_3$ clusters showed five bands. Their peaks at 3375 and 3130 cm^{-1} were assigned to a double-donor (DD) and acceptor-donor (AD) IHB OH stretching (Ayotte et al., 1999; Robertson and Johnson, 2003). The first peak may be related to the weak component (no. 3) of water within DODAC at 3368 cm^{-1}. The lower peak at 3244 cm^{-1} can be due to water in a bimolecular chloride cluster with another accepted HB, i.e., a DDA IHB OH stretch.

All correlations point to similarities of DODAC-associated water and anionic clusters of 2 - 5 water molecules. These findings agree well with previous IR spectroscopic features of H_2O bound to DODAC gel phases (Kawai et al., 1986; Umemura et al., 1984). However, ν(OD) absorptions presented here differ strongly from those results possibly due to the better signal-to-noise ratio in the present ATR FTIR measurements (Kawai et al., 1986).

DODAB

Peaks no. 1 and 6 of the ν(OH) band are shifted by 12 cm^{-1} to lower wavenumbers compared to corresponding peak positions obtained for spectra of bulk aqueous bromide solutions (Liu et al., 2004). The position of the strongest component (peak no. 3) agrees with the corresponding ν(OH) component of pure bulk water and is shifted by 30 cm^{-1} to lower frequencies compared to a band of sodium bromide (NaBr) solutions

(Liu et al., 2004). This is supported by the frequency of the analog ν(OD) component no. 3 (2489 cm^{-1}) which is close to the decoupled ν(OD) stretching absorption at 2505 cm^{-1} in bulk neat water (Bergström et al., 1991; Riemenschneider et al., 2009).

In peak system II, the wavenumber of the strongest component at 3444 cm^{-1} (no. 4) deviates by 24 cm^{-1} from the position of a related subband of aqueous NaBr solutions and its width is significantly smaller (65 vs. 257 cm^{-1}) (Liu et al., 2004). The corresponding ν(OD) peak position agrees well with that of a bromide hydration band observed for uncoupled OD oscillators (Bergström et al., 1991). However, the bandwidth observed for D_2O in DODAB is smaller (65 vs. 147 cm^{-1}) indicating less variation of the H bonded and/or dipolar environment.

The results for DODAB are also related to stretching bands of small water clusters. Bromide-water clusters with one to four water molecules give rise to IHB OH stretching bands at 3368, 3373, 3422 and 3466 cm^{-1} (Ayotte et al., 1998). Spectra of $Br^- \cdot H_2O$ and $Br^- \cdot (H_2O)_2Ar_3$ clusters exhibited IHB absorption peaks at 3270 and 3438 cm^{-1}, respectively. The latter absorption was assigned to an OH oscillator of a DD water molecule with HBs to bromide and to another water molecule (Roscioli et al., 2006; Ayotte et al., 1999). Such a cluster-like structure can occur within hydrated DODAB bilayers and may be reflected by peak no. 4. Otherwise, it can be also described as asymmetric unit including an OH stretching group H bonded to bromide (Liu et al., 2004). Component no. 3 can be due to a similar water fraction accepting a water molecule which leads to a red shift compared with component no. 4.

4.4.2. Correlations between water stretching bands from the varied DODAX species

Hydrated DODAX samples exhibited highly similar OH stretching component frequencies. DODAF peaks nos. 3 (H_2O) and 4 (D_2O) are related with DODAC peak no. 4 as well as with DODAB peak no. 3. All of these components are connected to absorptions of isolated water stretching oscillators (HOD in H_2O) in aqueous halide solutions. DODAF (no. 4) and DODAC (no. 3) peaks are also similar to stretching band components observed for bulk water (H_2O or D_2O) halide solutions. Furthermore, component no. 1 of spectra from DODAC and DODAB samples shows an agreement in band position and width. The spectroscopic findings suggest that an asymmetric H bonded water population found in DODAF and DODAC is split in DODAB bilayers into two fractions which strongly and weakly interact with bromide anions, respectively. Further similarities are found for ν(OH) components nos. 5 (DODAC) and 4 (DODAB). However, they are not as apparent for components nos. 2 and 3 (DODAC) and nos. 1 and 2 (DODAB) which differ

in their order parameter.

The common features in spectra point to water fractions in similar polar/H bonded environments. The fraction of bulk-related water (reflected by the broad bands similar to those found for aqueous salt solutions) can be larger in DODAC than in DODAB because of the high integral absorbance of components nos. 1, 4 and 6. A possible reason is the higher water content of investigated DODAC samples leading to less interaction of water with the ammonium salt components. It should be further noted that bandwidths of peak system II of DODAC water are noticeably smaller than those of analog DODAB values. This indicates the existence of a water fraction whose molecules are less similar to bulk in DODAC than in DODAB. FTIR analysis of interfacial water as a function of DODAX counterion, hydration state and temperature yielded a detailed picture of the distribution of the water structure and corresponding lipid order parameters.

4.4.3. Confined water within DODAB bilayers from MD simulations

Molecular dynamics (MD) simulations on the DODAB/water system were performed to gain complementary insights to the spectroscopic measurements. Unfortunately, crystal data, required to set up the coordinates for the lipid bilayers, were solely available for DODAB (Okuyama et al., 1988) impeding a comparative study of all four DODA halides. Methodological details of the MD simulations are given in (Woiterski et al., 2012) and its supporting material. In brief, the simulations were performed using the GROMACS 3.3.3 software package. Water molecules were modeled with the simple point charge (SPC) model (Berendsen et al., 1981; van der Spoel et al., 1998). DODAB was modeled using the parameters provided by Professor R. Böckmann (Computational Biology, Department Biologie, Universität Erlangen-Nürnberg, Germany) to implement the Berger lipid force field within GROMOS96 (ffG53a6) (Siu et al., 2008; Berger et al., 1997).

MD simulations were carried out on energy-minimized DODAB bilayers consisting of lipids, bromide ions and water, 128 constituents each. Bilayers had equilibrated after 100 ns and MD simulations were continued for 1 ns at a sampling rate of 50 fs. Trajectories with a length of 200 ps were analyzed to determine the orientation of DODAB and interfacial water molecules as well as translational and orientational motion. Figure 4.7 shows the mean-square displacement (MSD) as a function of time for water in DODAB bilayers and bulk SPC water. Slow diffusion of DODAB-associated water became clearly evident by its almost constant MSD(t). The inset of figure 4.7 (left) shows the MSD's saturation within short times, indicating confined diffusion of water within DODAB. On longer time scales, the MSD of DODAB water grew only slightly compared to bulk wa-

ter, which is reflected by a small diffusion coefficient $D = (1.35 \pm 0.74) \cdot 10^{-7}\,\mathrm{cm}^2/\mathrm{s}$. In contrast, for bulk SPC water a much larger $D = (4.02 \pm 0.05) \cdot 10^{-5}\,\mathrm{cm}^2/\mathrm{s}$ was determined. Furthermore, the orientation correlation function of SPC water in DODAB bilayers was found to decay much slower than that of bulk water (cf. figure 4.7, right), revealing also reduced rotational motion of water within DODAB. These results, firstly, confirm the spectroscopic finding that water between DODAB multistacks is strongly confined and, secondly, agree with other experimental and simulation studies of water-depleted phospholipid membranes (Zhao et al., 2008; Volkov et al., 2007; Berkowitz et al., 2006).

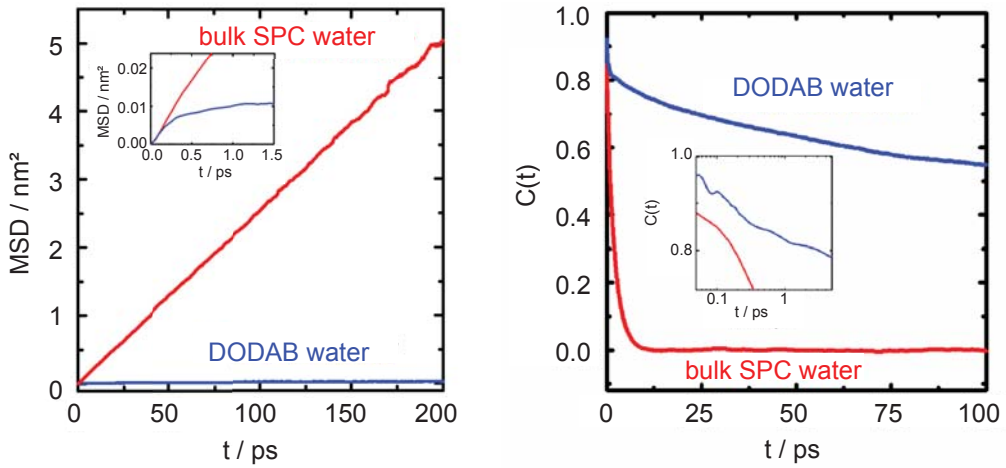

Figure 4.7.: *Left:* MSD *vs.* t plot of bulk SPC and membrane-associated water. *Inset:* Evidence for confined diffusion of SPC water within DODAB bilayers. *Right:* Decay of the rotation correlation. The functions indicate that reorientation of SPC water in DODAB bilayers is comparatively slow. The data are averaged over 128 molecules within the simulation. Images as published in (Woiterski et al., 2012).

A snapshot of a DODAB bilayer's MD trajectory after 100.2 ns simulation time is shown in figure 4.8. It illustrates that one octadecyl chains is kinked (Okuyama et al., 1988), whereas the major part of the alkyl chains is an all-trans conformation as found in the gel phase (figure 4.8A). Furthermore, it displays a detailed view on the interfacial region, particularly the location of water molecules and bromides that are involved in H bonding (figure 4.8B and C). In analogy to chain order parameters obtained by NMR spectroscopy for deuterated lipids (Seelig, 1977), a simulated chain segment order parameter $\langle S_{CD} \rangle$ of the alkyl chains' methylene groups was calculated and found to be $\langle S_{CD} \rangle = 0.098$. The corresponding tilt angle $\langle \theta_{CD} \rangle$ was converted to an average CH_2 tilt angle $\langle \theta \rangle = 39.17^\circ$, which relates to an IR chain order parameter $S_\theta = 0.402$. For the octadecyl chains of DODAB, this finding agrees very well with the IR spectroscopically measured S_θ. A small deviation can result from disorder of the investigated bilayer stacks due to imperfections in the experimental preparation.

The simulated positions of water molecules and bromides were analyzed in detail to

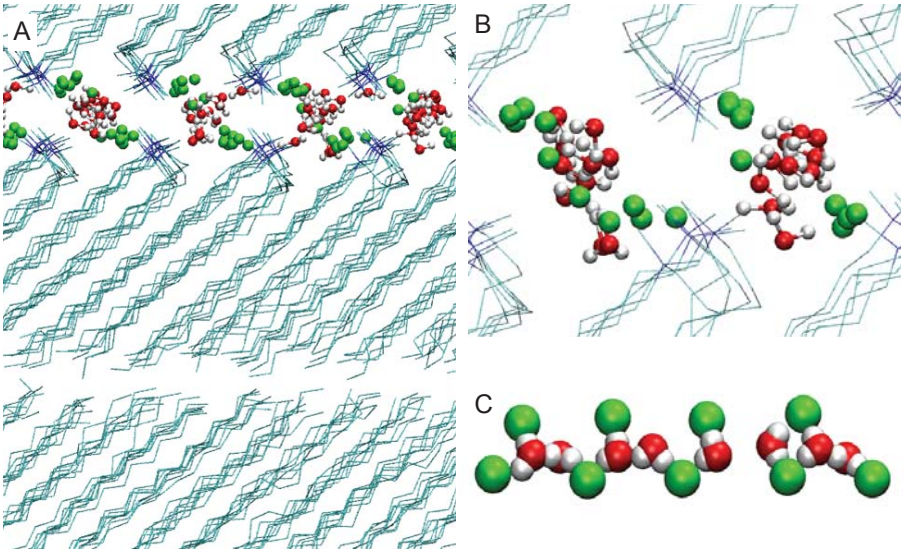

Figure 4.8.: Snapshot of a DODAB bilayer MD simulation at $T = 300$ K and $p = 1$ bar after 100.2 ns. View along the bilayer plane (b axis pointing into the plane of the picture). *A:* entire lipids within the bilayer, *B:* hydrophilic residues including water, *C:* detailed view on water molecules and bromide ions (green) highlighting the HBs between these species (other atoms omitted, different angle of view). Image as published in (Woiterski et al., 2012).

provide further structural insights on the behavior of water in DODAB bilayers. The orientations of the transition dipole moments of pure (uncoupled) symmetric and antisymmetric stretching modes of isolated water and of the stretching vibration along isolated (uncoupled) water OH bonds agree with the orientations of water dipoles μ, the HH vectors connecting the H atoms of each water molecule and the OH vectors defined by the direction and length of OH bonds. The orientation angles were calculated relative to the bilayer plane. Corresponding order parameters S_μ, S_{HH} and S_{OH} were computed for comparison with IR spectroscopic measurements. Finally, simulated water and bromide positions were analyzed to characterize involved HBs. Due to the simplicity of the SPC water model, a geometric definition of H bonding was used. The maximum HB length, which is defined as the first minimum of the radial distribution function, was found to be 0.30 nm between two water oxygen atoms and 0.40 nm between oxygen and bromide. The maximum HB angle was defined to be 30° (Auer and Skinner, 2009).

The distributions of the orientation angles θ_μ, θ_{HH} and θ_{OH} of DODAB-associated and bulk water, respectively, are given in (Woiterski et al., 2012). The water species giving rise to these orientation angles can be derived from simple considerations. If a single water molecule is considered as HB donor only, there are five H bonded water species possible within DODAB. Three double donor (DD) water species exist, which form HBs to two bromide ions (denoted as BWB), to two different water molecules (OWO, because water oxygen acts as acceptor) and to a bromide ion and another water (BWO). Furthermore, there are two possible single D water species with water H bonded to one bromide

Fraction		$\langle\theta_{HH}\rangle/^\circ$ (S_{HH})	$\langle\theta_{OH}\rangle/^\circ$ (S_{OH})	$\langle\theta_\mu\rangle/^\circ$ (S_μ)	Percentage
Average		55.3 (-0.01)	60.0 (-0.13)	69.8 (-0.32)	100
BWB	total	49.0 (0.15)	56.3 (-0.04)	72.2 (-0.36)	65
	DD	48.4 (0.16)	56.1 (-0.03)	70.9 (-0.34)	39
	ADD	49.6 (0.13)	56.4 (-0.04)	70.3 (-0.33)	26
BWO	total	69.3 (-0.31)	65.3 (-0.24)†; 72.3 (-0.36)‡	66.0 (-0.25)	25
	DD	70.1 (-0.33)		66.0 (-0.25)	23.5
	ADD	69.3 (-0.31)		67.2 (-0.28)	1.5
BW	total	57.1 (-0.06)	53.2 (0.04)^f; 68.1(-0.29)‡	66.6 (-0.26)	6.5
	D	56.7 (-0.05)		65.8 (-0.25)	4.8
	AD	58.1 (-0.08)		69.4 (-0.31)	1.7

Table 4.4.: Mean orientations and order parameters of SPC water in simulated DODAB bilayers for the average of all water molecules and the largest three fractions are BWB (DD to two bromides), BWO (DD to water and bromide) and BW (single D to bromide). Subfractions were defined by non-acceptance/acceptance of another HB. Orientation angles of two differently bonded OH bonds (defined by the vector from O to H) were separately analyzed. †OH groups bonded to water oxygen. ‡OH bonded to bromide. ^{f}Free OH groups. From (Woiterski et al., 2012)

(BW) or to another water molecule (OW). A sixth water species is represented by water (W) with two free protons. Each of these six water species can accept up to two water hydrogens by its oxygen.

The MD simulations revealed that (65.0 ± 5) % of the entire DODAB bilayer water belong to BWB, among these (40 ± 1)% of the molecules act as single acceptors (A) and only 0.1 % as double acceptors (DA). Hence, BWB water molecules form on average 2.4 HBs. BWO was shown to form the second largest fraction comprising (25 ± 3) % of water within DODAB. Out of these only 6 % formed an additional HB acting as A, giving rise to an average number of 2.06 HBs. In the BW species, which comprised (6.4 ± 1.5) % of DODAB water, a proton of a nearby water molecule was accepted by 25 %, giving an average number of 1.25 HBs. The remaining 3.5 % of DODAB water molecules were found to be split into HB D fractions comprising water with a single water molecule (OW, 2.5 ± 0.3 %), with two water molecules (OWO, 0.5 ± 0.2 %) and free water molecules (W, 0.5 ± 0.2 %). As the latter three species contributed only a small part to the entire water population, they were not further analyzed. The results for the three largest fractions are summarized in table 4.4.

The uniform shapes of BWB water's θ_{HH} and θ_{OH} distributions suggest a homogeneous water population (figure 5 in (Woiterski et al., 2012)). Moreover, BWB water molecules with no (DD) and with one accepted HB (ADD) were found to differ only slightly in their mean orientation angles and order parameters (cf. table 4.4). Thus, an additional HB did

not significantly modify the rotational freedom of water. This finding is in contrast to the properties of BW water, which is characterized one the one side by broader orientation angle distributions indicating a higher degree of rotational freedom. On the other side, BW water exhibited particularly large differences between D and AD subfractions, i.e., there was an effect of an additional HB on rotational motion for a D water molecule. Therefore, another accepted HB only influenced molecular rotation if it had not already been restricted by double H bonding of the water OH groups.

As a conclusion, it can be remarked that simulated SPC water molecules in DODAB are rotationally confined by varied H bonding to bromide ions or other water molecules resulting in differently oriented populations, which is in good qualitative agreement with the spectroscopic measurements presented in section 4.3. The most intense stretching band components of DODAB water at 3394 and 3444 cm^{-1} are loosely assigned to DDA and DD subpopulations of the BWB water fraction which is the largest found in simulated DODAB. Although the fractional sizes of these subpopulations do not agree with the relative intensities of the IR band components, there is a good accordance between the experimental order parameter S_{IR} and the corresponding S_{OH} value of OH bond directors. For D_2O stretching components the relative intensities roughly agree with the relative sizes of the modeled DDA and DD BWB fractions. However, the order parameters S_{IR} and S_{OH} show a stronger deviation between experiment and simulation. The behavior of the D_2O stretching modes within these membranes can differ from H_2O.

A generic correlation between average orientations of simulated water fractions and experimentally observed average orientations of all water populations was not found, possibly due to molecular coupling. Water molecules in DODAB samples cannot be considered isolated, since H bonding to one neighbored water molecule occurs for about 50 - 60 %. Coupled oscillations have dipole moments different from those of the underlying molecular fundamentals. The difference between experiment and simulation regarding average orientations of DDA BWB molecules is significantly larger than observed for the DD BWB. While the latter might approximate uncoupled OH stretching oscillators, increased intermolecular coupling in DDA molecules is assumed to induce stronger deviation from the fundamental. In synopsis, by controlling the degree of hydration and through counterion exchange the unusually strong structured water in the proximity of the model lipid membranes was revealed, demonstrating the dramatic extent to which biological assemblies can influence the surrounding water layer, which in turn influences subsequent interfacial events.

5. Neuronal Growth on Lipid Bilayer Substrates – From Single Cells to Networks

In the last chapter it was shown how a membrane matrix influences the structure of water molecules which are bound between the lipid bilayers. In the following, a completely different feature of membranes is elucidated – their application as substrates for neuronal growth. As described in section 2.2 polymer-tethered lipid bilayers are widely used as model system for cell-cell interactions (Tanaka and Sackmann, 2005). The potential of modulating the membrane's viscosity and frictional coupling (Minner, 2010; Purrucker et al., 2005) makes these substrates attractive for studying the mechanosensitive behavior of cells. The ability of cells to react on mechanical stimuli from their surroundings and follow gradients of varying substrate stiffness is called mechanotaxis or durotaxis (Lo et al., 2000). While this comportment was reported for various cell types (Engler et al., 2006; Discher et al., 2005; Lo et al., 2000), in this work, the focus is on the exploration of neuronal cells which were reported to show "inverse durotaxis". *In vitro* neurons preferred to grow on soft substrates (Georges et al., 2006; Flanagan et al., 2002) or directed their neurites towards softer 3D collagen gels (Sundararaghavan et al., 2009). However, although there is large number of experimental studies, there is no consensus which of the neuronal growth parameters are sensitive to changes in the substrate rigidity and the mechanisms of mechanotaxis are still poorly understood (Moore and Sheetz, 2011; Franze and Guck, 2010). Thus, the phenomenon of inverse durotaxis remains elusive to this day.

The experiments presented in the first part of this chapter shall give further insights into neuronal mechanosensitivity. Therefore, neurons of the NG108 cell line and primary retinal ganglion cells (RGCs) were cultured on tethered and supported lipid bilayers. These two types of substrates vary in their viscosity in analogy to hydrogels of different stiffness. The growth of individual cells was analyzed using phase contrast microscopy and subsequent tracking of neurites. The quantification of neurite growth comprises the

neurite length and branching in dependence of the membrane fluidity. Furthermore, a time-resolved analysis revealed long-term outgrowth speeds as well as outgrowth and retraction rates of single neurites. The results are presented in section 5.1.

The second part is dedicated to the collective cell growth, i.e., the formation of complex neuronal networks. A descriptive picture of developing RGC networks is given followed by a detailed characterization of the morphological networks. Therefore, topological maps were abstracted from the phase contrast images of RGCs and analyzed by means of graph theory. Typical network parameters such as the connectivity, shortest path length, edge length and the clustering coefficient were determined from the adjacency matrix and are presented (section 5.2). In particular the time-resolved monitoring of the early developing network revealed different stages of network complexity and it will be shown how a network optimizes its architecture. Like other neuronal networks, RGC networks belong to the small-world networks (Watts and Strogatz, 1998) as discussed at the end of the section. The results of the RGC network formation are published which will inevitably lead to an overlap between (Woiterski et al., 2013) and section 5.2 and 5.3 which will not always be referenced.

5.1. Mechanosensitivity of neurons on substrates with different viscosity

Before studying neuronal growth on lipid bilayer substrates, fluorescence recovery after photobleaching (FRAP) experiments were carried out as a qualitative control for the different fluidities of tethered and supported bilayers, tBLs and sBLs, respectively. Therefore, the outer bilayer leaflet was enriched with a fluorescent dye (Texas Red®-DHPE) as described in section 3.5. The upper part of figure 5.1 displays epifluorescent micrographs of a POPC sBL (A) and POPC tBLs with 5 mol% $PMOx_{50}$ (B) and 30 mol% $PMOx_{50}$ (C) after 2 min, 1 min and 3 min bleaching, respectively. The lower part shows the fluorescence recovery after 2 min. The tBL with low linker density shows a strong bleaching and a fast recovery (B), while the tBL with high lipopolymer concentration exhibits a very weak recovery of the fluorescence signal (C). Furthermore, the latter micrograph clearly reveals structural inhomogeneities comparable to the blistered structures described for a tBL system composed of 1-stearoyl-2-oleoyl-*sn*-glycero-3-phosphocholine (SOPC) and 30 mol% $PMOx_{50}$ (Siegel et al., 2010). Thus, tBLs with 30 mol% $PMOx_{50}$ were not used as cell substrate to exclude effects of the bilayer's height differences on the neuronal growth behavior.

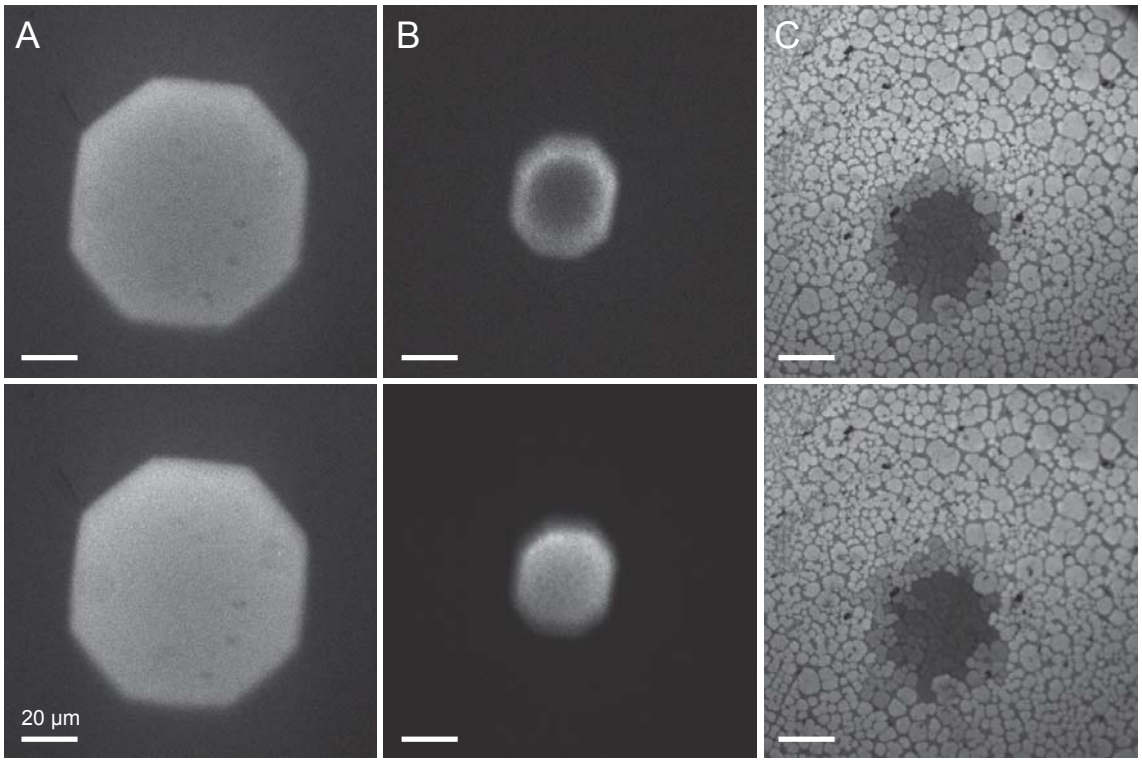

Figure 5.1.: Fluorescent micrographs of a pure POPC supported bilayer (A) and polymer-tethered lipid bilayers with POPC and 5 mol% (B) and 30 mol% (C), respectively, directly after bleaching (top) and fluorescence recovery after 2 min (bottom). Scale bars are 20 µm.

5.1.1. Analysis of neurite length and branching

First experiments were performed with the NG108 cell line. Therefore, NG108 cells of the same culture were seeded on two Petri dishes with a tBL and sBL substrate, respectively. Neurons adhered and started the formation of processes after several hours. Images of NG108 cells were acquired at ~ 100 locations on the Petri dish after 3 days in culture. Figure 5.2 shows several NG108 cells on fluid tBLs (A) and more viscous sBLs (B) with traced neurites (blue). The contour of the neurites was generated using *NeuronJ*, a plug-in of ImageJ as described in section 3.8.1. Three different types of neuronal morphologies can be distinguished: (i) cells with outgrowths that possess a high number of branches (figure 5.2, top), (ii) cells with very long neurites (up to ~ 900 µm, middle) and (iii) cells with primarily shorter neurites (≤ 80 µm, bottom). The occurrence of shorter neurites could be influenced by the surrounding cell density and will be discussed below. Since at first glance NG108 cells exhibit each of the characteristics on both types of substrates, a closer examination of the growth parameters becomes necessary.

Neurite growth of NG108 cells was quantified by determining both the maximal neurite length and number of branches per outgrowth after 3 days in culture. Processes were traced starting from the soma to the leading tip without distinguishing between axons and dendrites. The length and branching per outgrowth was quantified using Matlab

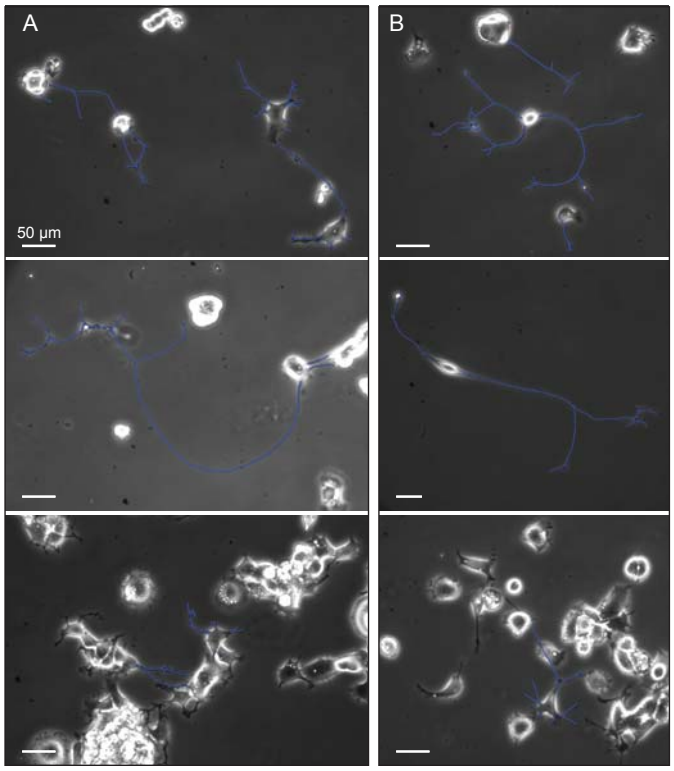

Figure 5.2.: Morphology of NG108 cells cultured for 3 days on a tBL (left) and a sBL (right), respectively. All scale bars are 50 µm.

(cf. section 3.8.1). Figure 5.3 shows the distributions of the maximal neurite length and number of branches (inset) per outgrowth on tBLs (blue) and sBLs (red), respectively. Bin sizes were 10 and 1 for the length and branch distributions, respectively. The graphs comprise data of 7 samples for each substrate as summarized in table 5.1.

On both substrates a large fraction of short neurites (< 20 µm) and a broad continuum of lengths up to 400 µm were observed. Above this threshold, significantly fewer neurites were found – in single cases they grew up to a length of 890 µm (for clarity not shown in figure 5.3). The neurite length was also examined regarding a potential dependence on the free space available for an extending process (data not shown). For this purpose, the area occupied by surrounding cells within a half-circle of radius $r = 200$ µm was quantified as described in section 3.8.1. However, there was no visible effect of the substrate: on both tBLs and sBLs long neurites (up to 300 µm) were observed for low cell densities (~ 30 % coverage) as well as short neurites (< 100 µm) at higher cell densities (up to 75 % coverage). In spite of these common features, shorter lengths (20 µm - 80 µm) were observed more frequently for neurites grown on sBLs, while a larger number of longer neurites (80 µm - 300 µm) appeared on tBLs. The distributions of the number of branches per outgrowth (figure 5.3, inset) appears very similar for both types of substrates. Nevertheless, neurons cultured on tBLs exhibit more branches in the higher regime, i.e., ≥ 5

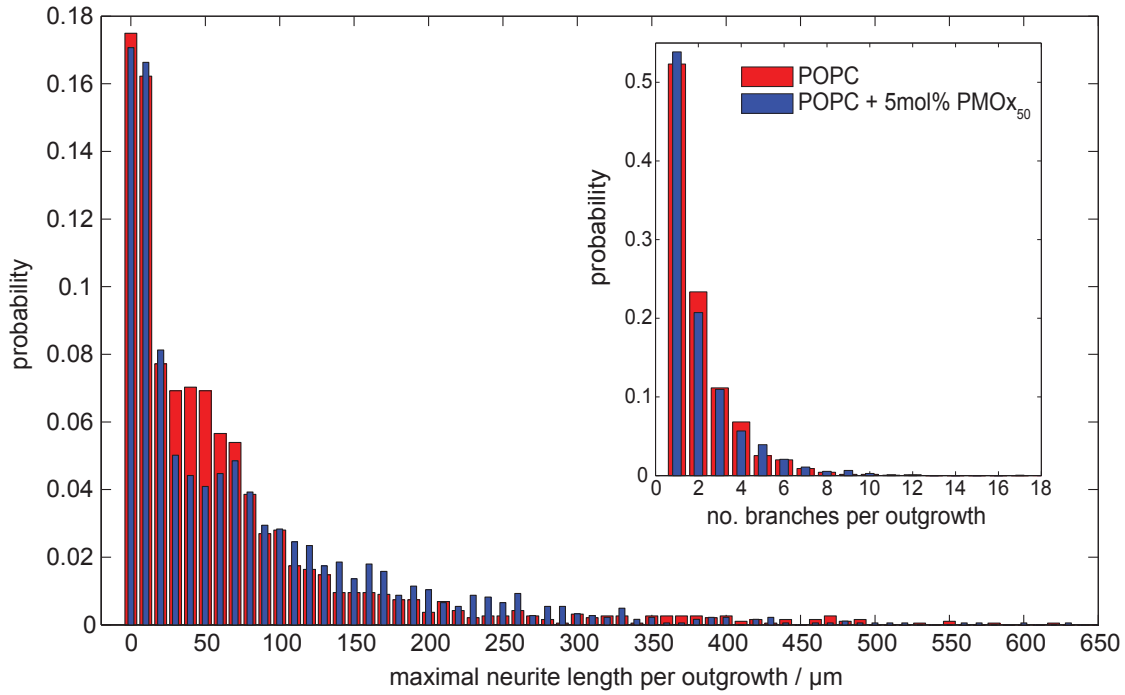

Figure 5.3.: Distributions of the maximal neurite length and number of branches (*inset*) per outgrowth of NG108 cells cultured on a tBL (blue) and sBL (red). For clarity lengths between 650 µm and 900 µm are not shown.

branches per outgrowth.

The neurite length as well as the number of branches per outgrowth were neither normally nor exponentially distributed. Therefore, Kolmogorov-Smirnov tests were used to test for significant differences between tBLs and sBLs. The data are presented in box-and-whisker plots specifying the median as well as upper and lower quartiles (see figure 5.4). The figure also shows the number of branches per millimeter of neurite length. This parameter was calculated for each of the seven samples as a fraction of the total number of branches and the total neurite length. It was found to be normally distributed (ANOVA test). The applied statistical tests only unveiled significant differences for the maximal

Parameter	tBL	sBL
Number of cells	633	647
Number of neurites	3782	3765
Length of longest neurite per outgrowth[a] /µm	47.28	42.37
Number of branches per outgrowth[a]	1	1
Number of branches per cell[b]	5.93 ± 0.38	5.87 ± 0.40
Number of branches per mm neurite[b]	14.43 ± 2.15	17.87 ± 2.64

Table 5.1.: Summary of analyzed NG108 cells cultured on tBLs and sBLs. The data include 7 samples for each substrate. [a]Median, [b]average value.

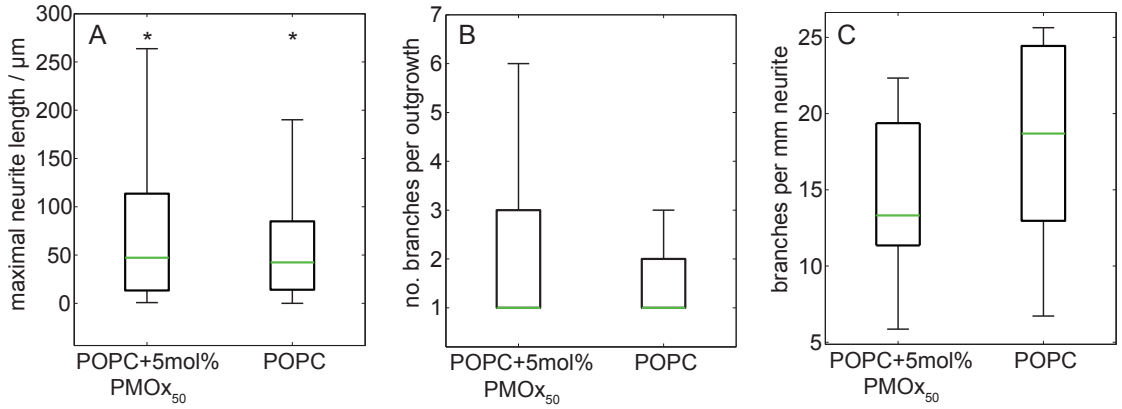

Figure 5.4.: Box-and-whisker plots of the maximal neurite length per outgrowth (A), number of branches per outgrowth (B) and branches per millimeter neurite (C). The boxes mark the 25 % and 75 % quartiles of each distribution and are bisected by the median (green). Whiskers display 5th and 95th percentiles, outliers were omitted for clarity. The distributions were tested with Kolmogorov-Smirnov (A, B) and ANOVA (C) tests. Significant differences between the two substrates were only found for the maximal neurite length ($p < 0.001$) as indicated by the asterisks.

neurite length per outgrowth (Kolmogorov-Smirnov test, $p < 0.001$) as indicated by the asterisks. The median of the maximal neurite length on tBLs was found to be slightly higher than the corresponding value on sBLs (cf. table 5.1). However, the number of branches per outgrowth ($p = 0.633$) and branches/mm neurites ($p = 0.423$) were very similar and not significantly different for NG108 cells cultured on tBLs and sBLs.

5.1.2. Analysis of neuronal outgrowth speeds

In addition to the experiments with NG108 cells, further experiments were performed with primary neurons from mice. Therefore, retinal ganglion cells (RGCs) were plated on the same tBL and sBL substrates as NG108 cells. The only difference was the supplemental use of LN-211 as coating protein which is more physiological for the primary cells (cf. section 3.4). Time-dependent RGC growth was monitored as described in sections 3.7 and 3.8.2. In the previous section neurite length and branching of NG108 cells were analyzed. Since the neurite length was the only parameter which showed slight differences on both substrates, RGC growth was investigated with regard to neurite growth speeds. The long-term neurite extension was quantified by determining the absolute neurite length in an image relative to its length in the initial image. Therefore, images were considered in time intervals of one hour. Please note, that in the following outgrowth speeds will be related to neurite ages. As RGC growth was monitored starting 17 - 20 h after plating the cells and ended after 38 - 41 h, the time *in vitro* is larger than the neurite age. The latter was set to zero at the beginning of the observation or when an individual

neurite started to grow out at a later point in time.

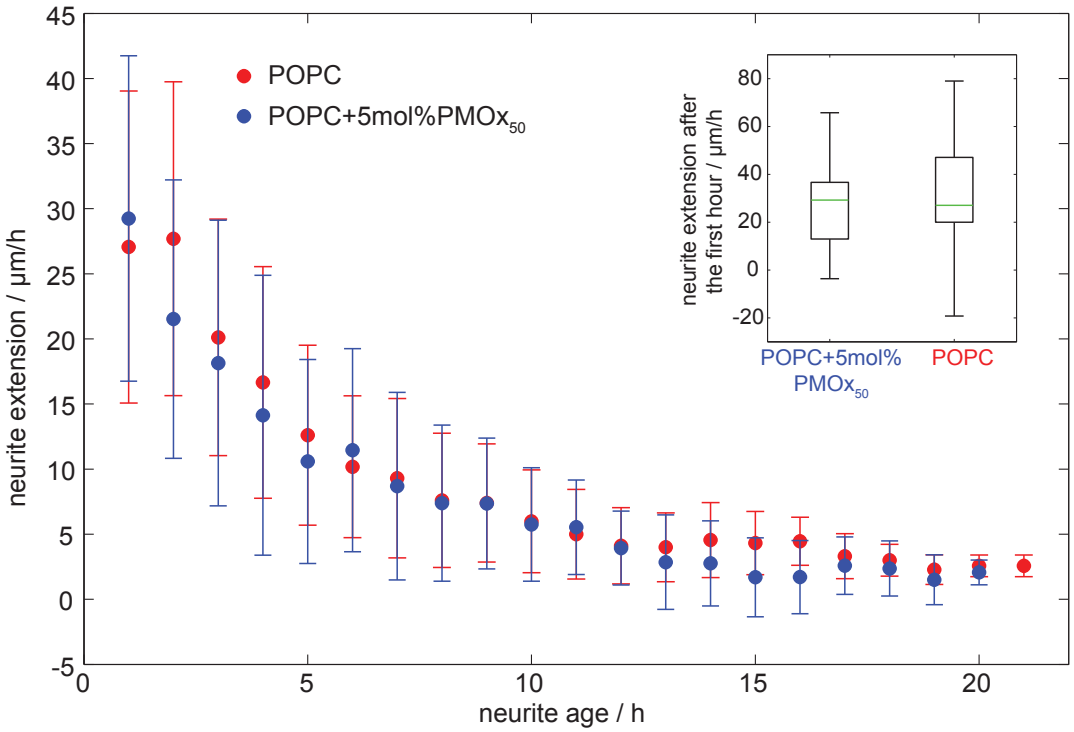

Figure 5.5.: Long-term neurite outgrowth speed of retinal ganglion cells (RGCs) on tBLs (blue, n=60) and sBLs (red, n=43). The values correspond to the median and error bars show the median absolute deviation (MAD). *Inset:* Box-and-whisker plot of the outgrowth speeds after the first hour.

Figure 5.5 shows the neurite outgrowth speed in dependence on the neurite age for RGCs cultured on tBLs (blue) and sBLs (red), respectively. Moreover, box-and-whisker plots with median as well as upper and lower quartiles are given exemplarily for the neurite extension after one hour in the inset. For both substrates, the long-term extension rates were not normally distributed (Kolmogorov-Smirnov test, $p < 0.001$). Although after one hour the median on tBLs (29.25 µm/h) was found to be slightly higher than on sBLs (27.06 µm/h), at most time points the long-term speed was higher on sBLs. Moreover, Kolmogorov-Smirnov tests after 1h, 2h, 5h, 10h, 15h and 20h revealed that there were no significant differences between the distributions of the outgrowth speeds on tBLs and sBLs ($0.311 \leq p \leq 0.947$). Another common feature for both substrates is that the observed outgrowth speeds show strong variations as reflected by the large error bars which correspond to the median absolute deviation (MAD). Neurite growth appears very similar on both substrates. While young neurites feature high outgrowth speeds between 15 and 30 µm/h, the speed continuously decreases to values $\sim 3.4 \pm 2.7$ µm/h. It has to be noted that not all of the neurites grew for the entire time range, since some processes retracted and disappeared while others only started growing in time course of the obser-

vation. Neurites were considered in the analysis if they were detected at least over 4 h, i.e., 5 successive frames. Thus, from the initial 60 (43) neurites on tBLs (sBLs), after 10 h only 22 (26) neurites remained and after 20 h their number reduced to 6 (4).

In contrast to the long-term growth speed, the short-term outgrowth rates were determined by dividing the difference in neurite length between two successive image frames by the time step (5 or 6 min). This analysis yields the fluctuations in the neurite growth as shown in figure 5.6. Positive growth rates correspond to a further elongation of the neurite, while negative rates imply a neurite retraction. Figure 5.6 shows that neurite growth is a highly dynamic process with rapid changes between phases of extension and retraction. This finding holds for both substrates, where the rates primarily fluctuated between +1 µm/min and -1 µm/min.

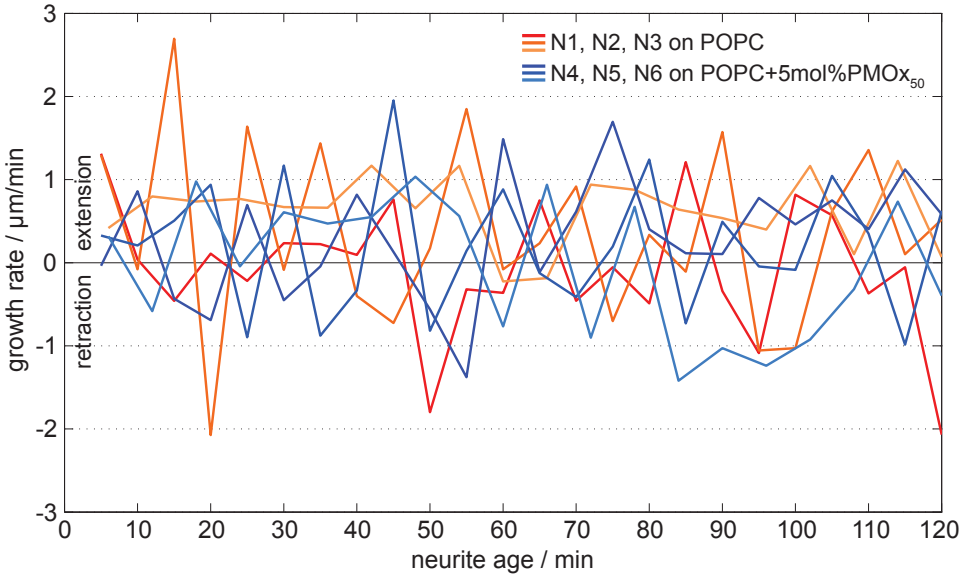

Figure 5.6.: Fluctuation of the growth rates of six individual RGC neurites from different cell preparations during the first 2 h of observation. The neurites N1 to N3 (reddish) were observed for RGCs cultured on sBLs, while N4 to N6 (blueish) are from RGCs cultured on tBLs. The line at y = 0, displayed to guide the eye, separates the two regimes of extension and retraction.

The data of all neurites is summarized in figure 5.7. It shows the time dependence of growth rate's median and its MAD for four different cell preparations. The medians assume predominantly positive values, i.e., the overall behavior of neurites is characterized by steadily growth. However, in agreement with the fluctuations described above (figure 5.6), the medians slightly oscillated during the entire monitored time span. One of the RGC preparations (red circles) exhibited a very slow outgrowth as reflected by the comparably low growth rates. However, this behavior is solely attributed to circumstances of that single cell preparation and cannot be generalized as slower growth on sBLs as reflected by the high growth rates on the other sBL substrate (orange circles). The large error bars for the first points at 5 min have to be ascribed to the method of detecting

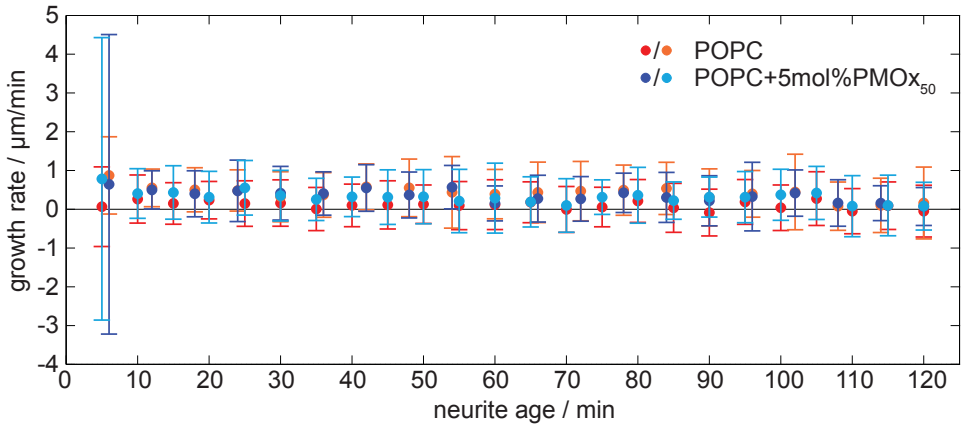

Figure 5.7.: Growth rates of RGC neurites during the first 2 h of observation. The data (median and MAD) comprise results of four primary cell preparations cultured on sBLs (red: n=67, orange: n=55) and tBLs (dark blue: n=50, light blue: n=61). Images were taken every 5 min (red; light blue) and 6 min (orange; dark blue), respectively.

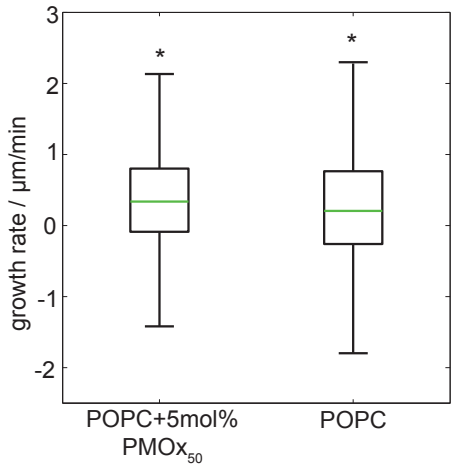

Figure 5.8: Box-and-whisker plots of the neurite growth rates on tBLs (left, n=1937) and sBLs (right, n=2309). Boxes bisected by the median (green) mark the 25 % and 75 % quartiles of each distribution and whiskers the 5th and 95th percentiles. Outliers were omitted for clarity. The distributions of the growth rates from RGCs cultured on tBLs and sBLs were significantly different (Kolmogorov-Smirnov test, $p < 0.001$) as indicated by the asterisks.

newly grown neurites. When a neurite branches, the new outgrowth was not detected starting from the branching point, but from the soma which leads to a large neurite length increase within the first time increment.

A statistical analysis of the growth rate distributions at each time step was performed. Kolmogorov-Smirnov tests yielded that growth rates for $t < 85$ min were not normally distributed ($p < 0.05$). In contrast, at later times the growth rates exhibited normal distributions ($p > 0.49$). The growth rates were further checked for significant differences between the two types of substrates. When comparing all growth rates independent of the point in time, the median of the growth rates measured on tBLs (0.34 ± 0.77 µm/min) exceeded those found for sBLs (0.21 ± 0.66 µm/min) as illustrated in the box-and-whisker plot in figure 5.8 and were significantly different (Kolmogorov-Smirnov test, $p < 0.001$). The results of both neuronal cell types will be discussed in section 5.3.

5.1.3. Characterization of the diffusion in tethered and supported lipid bilayers

The lateral lipid mobility within the planar lipid bilayers was quantified by FRAP experiments as described in section 3.5. Normalized fluorescence recovery curves for each bilayer system are shown in figure 5.9. The characteristic diffusion time, i.e., the half-time of the fluorescence recovery, $t_{1/2}$, and the intensity of the full recovery at $t \to \infty$, I_∞, were determined by fitting a single-exponential function to the FRAP curves. The diffusion coefficient, D, was then calculated using equation 3.1. The average values of 6 and 7 bleaching experiments for sBLs and tBLs, respectively, were found to be $D_{\mathrm{sBL}} = 3.15 \pm 0.63\,\mu\mathrm{m}^2/\mathrm{s}$ and $D_{\mathrm{tBL}} = 1.41 \pm 0.48\,\mu\mathrm{m}^2/\mathrm{s}$. Furthermore, the corresponding immobile fractions were determined to be $IF_{\mathrm{sBL}} \approx 30\,\%$ and $IF_{\mathrm{tBL}} \approx 40\,\%$.

Against the expectations which relied on results of an earlier study (Naumann et al., 2002), sBLs were slightly more fluid than polymer-tethered lipid bilayers. It also has to be noted that although the recovery in the tBL obviously occurs faster than in the sBL (see figure 5.9), the radius of the bleached spot r_{tBL} was only half of the corresponding r_{sBL}. As $D \propto r^2$, this has a direct influence and can be one possible reason for $D_{\mathrm{sBL}} > D_{\mathrm{tBL}}$.

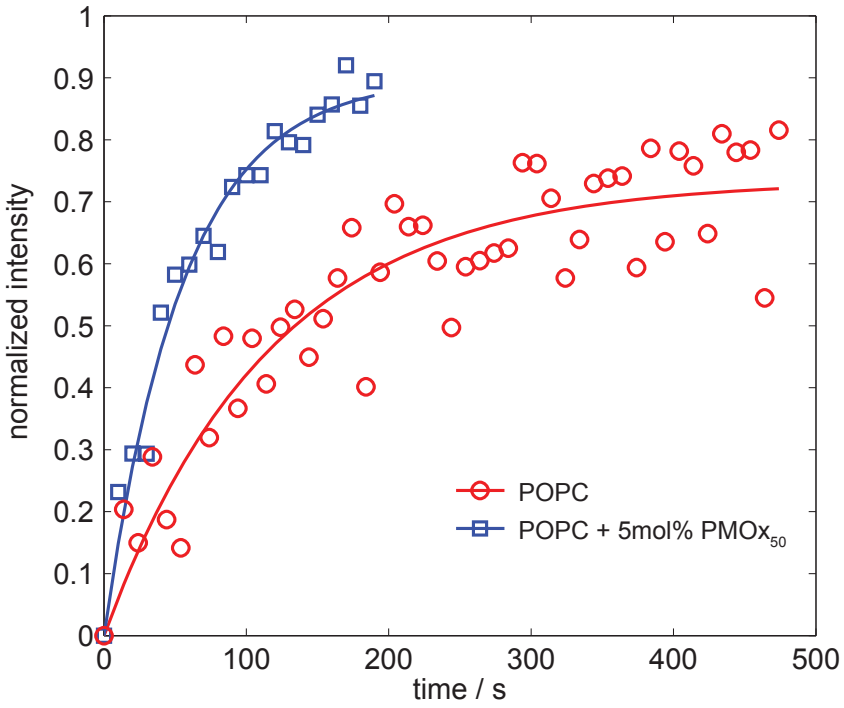

Figure 5.9.: Normalized fluorescence recovery curves with exponential fit measured for a sBL (red) and tBL (blue), respectively. Both outer leaflets were labeled with 0.5 mol% NBD-PE.

5.2. Network formation of RGCs

5.2.1. Growth stages of developing RGC networks

Neuritogenesis of retinal ganglion cells (RGCs) cultured on tethered lipid bilayers was observed starting 17 - 20 h after seeding. Figure 5.10 shows snapshots of a developing RGC neuronal network and the corresponding topological graphs at four different stages. The entire movie of the growing network is provided as supporting material in (Woiterski et al., 2013).

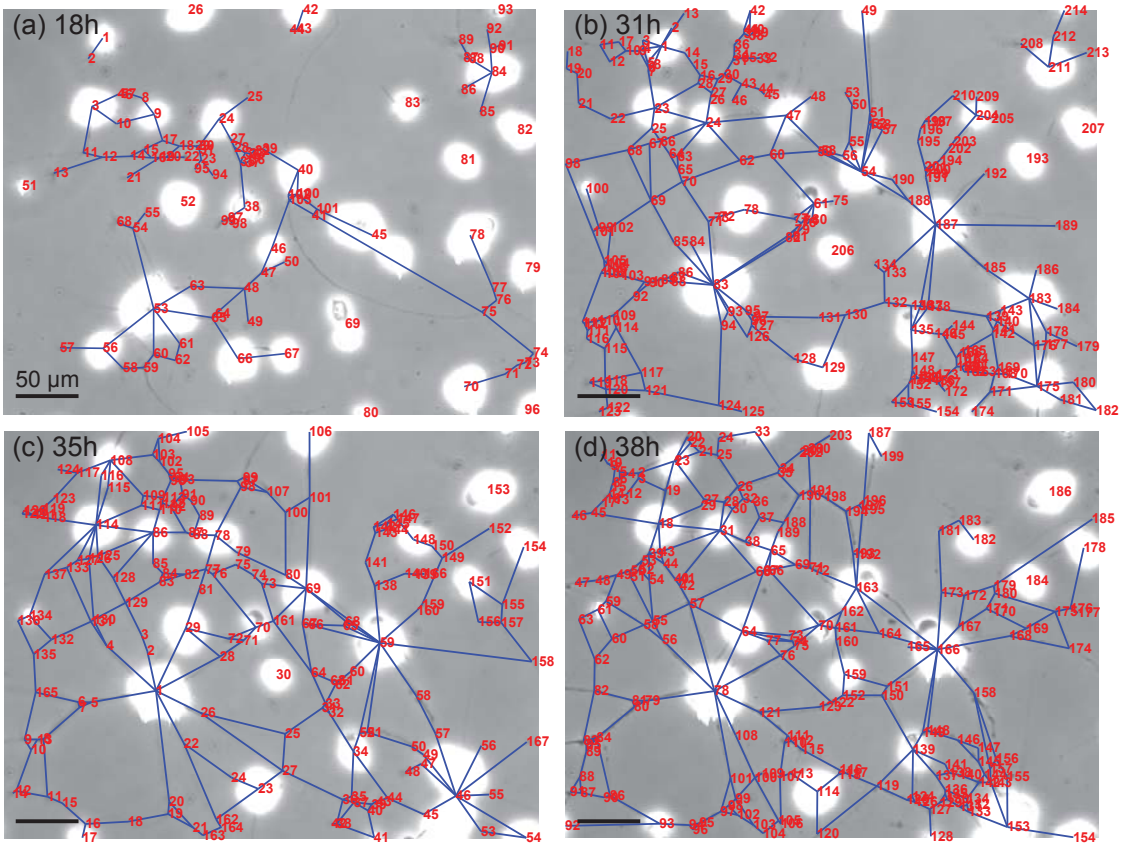

Figure 5.10.: Development of an RGC network. The phase contrast images and overlaid topological graphs show the network (a) when starting the observation after 18 h *in vitro*, (b) at the maximum complexity (31 h), (c) after the optimization (35 h) and (d) at the end of the observation (38 h). Vertices were marked by red numbers, existing connections by blue edges. Scale bars correspond to 50 µm. The cell density was 202 cells/mm^2. Image as published in (Woiterski et al., 2013).

At the beginning, isolated RGCs showed neurites, while small networks were rarely observed (see figure 5.10 a). Extending neurites initiated branching and formed connections to other cells which thereby got activated and formed new outgrowths. A self-avoidance of neuronal connections was not observed, i.e., neurites connected to outgrowths of one and the same cell. "Activation" of most of the cells occurred approxi-

mately until 19 - 23 h *in vitro*. With ongoing time, the cells formed new processes, which sometimes followed the path of already existing neurites before branching again. Thus, the network became more elaborate by formation of further connections to existing neurites or other cells (including multiple connections between two neighboring cells) until reaching a maximal complexity (figure 5.10 b) after 30 - 36 h *in vitro*. At that stage, the network displayed a high level of arborization and many short neurite segments. During the entire observation, neurites kept growing out and formed further connections. However, after reaching the maximum complexity, the dominant effect was an optimization of the network. The reduction occurred by the fusion of parallel neurites to strengthened bundles, the weakening or removal of neurites as well as the clustering of cells by migration of somata along a connection (figure 5.10 c). Along with this finding, a straightening out of neurites was observed. Towards later points in time (35 - 41 h *in vitro*), some networks underwent enhanced neuronal beading and aging of neurites which influenced the network's reduction process and could not be distinguished from "real" optimization. Nevertheless, RGCs were still viable (see section 3.8.3) and showed the same behavior as neurons without neuronal beading.

Already simple parameters indicate distinct properties of the neuronal networks at different temporal stages. In contrast to the start, maximum networks exhibited much larger numbers of vertices and connections as summarized in table 5.2. Furthermore, the number of non-connected cells decreased drastically. For optimized networks, both the average number of connections as well as the average number of vertices dropped by approximately 20 % in comparison to maximum networks.

	Start	Maximum network	Optimized network
Vertices	52 ± 6	142 ± 21	112 ± 17
Edges	40 ± 8	175 ± 31	143 ± 27
Non-connected cells	13 ± 2	5 ± 1	4 ± 1

Table 5.2.: Network parameters for different stages during the network formation of RGCs. Mean value and SEM of the number of vertices, the number of edges and the number of non-connected cells (averaged over 13 networks resulting from three primary cell preparations).

Another feature of the networks is that not all neurons were in the same stage at same time. A closer look to the center of figure 5.10 (b) reveals a maximum complexity of the network as reflected by the high density of vertices. While in figure 5.10 (c), this central area clearly shows a reduction, the complexity increases in the upper left corner. The same remodeling effect can be observed in figure 5.10 (d), where the upper left area is already optimized, but cells in the lower right part show enhanced branching. This finding can be either attributed to different RGC subtypes which may vary in their outgrowth

behavior (Kim et al., 2010) or to variations in the growth cone dynamics, i.e., diverse phases of growth and collapse. Thus, the exact determination of the point in time when the network assumes a certain stage is complicated and will be discussed in the following section.

5.2.2. Quantification of the network stages

The time-resolved analysis of connectivity, k, shortest path length, L, as well as edge length, d, provides further insights into the evolving network. Therefore, network graphs were analyzed in time steps of 90 min. In figure 5.11, the temporal development of the the number of vertices, connectivity, path length and edge length are given for the network shown in figure 5.10. All values are medians of the corresponding distributions. As expected, the number of vertices started to increase up to a maximum value which coincided in most of the cases with the highest network complexity. For several networks, a sharp peak was not observed in the time dependence of the vertices but rather a plateau. Therefore, maximum and also optimized networks were judged by means of several criteria. *Maximum networks* were characterized by a high number of vertices combined with a large path length and a small edge length. After the simplification, *optimized networks* were observed, these are defined as networks that possess a reduced number of vertices and edges (see table 5.2), a decreased path length and a simultaneous increased edge length. These conditions were met as indicated in figure 5.11 by the red and blue arrows for the maximum and optimized network, respectively.

As the network formed, the connectivity of single vertices was found to increase from $k = 2$ from the initial network stage to $k = 3$ for maximum networks. The shortest path length also increased showing slight fluctuations until reaching the highest value for the maximum network. For all samples, a reduction of the path length was observed for the optimized network. As mentioned above, at the stage of the maximum network, the system is characterized by many short segments. This is reflected by a decrease of the edge length to a minimum value. The restructuring of the network together with the observed straightening out of connections caused another increase of the edge length for the optimized network. The last two data points in figure 5.11 show a contrary trend for the number of vertices, path length and edge length. This behavior has to be attributed presumably to the interplay of retraction and outgrowth, in this case the new outgrowth of neurites. However, the other networks did not show this trend. Thus, the quintessence regarding the differences between maximum and optimized networks was not affected.

Figure 5.12 shows the distributions of the connectivity, shortest path length and edge length at prominent stages during the course of network formation, i.e., at the begin-

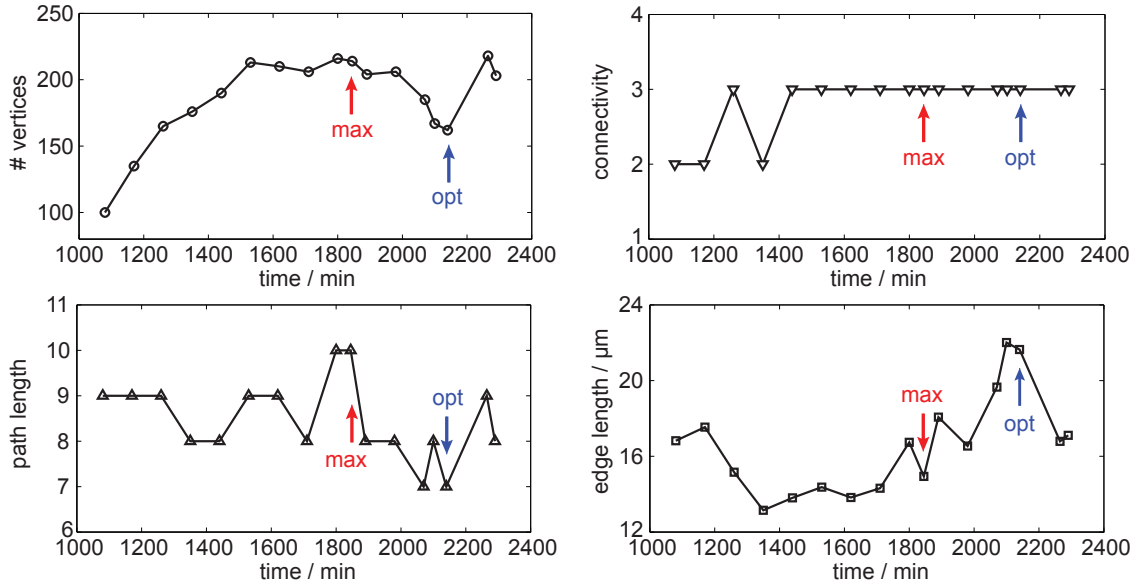

Figure 5.11.: Temporal changes of the number of vertices, connectivity, shortest path length and edge length for the developing RGC network shown in figure 5.10. The network with maximum complexity and the optimized network were marked with a red and blue arrow, respectively. (Image as published in (Woiterski et al., 2013).

ning of the observation (red), the maximum (blue) and the optimized network (green). The distributions comprise data of 13 networks resulting from three cell preparations. Therefore, the absolute numbers partly deviate from the published work (Woiterski et al., 2013), where the distributions of solely one network were considered, namely the network shown in figure 5.10. Given values correspond to the median and the MAD.

At the start, there is a large number of isolated cells or branching points ($k = 0$) and only few vertices are connected (figure 5.12, left). Thus, the connectivity was found to be $k_{\text{start}} = 1 \pm 1$. For higher developed networks, i.e., maximum and optimized networks, the number of neighboring vertices increased to $k_{\text{max/opt}} = 3 \pm 1$. Statistical analysis revealed that the distributions were not normally distributed (Kolmogorov- Smirnov test, $p < 0.001$). Furthermore, there were significant differences between the connectivity distribution of initial and maximum networks (Kolmogorov-Smirnov test, $p < 0.001$), but not between maximum and optimized networks (Kolmogorov-Smirnov test, $p = 0.359$).

The connectivity distributions of maximum and optimized networks are rather symmetric, i.e., in the low connectivity wing, RGC networks exhibited only few vertices with only one or two neighbors. The shape of the distribution gives further information about the underlying networks. Firstly, the connectivity distribution could not be fitted with a power law, suggesting that the connectivity was not scale-free (Amaral, 2000). Secondly, it clearly displays a long tail, i.e., high node degrees of up to $k = 14$ which indicate the existence of network hubs (Bullmore and Sporns, 2009).

The path length distributions were found to be very broad for initial and maximum networks (figure 5.12, right, top) assuming values in the range between 5 and 25. The largest path lengths of up to $L = 32$ were determined for maximum networks. For initial networks, a path length of $L_{\text{start}} = 6 \pm 4$ was found. With increasing complexity the path length grew and peaked in $L_{\text{max}} = 10 \pm 4$ for maximum networks. As the network evolved further, there was a clear shift towards shorter path lengths, which manifests in the decrease of the path length to $L_{\text{opt}} = 8 \pm 3$ corresponding to a reduction of 20 %. The increased path length from initial to maximum networks as well as its reduction for optimized networks were confirmed to be statistically significant by Kolmogorov-Smirnov tests ($p < 0.001$).

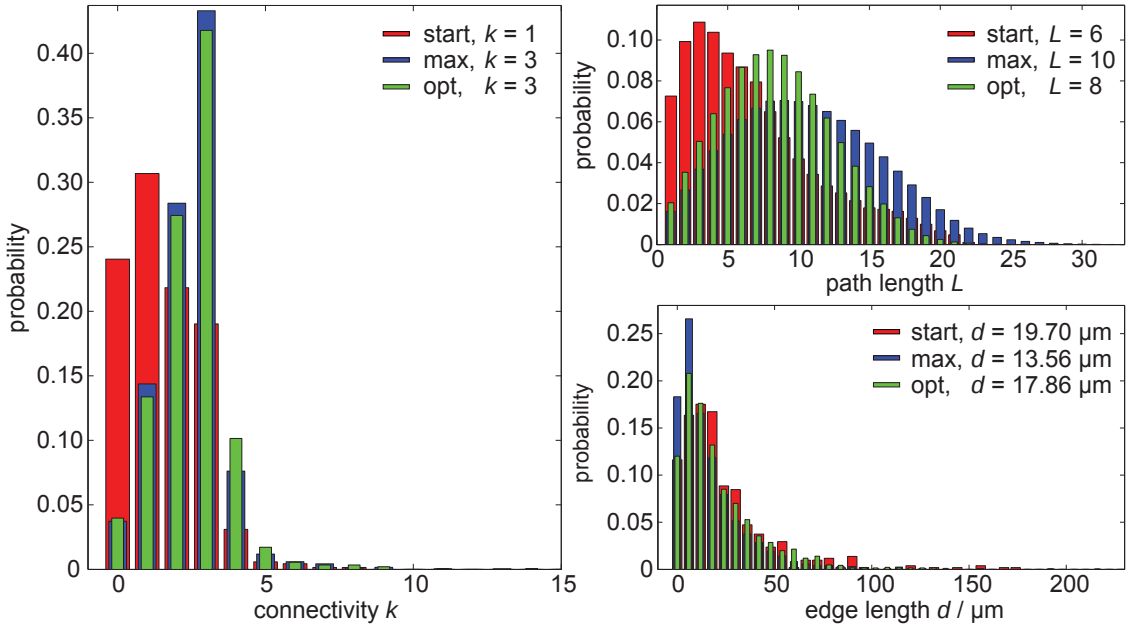

Figure 5.12.: Distributions and medians of the connectivity, shortest path length and edge length resulting from 13 RGC networks at different stages of early network formation. *Red*: networks at the start of the observation (678 vertices, 514 connections), *Blue*: maximum networks (1850 vertices, 2275 connections), *Green*: optimized networks (1458 vertices, 1856 connections).

Edge length distributions for the striking stages are displayed in figure 5.12 (right, bottom). They reveal the existence of a large number of short edges ($d \leq 12\,\mu\text{m}$) at the beginning of the network formation (bin size 6 µm), which is even exceeded in the maximum network. Most of the connections exhibited lengths between 10 µm and 100 µm, although edge lengths up to 230 µm were observed at all stages during the network development. At the beginning, when few vertices were present, a high value of the edge length was found ($d_{\text{start}} = 19.70 \pm 16.37\,\mu\text{m}$). With increasing complexity, it decreased to $d_{\text{max}} = 13.56 \pm 12.87\,\mu\text{m}$ which corresponds to a reduction of 31 %. For optimized networks, the edge length distribution shifted to higher values reflected by an increase of 32 % to $d_{\text{opt}} = 17.86 \pm 15.60\,\mu\text{m}$. This is attributed to the remodeling and simplification

of the network accompanied by the observed straightening out of edges. As above for the path length, the changes of the edge length distributions for the three stages were determined to be statistically significant (Kolmogorov-Smirnov tests, $p < 0.001$).

5.2.3. Small-world analysis

In the last section, the focus was on the temporal changes of topological network parameters such as connectivity, shortest path length, edge length. It was shown how RGCs evolve in different stages from a simple network to a system with an optimized architecture. However, networks are further characterized, essentially regarding the network class, by the clustering coefficient C and the so-called small-worldness S. The latter relates the small-world parameters C_{small} and L_{small} to corresponding values for random networks with the same number of vertices and edges and is given by equation 3.4 (Humphries et al., 2008). Small-world networks stand out due to large cluster coefficients compared to random networks ($\overline{C}_{\text{small}} \gg C_{\text{rand}}$), where $C_{\text{rand}} \sim k/n$ with n being the number of vertices in the network and k the degree of a vertex. Additionally, the path length L is much smaller than for regular graphs and similar to values for random graphs, i.e., $L_{\text{reg}} \gg L_{\text{small}} \geq L_{\text{rand}}$ with $L_{\text{reg}} = n/2k$ and $L_{\text{rand}} \sim \ln(n)/\ln(k)$ (Watts and Strogatz, 1998). The clustering coefficient averaged over all 13 RGC networks was determined to be $\overline{C}_{\text{start}} = 0.030 \pm 0.011$ at the beginning of the observation. As expected, when the networks evolved, the clustering coefficient increased to an average value of $\overline{C}_{\text{max/opt}} = 0.095 \pm 0.013$ for both maximum and optimized networks. The errors correspond to the SEM.

It has to be noted that the clustering coefficient is not well-defined for single vertices or vertices with only one neighbor because the denominator becomes zero (cf. equation 3.3). In theses cases, clustering coefficients of corresponding vertices were set to zero. However, this procedure underestimates the clustering coefficient. Therefore, a correction factor f for the clustering coefficient was proposed which then reads as $C' = f \cdot C$ (Kaiser, 2008). The prefactor is defined as $f = \frac{1}{1-\gamma}$, where γ corresponds to the fraction of vertices with zero or one neighbor. Specifying the prefactor f in addition to the clustering coefficient C allows a better evaluation of the network's connectedness (Kaiser, 2008). The influence of isolated vertices was largest for the initial networks, where values of $\overline{f}_{\text{start}} = 3.041 \pm 0.844$ and $\overline{C}'_{\text{start}} = 0.055 \pm 0.019$ were found. For the more connected maximum and optimized networks f decreased to $\overline{f}_{\text{max}} = 1.284 \pm 0.356$ yielding a corrected clustering coefficient $\overline{C}'_{\text{max}} = 0.120 \pm 0.012$ and $\overline{f}_{\text{opt}} = 1.302 \pm 0.361$ which leads to $\overline{C}'_{\text{opt}} = 0.120 \pm 0.015$, respectively.

For the largest network of each of the three cell preparations the path lengths L_{opt} and

the clustering coefficients $\overline{C}_{opt}$ were compared with according values for regular and random networks, respectively, as summarized in table 5.3. Therefore, ten random network graphs were generated using the Brain Connectivity Toolbox (Rubinov and Sporns, 2010) and analyzed as described in section 3.8.3 for the RGC data. All RGC networks exhibited path lengths that were much smaller than those of corresponding regular networks and slightly larger than L_{rand}. The clustering coefficients of RGC networks exceeded the values determined for analog random networks by one order of magnitude. Finally, the small-worldness was found to be much larger than one for all of the three RGC networks. Very similar findings were obtained for maximum networks. Thus, all these properties show that RGC networks also belong to the small-world networks.

n	m	k	L_{reg}	L	L_{rand}	$\overline{C}_{rand}$	$\overline{C}$	f	S
243	350	3	40.5	10	5.1	0.012	0.130	1.085	5.62
203	293	3	33.8	9	4.9	0.013	0.134	1.103	5.72
98	121	2	24.5	7	4.8	0.013	0.189	1.256	9.81

Table 5.3.: Small-world parameters of three optimized *in vitro* RGC networks (n: number of vertices, m: number of edges, k: connectivity, L: path length, $\overline{C}$: normal average clustering coefficient, f: correction factor taking account of scarcely connected cells, S: small-worldness). The path lengths L_{reg} and L_{rand} and the clustering coefficient $\overline{C}_{rand}$ of a regular and random network, respectively, with the same numbers of vertices, edges and connectivity are given for comparison.

5.3. Discussion

Neuronal growth was studied on two levels – on one side the neurite formation of single cells and on the other side the formation of entire networks. The first point shall shed light on the question whether neurons are able to sense mechanical differences in their surroundings, i.e., the substrates they are growing on and if they show an inverse durotaxis. In the second part, it will be discussed how RGC networks evolve towards optimized complex small-world networks and a comparison will be drawn to other neuronal networks.

5.3.1. Lipid bilayer substrates for neuronal growth

Previous studies of neuronal mechanosensitivity *in vitro* were mostly carried out on hydrogels of different compliance (Franze and Guck, 2010). Here, a novel approach was followed – the use of lipid bilayer substrates with tunable fluidity. The viscous drag on anchor molecules for cell adhesion in the lipid bilayer was supposed to act as mechanical stimulus which can be perceived by growing cells. Tethered bilayers were reported to

show a higher lateral mobility than conventional supported bilayers (Tanaka and Sackmann, 2005; Naumann et al., 2002). Moreover, the polymer-linker density essentially influences the membrane fluidity (Deverall et al., 2005). It was shown for different bilayer systems that the diffusion coefficients of tBLs with a polymer-linker concentration of 5 mol% exceed corresponding values at 30 mol% by a factor of approximately three to four (Siegel et al., 2010; Deverall et al., 2008).

To characterize the substrates used in this work, qualitative and quantitative FRAP experiments were performed. The qualitative FRAP experiments showed a faster bleaching of polymer-tethered bilayers at low polymer-linker concentration in contrast to pure POPC supported bilayers. Furthermore, they revealed the existence of substructures within the bilayer for a high polymer concentration (30 mol% $PMOx_{50}$). This finding was also reported for a similar system by (Siegel et al., 2010). Therefore, these substrates were excluded and the mechanosensitive behavior of neurons was solely investigated on pure POPC supported bilayers and tethered bilayers consisting of POPC + 5 mol% $PMOx_{50}$, denoted as sBLs and tBLs in the following. The fluidity of the bilayers was evaluated by means of the diffusion coefficient D. Quantitative FRAP measurements yielded a slightly higher diffusion coefficient for the sBLs, which was in contradiction to my expectations. There are several possible explanations for this finding. Firstly, the radius of the bleaching spot size r was not kept constant for both substrates. As the diffusion coefficient D depends quadratically on r, it makes a direct comparison of the data for sBLs and tBLs difficult. Secondly, the data comprise 6 (sBLs) and 7 (tBLs) sets measured on one and the same bilayer preparation. Thus, on the one side better statistics could have been obtained if more substrates would have been prepared for the FRAP experiments. On the other side, the risk of measuring artifacts or defects in the bilayer could have been minimized. These arguments also hold for the large immobile fractions (30 - 40 %) measured here. In earlier FRAP studies they were reported to be between 3 - 15 % (Guo et al., 2008; Diaz et al., 2008; Kalb et al., 1992). Another plausible reason is that the outer bilayer leaflet was enriched with 5 mol% PEG2000-NHS-linker to promote cell adhesion. These large molecules may cause the increased immobile fractions. However, the diffusion coefficient D_{sBL} measured in this work fits perfectly in the range of earlier results ($1.8\,\mu m^2/s \leq D_{\mathrm{POPC}} \leq 4.5\,\mu m^2/s$) (all at approximately 25 °C) (Guo et al., 2008; Diaz et al., 2008; Kalb et al., 1992).

5.3.2. Mechanosensing of NG108 cells: neurite length and branching

Due to the positive results of the qualitative FRAP experiments, the lipid bilayer systems were used as substrates for neuronal growth. The mechanosensitive response of NG108 cells was analyzed by evaluating the neurite length and branching. For both parameters an ambiguous behavior was reported in earlier studies. Dorsal root ganglion (DRG) cells are presumably the only type of cell which showed a response in the neurite length depending on the substrate stiffness. Norman and Aranda-Espinoza found the longest DRG neurites on the softest PAA gels (870 Pa) used in their study (Norman and Aranda-Espinoza, 2010). Koch and coworkers reported similar results, i.e., a maximal neurite length of DRG cells on PAA gels of intermediate stiffness (1000 Pa) and shortest neurites on soft PAA gels (300 Pa) (Koch et al., 2012). In contrast to these findings for DRG cells, there are several studies where the neurite length was found to be unaffected by a variation of substrate stiffness. These studies include different cell types, among these mixed cortical cultures, PC12 cells, spinal cord neurons, fetal cortical neurons and hippocampal neurons (Koch et al., 2012; Norman and Aranda-Espinoza, 2010; Jiang et al., 2007; Leach et al., 2007; Georges et al., 2006). The same holds true for neurite branching. While primary spinal cord neurons showed an increased branching on softer PAA gels (Flanagan et al., 2002), PC12 cells grew poorly on very soft substrates (7 Pa) and exhibited uniform neurite branching on substrates in the range of 190 - 19 kPa (Leach et al., 2007). DRG cells and hippocampal neurons investigated using a similar range of substrate stiffness (150 - 5 kPa) displayed only a slightly increased neuronal branching on softer substrates (Koch et al., 2012).

In this work, neurite formation of NG108 cells grown on tBL and sBL substrates was quantified after 3 days in culture. In accord with an earlier study on PC12 cells cultured on PAA substrates, the distributions of the maximal neurite length and branches per neurite were neither normally nor exponentially distributed (Leach et al., 2007). Significant differences between tBL and sBL substrates were only detected for the maximal neurite length (Kolmogorov-Smirnov test, $p < 0.001$). Its median on tBLs was found to be 47.28 µm and, thus, slightly higher than the corresponding value on sBLs (42.37 µm) (cf. table 5.1). This trend was not reported for most of the other cell types, where substrate rigidity did not impact the neurite length (see above).

If the neurite extension after 3 days in culture is considered as an outgrowth speed, the NG108 growth on lipid bilayer systems can be compared with other substrates. Estimating the outgrowth speed from the median of the neurite length after an average time of 72 h yields 0.66 µm/h for tBLs and 0.59 µm/h for sBLs, respectively. Zhong and cowork-

ers reported NG108 extension rates on conventional cell culture dishes of approximately 1.46 µm/h after 2 days in culture and a decrease to 0.44 µm/h after 4 days (Zhong et al., 1997). In another study average NG108 neurite lengths of 78 µm after 4 - 6 days were determined which corresponds to outgrowth speeds of 0.54 - 0.81 µm/h (on culture flasks) (Mitchell et al., 2007). Thus, NG108 cells show similar neurite lengths on lipid bilayers and normal culture dishes. However, this finding does not imply that NG108 cells do not feel substrate stiffness. A comparative study of neurons cultured on glass and polydimethylsiloxane (PDMS) substrates of varying stiffness yielded a biphasic response, i.e., DRG cells indeed grew best on glass (70 GPa), but on the PDMS substrates they markedly preferred an intermediate stiffness of only 88 kPa (Cheng et al., 2011).

The branching behavior of NG108 cells was characterized in terms of the number of branches per outgrowth and number of branches per millimeter of neurite. The median of the first was found to be 1 for both substrates. Although the 75 % quartile and 95th percentile were larger for tBLs, the distributions did not show a significant difference for tBLs and sBLs. The second parameter (branches/mm neurite) did not show significant differences neither. The average values of 14.43 ± 2.15 (tBL) and 17.87 ± 2.64 (sBL) are slightly above those reported for PC12 cells (Leach et al., 2007) and clearly exceed the ones measured by the group of Paul Janmey (Flanagan et al., 2002). The large discrepancy can be attributed to the use of primary neurons in the study by Flanagan and coworkers, because these cells have much longer neurites than those of neurons from cell lines. Another point is that in both studies (Leach et al., 2007; Flanagan et al., 2002) it was not specified how the neurite length was measured. Here all neurites were tracked beginning from the soma, i.e., deviations of the absolute numbers of branches/mm neurite may deviate if secondary neurites were measured starting from a branching point.

5.3.3. Mechanosensing of RGCs: neurite extension rates

Since the neurite length was almost not sensitive to changes of the substrate viscosity, further experiments were carried out to examine a potential influence of different extension and retraction rates. The determination of growth rates was achieved using time-lapse video microscopy. Moreover, a more physiological cell system, i.e., primary retinal ganglion cells (RGCs), was studied which has the advantage of exhibiting longer neurites than neurons from cell lines. Firstly, growth speeds were determined as long-term extension over the entire observation time (approximately 18 - 21h) and, secondly, as extension and retraction rates between successive image frames (5 - 6 min) during the first 2 h of observation. The long-term growth speeds of RGCs decreased from initially high values of 15 - 30 µm/h to 1 - 5 µm/h after 12 h. The occurrence of very low outgrowth speeds

after 24 - 48 h of observation was also discussed recently (Weigel et al., 2012). The authors report a strong dependence of the growth velocity on the length of the measurement. Hence, the low RGC long-term speeds after 20 h (i.e., approximately 2 days *in vitro*) are in good agreement with endpoint assays after 24 h and 48 h, where embryonic chicken DRG cells (Stepien et al., 1999), embryonic rat hippocampal neurons (Rajnicek et al., 1997) and rat DRG cells exhibited outgrowth velocities of 2 - 6 µm/h. In contrast, at the early stage of neuronal growth, larger velocities of 20 µm/h were reported for Xenopus spinal cord neurons (Rajnicek, 2006) and even up to 60 µm/h for embryonic chicken DRG cells (Schlosshauer et al., 2003), which is consistent with the findings for RGCs in the present work. Thus, the range of mouse RGC growth velocities are in accordance with existing results reported for other primary neurons from various animals. Nevertheless, an effect of substrate viscosity on the long-term RGC growth was not found. Statistical tests did not yield significant differences at several time points during the measurement. As discussed earlier, it cannot be ruled out whether this is a feature of RGC growth or due to the similarity of sBL and tBL substrates. Despite this insensitivity for RGCs, it has to be mentioned that for hippocampal neurons the axonal extension was highest on soft laminin-coated PAA gels (0.5 - 7.5 kPa) (Kostic et al., 2007).

Long-term measurements of growing neurites or endpoint studies may mask features that take place at shorter time scales (Weigel et al., 2012). Therefore, extension and retraction rates during the first 2 h of observation were determined at higher temporal resolution (5 - 6 min). On both substrates, single RGC neurites showed similar growth dynamics, i.e., extension and retraction rates in the range of $\pm$ 1.5 µm/min. These values are in perfect agreement with previous results on advancing growth cones of rat hippocampal neurons and rat DRG cells which exhibited forward speeds of 0.05 - 1.25 µm/min (retraction events were not specified) (Koch et al., 2012). In another study of rat cortical neurons on PDL or laminin-coated PAA gels extension rates of 0.8 - 1.1 µm/min and retraction rates of between -1.3 µm/min and -1.7 µm/min were measured (Norman and Aranda-Espinoza, 2010). However, in both studies the growth rates were found to be independent of the substrate stiffness. This is in contrast to the RGC growth rates measured in the present work, where the median for tBLs (0.34 ± 0.77 µm/min) exceeded the corresponding value of 0.21 ± 0.66 µm/min for sBLs. The statistical analysis confirmed the significant difference between both substrates (Kolmogorov-Smirnov test, $p < 0.001$).

5.3.4. Do neurons show an inverse durotaxis?

Table 5.4 summarizes the results of the mechanosensitivity experiments for NG108 cells and mouse primary RGCs on tBL and sBL substrates. The growth parameters analyzed

for NG108 cells and RGC did not show drastic differences between tBL and sBL substrates. Nevertheless, slight but significant differences were unveiled for the neurite length of NG108 cells and neurite extension rates of RGCs. It is difficult to judge whether these minor changes were solely caused by the similar fluidities of the substrates as measured by the diffusion coefficients. Other lipid substrates composed of stacks of up to four lipid bilayers yielded more definite results. On the most fluid bilayer type fibroblasts did not show any stress fibers after 20 h in culture (Minner, 2010). Thus, it cannot be dismissed that the small differences in substrate viscosity have a relevant impact on the results obtained in this study.

NG108 cells	primary RGCs
• slightly but significantly longer neurites for NG108 cells on tBLs • no significant differences for the number of branches per outgrowth and the number of branches per millimeter neurite on both substrates	• no significant differences for long-term outgrowth speed on both substrates • significantly higher extension rates on tBLs

Table 5.4.: Mechanosensitive response of neurons investigated in the present work

Anyhow, there are other factors which complicate the interpretation of the current results. It has to be noted that the findings obtained in the study perfectly integrate with the "ambiguous results" from earlier studies on neuronal mechanosensitivity which underline the cell's complex responses on substrates of different rigidity. *First, the choice of parameters matters*. The survival of neurons (Georges et al., 2006), number of neurites (Gunn et al., 2005) or focal adhesions (FAs) linking the cell's cytoskeleton to the ECM (Koch et al., 2012), branching behavior (Flanagan et al., 2002), neurite length (Koch et al., 2012; Norman and Aranda-Espinoza, 2010) or neurite extension rates (Norman and Aranda-Espinoza, 2010; Kostic et al., 2007; Balgude, 2001) are quantities, which have been observed to be subject to change with the substrate stiffness or viscosity. The last two parameters were also found to vary on tBLs and sBLs in this study. I believe that focusing on internal cellular structures such as focal adhesion complexes/point contacts or the cytoskeleton may yield further unequivocal insights in the cells' response to mechanical stimuli. *Second, all these findings strongly depend on the cell type*. Even more strikingly, they can vary between neurons from the CNS and PNS (Koch et al., 2012). Koch *et al.* found that DRGs (PNS) generate much higher traction forces than hippocampal neurons (CNS) which makes sense as they have to travel greater distances outside of the brain. Thus,

higher traction forces improve sensing different substrates outside of the brain and allow enhanced neurite outgrowth speeds by pulling at neurites. The high coupling may protect against external mechanical forces from the surrounding tissues (Koch et al., 2012). Thus, observations from different neuronal cell types cannot be generalized and future studies will be necessary to obtain a unified picture.

The exact mechanisms that govern cellular mechanosensitivity have not been revealed yet (Ladoux and Nicolas, 2012; Moore and Sheetz, 2011; Franze and Guck, 2010). Ongoing research aims at specifying the time and length scales on which cells are able to react on differences in substrate stiffness (Ladoux and Nicolas, 2012; Janmey and Miller, 2011) and molecules or cellular structures that act as mechanosensors. Possible candidates are surface adhesion receptors that trigger gene expression upon mechanical stimulation (Wang et al., 2009), focal adhesions (Pelham and Wang, 1997) and traction forces that have been shown to influence FAs (Balaban et al., 2001), mechanosensitive calcium ion channels (Lo et al., 2000) as well as the contractile acto-myosin apparatus (Trichet et al., 2012; Mitrossilis et al., 2009; Chan and Odde, 2008). However, it can likewise be expected that the microtubule (MT) cytoskeleton also has an impact on the mechanosensing (Franze and Guck, 2010). Recent work gives strong evidence that force generation in neuronal growth cones involves a significant contribution from MTs (Rauch et al., 2013).

Nature is beautiful, colored and particularly complex – not only black and white. In analogy, the question whether neurons do show an inverse durotaxis, i.e., they prefer to grow on soft substrates, cannot be answered with yes or no. The large body of experimental data shows that, in contrast to all other cells, neurons grow exceptionally well on soft substrates. Furthermore, *in vivo* neurons grow along glial cells which provide a soft matrix protecting the neurons from mechanical trauma (Lu et al., 2006). Understanding neuronal mechanosensitivity could have direct implications for the injured nervous system, e.g., new insights about how scar tissues hinders neuronal regeneration (Franze and Guck, 2010) or novel approaches for the design of scaffolds that promote regrowth of nerve cells (Moore and Sheetz, 2011) .

5.3.5. How do retinal ganglion cells develop to optimized networks?

The formation of retinal ganglion cell (RGC) networks on lipid bilayer substrates was monitored between 17 h and 41 h in culture. The outgrowth behavior of RGCs described in section 5.2.1 showed similar features to that of 2D locust frontal ganglion cell (FGC) cultures (Shefi et al., 2002b), however, mouse RGC networks developed faster. While in the present study, mouse RGCs exhibited a maximum complexity after 30 - 36 h *in vitro*,

locust FGCs reached that stage only after 3 days. Furthermore, optimized RGC networks appeared earlier, i.e., between 36 - 41 h *in vitro* in contrast to 4 - 5 days for locust FGCs (Shefi et al., 2002a).

To characterize the single stages during the network formation in more detail, the temporal development of various network parameters was analyzed. From the topological graphs, the number of vertices, connectivity, shortest path length and edge length were determined. The time development of these parameters allowed the definition of networks with a maximum complexity and optimized networks. Going through the individual parameters, for the median of the connectivity an increase from $k = 1$ at the beginning to $k = 3$ for higher developed maximum and optimized networks was observed which is not surprising since neural networks aim for a high degree of connectivity. The path length was highest for maximum networks and decreased as the networks optimized. The edge length simultaneously showed an opposing trend, i.e., for maximum networks, where many short segments were observed, it assumed a minimal value and it increased again upon network optimization.

The distributions of the connectivity, path length and edge length were closer examined at the prominent three stages. The connectivity of maximum and optimized RGC networks ($k = 3$) was higher than the average connectivity of 2.38 reported for locust FGCs (Shefi et al., 2002b). Furthermore, the connectivity distributions in the present study were found to be more symmetric than those reported earlier (Shefi et al., 2002b). In other words, mouse RGC networks show less vertices with a low degree and especially maximum and optimized networks were more connected than locust FGC networks. As mentioned above, the connectivity did not follow a power law, thus, RGC networks are not scale-free (Amaral, 2000). This is in agreement with other studies of (un)directed structural and functional neural networks (Stobb et al., 2012; Perin et al., 2011; Sporns and Zwi, 2004; Shefi et al., 2002b) as well as a graph-theoretic model (Humphries et al., 2006). Another feature of RGC networks is the appearance of high node degrees. They suggest the existence of hubs and are characteristic of complex networks (Bullmore and Sporns, 2009). Hubs were also observed for other neural networks (Downes et al., 2012; Bonifazi et al., 2009; Achard, 2006; Sporns and Zwi, 2004). So-called connector hubs link different network modules and, therefore, play an important role in the (fast) communication through the network (Bullmore and Sporns, 2009).

During the network optimization, a path length decrease from $L_{max} = 10$ to $L_{opt} = 8$ was observed. These results are less than half of the earlier reported values (Shefi et al., 2002b). Thus, mouse RGC networks show significant shorter path lengths than locust FGCs *in vitro*, but are still larger than average path length reported for *C. elegans*, macaque and cat cortex (Boccaletti et al., 2006). The large differences between these data most likely

result from the definition of vertices (Kaiser, 2011). While for macaque and cat cortices the connectivity of whole clusters was analyzed (Kaiser and Hilgetag, 2006), in the case of *C. elegans* single cells were counted as vertices (Watts and Strogatz, 1998). In contrast, for 2D *in vitro* neuronal cultures cell somata and neurite branching points were defined as vertices which can cause larger path lengths (this study and (Shefi et al., 2002b)).

While the path length decreased during the network optimization, this behavior was accompanied by a concurrent increase of the edge length from $d_{\mathrm{max}} = 13.56 \pm 12.87\,\mu\mathrm{m}$ to $d_{\mathrm{opt}} = 17.86 \pm 15.60\,\mu\mathrm{m}$. Despite of the choice of vertices and edges, these findings are consistent with earlier results from *C. elegans*, macaque cortex and structural human brain networks that were shown to favor a minimized path length (i.e., number of processing steps) over an absolute minimum of the wiring length to maintain the high topological complexity of small-world networks (Bassett et al., 2010; Chen, 2006; Kaiser and Hilgetag, 2006).

5.3.6. The small world of RGC networks

Beside the path length, the average clustering coefficient $\overline{C}$ provides further insights on the network class. High clustering coefficients were determined for maximum and optimized networks which clearly exceed comparable values of generated random networks. The results for RGC networks agree very well with locust FGCs *in vitro* networks (Shefi et al., 2002b). Furthermore, they are consistent with results reported for connectivity patterns of *C. elegans* and zebrafish as well as different cortical networks (Stobb et al., 2012; Boccaletti et al., 2006; Watts and Strogatz, 1998). The analysis of the correction factor for the clustering coefficient yielded for maximum and optimized networks approximately $f = 1.3$. This result is larger than the corresponding value for the neuronal network of *C. elegans* (Kaiser, 2008). Hence, mouse RGC networks after 2 days *in vitro* are comparatively less connected, i.e., they possess a larger number of vertices with zero or one neighbor.

The small-worldness S introduced by Humphries and coworkers was between 5.62 and 9.81 for the largest three RGC networks studied (Humphries et al., 2008). For locust FGCs the small-worldness was not specified (Shefi et al., 2002b). However, extraction from their data yielded $2.39 \leq S \leq 4.21$, which is notably smaller than the finding for RGCs. Anyhow, both mouse RGC and locust FGC networks join other neural networks, e.g., of *C. elegans*, macaque cortex or functional cortical networks of the human brain (Humphries et al., 2008; Achard, 2006; Kaiser and Hilgetag, 2006) which all exhibit small-worldness parameters of $S > 1$. Taking all the properties like path length, clustering coefficient and small-worldness together, the results show on the one hand that the studied mouse RGC networks (both maximum and optimized) form part of the family of

neural small-world networks. On the other hand, the time dependence interestingly revealed that first the small-world architecture is established and subsequently optimized for short path lengths.

In conclusion it can be summarized that although the neuronal networks were allowed to form in a random way, the system self-organized to a non-random small-world network. During the early development of RGC networks, different stages were identified which involved the reduction from a network with maximal complexity to an optimized network. At both stages, the networks displayed robust small-world properties. Network optimization was described as a property of small-world systems, but also for spatially constrained networks (Barthélemy, 2011; Bassett et al., 2010). In agreement with earlier results, it was observed that evolving RGC networks do not exclusively strive for a large connectivity, but rather minimize the shortest path length for a high performance in information transmission (Bullmore and Sporns, 2012; Bassett et al., 2010; Chen, 2006; Kaiser and Hilgetag, 2006). Thus, fundamental inherent neuronal properties reveal and govern the RGC outgrowth. These comprise, firstly, the formation of small-world networks which could be defined as the default program for RGCs that are not in their natural environment and, secondly, the ability to optimize the network's architecture.

6. Conclusions and outlook

The biological membrane does not only form the border of a cell but constitutes a platform which is highly involved in the interactions of the cell with its environment. Lipids and proteins as building blocks of the plasma membrane play an important role in processes like signal transduction, permeability and cell adhesion. Another integral part of cells and the extracellular matrix is water which has on the one side a profound influence on the structure of proteins and DNA and on the other side it exhibits itself peculiar properties in the vicinity of biomolecules. Therefore, the first scope of this thesis was to elucidate the properties of confined water at cationic lipid membranes using ATR FTIR spectroscopy. Down to the present day, there is no model that explains all properties of liquid water. Since water is ubiquitous, a large interest persists in unraveling its peculiar properties. Due to the development of new experimental techniques like ultra-fast IR spectroscopy and advancements in computational hardware and models, this is a highly active research field (Berkowitz and Vácha, 2012).

The second part of thesis was dedicated to the behavior of nerve cells being in direct contact with another membrane. First, the growth of single neurons was investigated on lipid bilayers of varying viscosity. These substrates were used as physical guidance cue to gain new insights in the mechanosensitive behavior of neurons. Numerous studies reported that the response of neurons to changes in substrate stiffness varied from that of other cells, which normally prefer to grow on stiff substrates (Lo et al., 2000). Although some key mechanosensing structures have been identified, the reasons for the inverse durotactic behavior of neurons as well as the mechanisms of rigidity sensing have not emerged to a fully understood picture yet (Ladoux and Nicolas, 2012; Moore and Sheetz, 2011). Another aim of this thesis was the study of collective neuronal growth, i.e., the formation of neuronal networks. How neurons self-organize to complex brain networks is of particular interest to understand the development of the nervous system (Salvador et al., 2005). Furthermore, both the growth of single neurons as well as network behavior are linked to medical applications. Developing new substrates to stimulate neuronal outgrowth after injury and altered network properties (disconnected syndromes) related to neural disorders like Alzheimer's disease (Stam and van Straaten, 2012; Bassett and

Bullmore, 2009) are only two examples.

Part 1: Oriented confined water induced by cationic lipids

DODA halides represent a particular membrane system because of their drastic changes in water capacity in dependence on the counterion (F, Cl, Br and I). This has wide implications on the IR spectrum of water adhered to DODAX model membranes. While water adsorptions at DODAI could be hardly detected, one to two water molecules per lipid adhered to DODAC and DODAB multistacks and eleven water molecules to DODAF. Consequently, the OH stretching bands showed striking differences and exhibited clearly visible subbands and shoulders which have not been observed for other lipids such as phospholipids before. At full hydration, the latter adsorb six to thirty water molecules and, therefore, it is more difficult to distinguish between IR spectroscopic signatures of confined and bulk water. In contrast, by adjustment of DODAF hydration to ~ 2 water molecules per lipid, stretching absorptions from water of the first hydration shell were accessible for the fluoride, chloride and bromide analogs.

The polarized measurements demonstrated highly confined and oriented water with IR order parameters ranging from 0.2 to -0.4. Resolved IR water band components were attributed to different H bonded populations. Complementary MD simulations of DODAB strongly supported the existence of differently H bonded and oriented water within DODAB multilayers. The assignment of water stretching band components to structures was achieved by a combination of both techniques and by comparison with previous results from other studies on aqueous salt solutions and small water-halide clusters. In synopsis, the described cationic lipid systems are a prototype for a bottom-up approach to understand the IR spectroscopy of structured water at biological interfaces since they permit a defined increase of hydrophilic water-anionic interactions leading to extended water networks at membranes.

There are several connecting factors for future work on DODAX model membranes. It would be interesting to study the peculiar behavior of water within DODAX with other vibrational spectroscopic techniques like sum frequency generation (SFG) in combination with the utilization of isotopically diluted water. Decoupled OD oscillators (5% D_2O in H_2O) did not give a detectable signal when measured with ATR FTIR spectroscopy and, thus, impeded a systematic study of the water structure. Using pure H_2O and D_2O yields a good signal (cf. section 4.3), but the resulting IR OH/OD stretching spectra are influenced by complex intra- and intermolecular couplings which are difficult to assign (Bakker and Skinner, 2010; Binder, 2003). Therefore, the utilization of newer techniques like SFG spectroscopy provides a powerful tool to gain further insights in lipid/water in-

teractions, as recently shown by Bonn and coworkers who presumably ended the debate whether there is ice-like water near lipid membranes – the answer is "no" (Bonn et al., 2012).

The ordering of water near lipid membranes can also be examined by means of heavy water NMR relaxation measurements. The technique allows the determination of water content within lipid bilayers, water dynamics and the characterization of the physical properties of lipid hydration shells (Arnold et al., 1983; Gawrisch et al., 1992). Arnold and coworkers observed a typical quadrupole splitting of ^{2}H-NMR spectra if lipids were hydrated with D_2O and assorted differently bound water molecules to an inner hydration shell and to partly bound water (Arnold et al., 1983). Gawrisch *et al*. further specified repulsive hydration forces between lipid bilayers (Gawrisch et al., 1992). A common way of accessing the interactions between surfaces such as attractive hydrophobic or Van der Waals forces, repulsive hydration forces, oscillatory or electrostatic forces is the utilization of the surface force apparatus (Israelachvili, 1992; Rand and Parsegian, 1989). The contribution of different surface forces was studied for 1,2-dilauroyl-*sn*-glycero-3-phosphocholine (DLPC) membranes in the presence of various salts (Petrache et al., 2006). The effects observed by using different halide salt solutions (Petrache et al., 2006) indicate that surface forces between DODAX model membranes should also vary significantly.

Another aspect of ongoing research with DODAX model membranes regards the Hofmeister effect (Hofmeister, 1888) because the four counterions belong to the Hofmeister series. The different H bonding strengths, changes of water stretch absorptions and corresponding molecular orientations found in the present work follow the trends predicted by the Hofmeister series (Woiterski et al., 2012). W. Kunz stated recently that "the conclusions made by Hofmeister are far from being trivial" and the origin of the Hofmeister effect is not yet clear. There are many open questions like whether ion-ion interactions play the leading role or ion-water interactions (Kunz, 2010). However, as proven by the work of Petrache and coworkers, salt effects on lipid-water interactions can explain particular Hofmeister effects (Petrache et al., 2006).

Concluding it can be noted that water is an ubiquitous solvent with very remarkable properties which arise from its hydrogen bonding network. It is amazing that, even in the liquid state, water is highly structured.

Part 2: Substrate viscosity as stimulus for neuronal mechanosensitivity

Two neuronal cell types, NG108 cells from a cell line and primary retinal ganglion cells (RGCs), were used to study their response to an altered substrate viscosity. According to previous results regarding the lateral mobility of supported lipid bilayers (sBLs) and

polymer-tethered lipid bilayers (tBLs), the differences in fluidity of these two bilayer systems were expected to be large enough for application as stimulus in neuronal outgrowth (Deverall et al., 2005; Tanaka and Sackmann, 2005; Naumann et al., 2002). While qualitative FRAP experiments still supported this assumption, a quantification of the diffusion in sBLs and tBLs did not yield significant differences (cf. sections 5.1.3 and 5.3.1). In accordance with these results on the substrate properties, neurons cultured on sBLs and tBLs showed only little variations in their outgrowth behavior. In conclusion, it has to be noted that the question whether substrate viscosity can modulate neuronal outgrowth remains open.

Nonetheless, the approach of using viscous substrates as physical stimuli to understand the mechanisms of mechanosensitivity should be further investigated because they constitute a more physiologic model system than substrates with immobilized linkers like hydrogels or micropatterns. One possibility to increase the bilayer fluidity more drastically is the utilization of multiple bilayer stacks (Minner, 2010) which have been briefly introduced in section 2.2.2. However, further studies should address several critical points disregarding the usage of single or multiple bilayers. The first is the occurrence of substrate defects, i.e., it has to be ruled out that cells form anchors through the substrate and connect directly to the solid support. A second aspect concerns the coating with adhesion/ECM molecules (laminin was used in the present thesis and in the work by D. Minner (Minner, 2010)). The lateral mobility of laminin should also be evaluated because cells pull on adhesion molecules to cluster cellular integrins to form point contacts in the case of neurons (McKerracher et al., 1996) or focal adhesions (Geiger et al., 2009).

Additional insights could be obtained by investigating the structural organization of adhesion sites as well as the cytoskeleton, e.g., by appropriate fluorescent staining. A promising result for future work was obtained for fibroblasts on double and quadruple lipid bilayers (Minner, 2010). While on double layers typical actin stress fibers were reported to be replaced by a cortical actin meshwork, on quadrupole layers fibroblasts were found to be highly polarized assuming a spindle-like morphology.

Apart from the substrate quality, also the choice of cell types itself and the parameters which are examined to quantify the mechanosensitive response were found to influence the results of previous studies as discussed in section 5.3.4. Thus, ongoing research will have to address all these points to unravel the mechanisms that govern cellular mechanosensitivity.

In synopsis, although the substrates used in this work did not show the expected differences in fluidity, the approach of modulating cellular mechanosensitivity by altered viscosity should be absolutely pursued. The idea is of great importance because fluidity

is omnipresent in nature.

Part 3: Stages of neuronal network formation

The study of cellular mechanosensitivity focused on the neuronal growth at the level of single cells. Zooming out of this detailed view revealed that cells grew out neurites which connected to neighboring cells and ended up in a large, dynamic neuronal network. The development of RGC networks was characterized by means of time-lapse video microscopy and graph theory. Typical network parameters like clustering coefficient, shortest path length, connectivity and small-worldness were determined (cf. section 5.2). While the topological mapping to graphs of neuronal networks is not new (Bullmore and Sporns, 2009; Watts and Strogatz, 1998), in the present thesis the *temporal evolution of the network parameters* was investigated during the first two days in culture. Surprisingly, different stages were observed during the early network formation. Initially sparsely connected networks developed to networks with a maximum complexity reflected by an increased path length and decreased edge length. In the further course, a simplification of the network was monitored, which manifested in the minimization of the path length. Moreover, RGC networks self-organized as small-world networks at both stages, however, the optimization of the network's architecture occurred only in the second stage.

These results show that despite the simplicity of the model system – a structural *in vitro* 2D neuronal network – new insights about fundamental organizational principles of networks can be derived. The variety of suitable model systems is far from being vast. Only few different species have been characterized: the only entirely mapped neuronal network of *C. elegans* (Watts and Strogatz, 1998), 2D locust frontal ganglion networks (Shefi et al., 2002b), the sensorimotor pathway in zebrafish (Stobb et al., 2012) and among the mammalians different cortical networks of rat (Downes et al., 2012), macaque monkey and cat (Hilgetag et al., 2000) and human brain networks (Stam, 2010; Bullmore and Sporns, 2009). Since progress in neuroscience is tightly connected to computer-based modeling, there is a large demand for corresponding experimental data (van Ooyen, 2011). Thus, neuronal networks from mouse RGCs constitute a novel model system that is suitable to survey theoretical models or to investigate further network properties. This could be in particular the formation of network hubs, the balance of short path length and long edge length which determines the wiring cost (Bassett et al., 2010; Kaiser and Hilgetag, 2006) as well as the exploration of motifs and modularity in RGC networks, which are other features of complex networks and have not been examined yet. Finally, it would be interesting to study the network's response to the removal of vertices or hubs

to illuminate their role in neural diseases (Stam, 2010).

Since scientists are curious, they will not stop until mysteries like the wiring of the brain and the origins of consciousness, intelligence or memory are discovered.

List of Abbreviations

η	Viscosity
λ	Viscous drag coefficient
λ_d	Penetration depth of the evanescent wave
μ	Transition dipole moment
ν	Wavenumber (spectroscopy), Poisson ratio (rheology)
θ_μ	Orientation angle of the transition dipole moment with regard to the normal of the ATR crystal
$A_\parallel$, $A_\perp$	Absorbance measured with parallel and perpendicular polarized light, respectively
C	Clustering coefficient
D	Lateral diffusion coefficient
d	Edge length (neuronal networks), sample thickness (ATR)
E	Electric field strength (spectroscopy), Young's modulus (rheology)
G'	Storage modulus
I	Intensity of the fluorescence signal
IF	Immobile fraction
k	Connectivity or degree of a vertex
K_1, K_2	Optical constants
k_B	Boltzmann constant
L	Path length
n	Refractive index

R	Dichroic ratio
S	Small-worldness
S_{IR}	Infrared order parameter
S_{θ}	Chain order parameter
T_m	Transition temperature
C. elegans	*Caenorhabditis elegans*
A	Acceptor of a hydrogen bond
AgBr	Silver bromide
AgF	Silver fluoride
ATR FTIR	Attenuated total reflection Fourier-transfrom infrared
C_2H_5OH	Ethanol
CCD	Charge-coupled device
CH_3OH	Methanol
$CHCl_3$	Chloroform
CNS	Central nervous system
D	Donor of a hydrogen bond
D_2O	Deuterated water
DLPC	1,2-Dilauroyl-*sn*-glycero-3-phosphocholine
DMPC	1,2-Dimyristoyl-*sn*-glycero-3-phosphocholine
DMSO	Dimethyl sulfoxide
DODAB	Dioctadecyldimethyl ammonium bromide
DODAC	Dioctadecyldimethyl ammonium chloride
DODAF	Dioctadecyldimethyl ammonium fluoride
DODAI	Dioctadecyldimethyl ammonium iodide
DPPC	1,2-dipalmitoyl-*sn*-glycero-3-phosphocholine

DRG	Dorsal root ganglion
DTGS	Deuterated tri-glycine sulfate
ECM	Extra cellular matrix
EDX	Energy dispersive x-ray
FA	Focal adhesion
FBS	Fetal bovine serum
FGC	Frontal ganglion cell
fMRI	Functional magnetic resonance imaging
FRAP	Fluorescence recovery after photobleaching
H_2O	Water
HB (IHB)	(Ionic) Hydrogen bond
HFF	Human foreskin fibroblast
KCl	Potassium chloride
KI	Potassium iodide
LB	Langmuir-Blodgett
LN	Laminin
LS	Langmuir-Schäfer
MAD	Median absolute deviation
MALDI-TOF	Matrix-assisted laser desorption/ionization time of flight
MD	Molecular dynamics
MEA	Muli-electrode array
MSD	Mean square displacement
MT	Microtubule
n	Number of vertices in a network
NBD-PE	*N*-(7-nitrobenz-2-oxa-1,3-diazol-4-yl)-1,2-dihexadecanoyl-*sn*-glycero-3-phosphoethanolamine

NMR	Nuclear magnetic resonance
PAA	Polyacrylamide
PBS	Phosphate buffered saline
PDL (PLL)	Poly-D-lysine (poly-L-lysine)
PDMS	Polydimethylsiloxane
PEG2000-NHS	1,2-distearoyl-*sn*-glycero-3-phosphoethanolamine-*N*-[succinimide ester (polyethylene glycol)-2000]
$PMOx_{50}$	1,2-distearoyl-*sn*-glycerol-poly(2-methyl-2-oxazoline)$_{50}$
PNS	Peripheral nervous system
POPC	1-palmitoyl-2-oleoyl-*sn*-glycero-3-phosphocholine
RGC	Retinal ganglion cell
RH	Relative humidity
SAM	Self-assembled monolayer
sBL	Supported lipid bilayer
SE(M)	Standard error (of the mean)
SOPC	1-stearoyl-2-oleoyl-*sn*-glycero-3-phosphocholine
SPC	Simple point charge
tBL	Tethered lipid bilayer
TR-DHPE	Texas Red®, 1,2-Dihexadecanoyl-*sn*-Glycero-3-Phosphoethanolamine, Triethylammonium Salt
TRITC	Tetramethylrhodamine isothiocyanate
YFP	Yellow fluorescent protein
ZnSe	Zinc selenide

Bibliography

S. Achard. A resilient, low-frequency, small-world human brain functional network with highly connected association cortical hubs. *J. Neurosci.*, 26(1):63–72, 2006.

R. Albert and A. L. Barabási. Statistical mechanics of complex networks. *Rev. Mod. Phys.*, 74(1):47–97, 2002.

B. Alberts. *Molecular Biology of the Cell*. Garland Science, New York, 4 edition, 2002.

D. Alker, L. M. Harwood, and C. E. Williams. Carbamate derived stable precursors for generating chiral azomethine ylids under mild conditions. *Tetrahedron*, 53(37):12671–12678, 1997.

K. Åman, E. Lindahl, O. Edholm, P. Håkansson, and P.-O. Westlund. Structure and dynamics of interfacial water in an Lα phase lipid bilayer from molecular dynamics simulations. *Biophys. J.*, 84(1):102–115, 2003.

L. A. N. Amaral. Classes of small-world networks. *Proc. Natl. Acad. Sci.*, 97(21):11149–11152, 2000.

S. Aoki and Y. Morimoto. Polymerization of amphiphilic quaternary ammonium-salts of acrylic, methacrylic, and ethacrylic acids. *Colloid Polym. Sci.*, 273(8):733–739, 1995.

C. G. Armstrong and V. C. Mow. Variations in the intrinsic mechanical properties of human articular cartilage with age, degeneration, and water content. *J. Bone Joint Surg. Am.*, 64(1):88–94, 1982.

K. Arnold, L. Pratsch, and K. Gawrisch. Effect of poly(ethylene glycol) on phospholipid hydration and polarity of the external phase. *Biochim. Biophys. Acta-Biomembranes*, 728 (1):121–128, 1983.

E. Arunan, G. R. Desiraju, R. A. Klein, J. Sadlej, S. Scheiner, I. Alkorta, D. C. Clary, R. H. Crabtree, J. J. Dannenberg, P. Hobza, H. G. Kjaergaard, A. C. Legon, B. Mennucci, and D. J. Nesbitt. Definition of the hydrogen bond (IUPAC recommendations 2011). *Pure Appl. Chem.*, 83(8):1637–1641, 2011a.

E. Arunan, G. R. Desiraju, R. A. Klein, J. Sadlej, S. Scheiner, I. Alkorta, D. C. Clary, R. H. Crabtree, J. J. Dannenberg, P. Hobza, H. G. Kjaergaard, A. C. Legon, B. Mennucci, and D. J. Nesbitt. Defining the hydrogen bond: An account (IUPAC technical report). *Pure Appl. Chem.*, 83(8):1619–1636, 2011b.

B. M. Auer and J. L. Skinner. Vibrational sum-frequency spectroscopy of the liquid/vapor interface for dilute HOD in D_2O. *J. Chem. Phys.*, 129(21):214705, 2008.

B. M. Auer and J. L. Skinner. Water: Hydrogen bonding and vibrational spectroscopy, in the bulk liquid and at the liquid/vapor interface. *Chem. Phys. Lett.*, 470(1-3):13–20, 2009.

M. Aumailley, L. Bruckner-Tuderman, W. Carter, R. Deutzmann, D. Edgar, P. Ekblom, J. Engel, E. Engvall, E. Hohenester, J. C. R. Jones, H. K. Kleinman, M. P. Marinkovich, G. R. Martin, U. Mayer, G. Meneguzzi, J. H. Miner, K. Miyazaki, M. Patarroyo, M. Paulsson, V. Quaranta, J. R. Sanes, T. Sasaki, K. Sekiguchi, L. M. Sorokin, J. F. Talts, K. Tryggvason, J. Uitto, I. Virtanen, K. von der Mark, U. M. Wewer, Y. Yamada, and P. D. Yurchenco. A simplified laminin nomenclature. *Matrix Biol.*, 24(5):326–332, 2005.

D. Axelrod, D. E. Koppel, J. Schlessinger, E. Elson, and W. W. Webb. Mobility measurement by analysis of fluorescence photobleaching recovery kinetics. *Biophys. J.*, 16(9): 1055–1069, 1976.

P. Ayotte, C. G. Bailey, G. H. Weddle, and M. A. Johnson. Vibrational spectroscopy of small $Br^-\cdot(H_2O)_n$ and $I^-\cdot(H_2O)_n$ clusters: Infrared characterization of the ionic hydrogen bond. *J. Phys. Chem. A*, 102(18):3067–3071, 1998.

P. Ayotte, S. B. Nielsen, G. H. Weddle, M. A. Johnson, and S. S. Xantheas. Spectroscopic observation of ion-induced water dimer dissociation in the $X^-\cdot(H_2O)_2$ (X = F, Cl, Br, I) clusters. *J. Phys. Chem. A*, 103(50):10665–10669, 1999.

H. J. Bakker and J. L. Skinner. Vibrational spectroscopy as a probe of structure and dynamics in liquid water. *Chem. Rev.*, 110(3):1498–1517, 2010.

N. Q. Balaban, U. S. Schwarz, D. Riveline, P. Goichberg, G. Tzur, I. Sabanay, D. Mahalu, S. Safran, A. Bershadsky, L. Addadi, and B. Geiger. Force and focal adhesion assembly: a close relationship studied using elastic micropatterned substrates. *Nat. Cell Biol.*, 3 (5):466–472, 2001.

A. Balgude. Agarose gel stiffness determines rate of DRG neurite extension in 3D cultures. *Biomaterials*, 22(10):1077–1084, 2001.

P. Ball. Water as an active constituent in cell biology. *Chem. Rev.*, 108(1):74–108, 2008a.

P. Ball. Water: Water - an enduring mystery. *Nature*, 452(7185):291–292, 2008b.

P. Ball. Water as a biomolecule. *ChemPhysChem*, 9(18):2677–2685, 2008c.

J. B. Bard. The behavior of fibroblasts from the developing avian cornea. Morphology and movement *in situ* and *in vitro*. *J. Cell Biol.*, 67(2):400–418, 1975.

A. Barth. Infrared spectroscopy of proteins. *Biochim. Biophys. Acta - Bioenergetics*, 1767(9): 1073–1101, 2007.

M. Barthélemy. Betweenness centrality in large complex networks. *Eur. Phys. J. B*, 38(2): 163–168, 2004.

M. Barthélemy. Spatial networks. *Phys. Rep.*, 499(1-3):1–101, 2011.

D. S. Bassett and E. T. Bullmore. Human brain networks in health and disease. *Curr. Opin. Neurol.*, 22(4):340–347, 2009.

D. S. Bassett and M. S. Gazzaniga. Understanding complexity in the human brain. *Trends Cogn. Sci.*, 15(5):200–209, 2011.

D. S. Bassett, E. T. Bullmore, A. Meyer-Lindenberg, J. A. Apud, D. R. Weinberger, and R. Coppola. Cognitive fitness of cost-efficient brain functional networks. *Proc. Natl. Acad. Sci.*, 106(28):11747–11752, 2009.

D. S. Bassett, D. L. Greenfield, A. Meyer-Lindenberg, D. R. Weinberger, S. W. Moore, E. T. Bullmore, and K. J. Friston. Efficient physical embedding of topologically complex information processing networks in brains and computer circuits. *PLoS Comput. Biol.*, 6(4):e1000748, 2010.

M. F. Bear, B. W. Connors, and M. A. Paradiso. *Neuroscience: Exploring the brain*. Lippincott Williams & Wilkins, Philadelphia and PA, 3rd edition, 2007.

B. Bechinger and J. Seelig. Conformational-changes of the phosphatidylcholine headgroup due to membrane dehydration - A ^{2}H-NMR study. *Chem. Phys. Lipids*, 58(1-2): 1–5, 1991.

A. Benda, M. Beneš, V. Mareček, A. Lhotský, W. T. Hermens, and M. Hof. How to determine diffusion coefficients in planar phospholipid systems by confocal fluorescence correlation spectroscopy. *Langmuir*, 19(10):4120–4126, 2003.

K. A. Beningo and Y.-L. Wang. Flexible substrata for the detection of cellular traction forces. *Trends Cell Biol.*, 12(2):79–84, 2002.

H. J. C. Berendsen, J. P. M. Postma, W. F. van Gunsteren, and Hermans J. Interaction model for water in relation to protein hydration. In A. Pullman, editor, *Intermolecular Forces*, volume 14, pages 331–342. D. Reidel Publishing Company, Dordrecht, 1981.

O. Berger, O. Edholm, and F. Jahnig. Molecular dynamics simulations of a fluid bilayer of dipalmitoylphosphatidylcholine at full hydration, constant pressure, and constant temperature. *Biophys. J.*, 72(5):2002–2013, 1997.

P. A. Bergström and J. Lindgren. Infrared study on the hydration of Mn^{2+}, Fe^{2+}, Co^{2+}, La^{3+}, Nd^{3+}, Dy^{3+}, and Yb^{3+} ions in dilute aqueous-solution. *Inorg. Chem.*, 31(8):1529–1533, 1992.

P. A. Bergström, J. Lindgren, and O. Kristiansson. An IR study of the hydration of ClO_4^-, NO_3^-, I^-, Br^-, Cl^-, and SO_4^{2-} anions in aqueous-solution. *J. Phys. Chem.*, 95(22):8575–8580, 1991.

M. L. Berkowitz and R. Vácha. Aqueous solutions at the interface with phospholipid bilayers. *Acc. Chem. Res.*, 45(1):74–82, 2012.

M. L. Berkowitz, D. L. Bostick, and S. Pandit. Aqueous solutions next to phospholipid membrane surfaces: Insights from simulations. *Chem. Rev.*, 106(4):1527–1539, 2006.

A. Bershadsky, M. Kozlov, and B. Geiger. Adhesion-mediated mechanosensitivity: a time to experiment, and a time to theorize. *Curr. Opin. Cell Biol.*, 18(5):472–481, 2006.

A. D. Bershadsky, N. Q. Balaban, and B. Geiger. Adhesion-dependent cell mechanosensitivity. *Annu. Rev. Cell Dev. Biol.*, 19(1):677–695, 2003.

J. E. Bertie, M. K. Ahmed, and Eysel H. H. Infrared intensities of liquids. 5. Optical and dielectric constants, integrated intensities, and dipole moment derivatives of H_2O and D_2O at 22 °C. *J. Phys. Chem.*, 93(6):2210–2218, 1989.

L. Bettencourt, G. Stephens, M. Ham, and G. Gross. Functional structure of cortical neuronal networks grown *in vitro*. *Phys. Rev. E*, 75(2), 2007.

S. Bhattacharya and A. Bajaj. Advances in gene delivery through molecular design of cationic lipids. *Chem. Commun.*, (31):4632, 2009.

K. Bhattacharyya. Nature of biological water: a femtosecond study. *Chem. Commun.*, (25): 2848–2857, 2008.

S. Y. Bhide and M. L. Berkowitz. Structure and dynamics of water at the interface with phospholipid bilayers. *J. Chem. Phys.*, 123(22):224702, 2005.

H. Binder. The molecular architecture of lipid membranes - new insights from hydration-tuning infrared linear dichroism spectroscopy. *Appl. Spectrosc. Rev.*, 38(1):15–69, 2003.

H. Binder. Water near lipid membranes as seen by infrared spectroscopy. *Eur. Biophys. J. Biophys. Lett.*, 36(4-5):265–279, 2007.

H. Binder. *Infrarot-Lineardichroismus molekulargeordneter Systeme - Untersuchungen zur Hydratation und Struktur von Dienlipiden*. Habilitation, Universität Leipzig, Dezember 1999.

H. Binder and W. Pohle. Structural aspects of lyotropic solvation-induced transitions in phosphatidylcholine and phosphatidylethanolamine assemblies revealed by infrared spectroscopy. *J. Phys. Chem. B*, 104(50):12039–12048, 2000.

H. Binder and H. Schmiedel. Infrared dichroism investigations on the acyl chain ordering in lamellar structures: I. Order parameter formalism and its application to polycrystalline stearic acid. *Vib. Spectrosc.*, 21(1-2):51–73, 1999.

M. Bloom and O. G. Mouritsen. Chapter 2: The evolution of membranes. In *Handbook of Biological Physics*, volume 1, pages 65–95. Elsevier Science B. V., Amsterdam, 1995.

S. Boccaletti, V. Latora, Y. Moreno, M. Chavez, and D. Hwang. Complex networks: Structure and dynamics. *Phys. Rep.*, 424(4-5):175–308, 2006.

B. Bollobás. *Modern Graph Theory*. Springer, New York, 1998.

P. Bonifazi, M. Goldin, M. A. Picardo, I. Jorquera, A. Cattani, G. Bianconi, A. Represa, Y. Ben-Ari, and R. Cossart. Gabaergic hub neurons orchestrate synchrony in developing hippocampal networks. *Science*, 326(5958):1419–1424, 2009.

M. Bonn and R. K. Campen. Optical methods for the study of dynamics in biological membrane models. *Surf. Sci.*, 603(10-12):1945–1952, 2009.

M. Bonn, H. J. Bakker, A. Ghosh, S. Yamamoto, M. Sovago, and R. K. Campen. Structural inhomogeneity of interfacial water at lipid monolayers revealed by surface-specific vibrational pump-probe spectroscopy. *J. Am. Chem. Soc.*, 132(42):14971–14978, 2010.

M. Bonn, H. J. Bakker, Y. Tong, and E. H. G. Backus. No ice-like water at aqueous biological interfaces. *Biointerphases*, 7(1-4), 2012.

D. Bray. Mechanical tension produced by nerve cells in tissue culture. *J. Cell Sci.*, 37: 391–410, 1979.

D. Bray. Axonal growth in response to experimentally applied mechanical tension. *Dev. Biol.*, 102(2):379–389, 1984.

D. W. Britt, T. Goodman, and C. Selle. The influence of lipid dipole moment and interfacial water structure on protein adsorption to mixed lipid monolayers. *Materialwiss. Werkstofftech.*, 34(12):1133–1137, 2003.

K. M. Brown, G. Barrionuevo, A. J. Canty, V. Paola, J. A. Hirsch, G. S. X. E. Jefferis, J. Lu, M. Snippe, I. Sugihara, and G. A. Ascoli. The diadem data sets: Representative light microscopy images of neuronal morphology to advance automation of digital reconstructions. *Neuroinformatics*, 9(2-3):143–157, 2011.

J. B. Brubach, A. Mermet, A. Filabozzi, A. Gerschel, and P. Roy. Signatures of the hydrogen bonding in the infrared bands of water. *J. Chem. Phys.*, 122(18), 2005.

V. Buch and J. P. Devlin. A new interpretation of the OH-stretch spectrum of ice. *J. Chem. Phys.*, 110(7):3437–3443, 1999.

E. Bullmore and O. Sporns. Complex brain networks: graph theoretical analysis of structural and functional systems. *Nat. Rev. Neurosci.*, 10(3):186–198, 2009.

E. Bullmore and O. Sporns. The economy of brain network organization. *Nat. Rev. Neurosci.*, 13(5):336–349, 2012.

E. T. Bullmore and D. S. Bassett. Brain graphs: Graphical models of the human brain connectome. *Annu. Rev. Clin. Psychol.*, 7(1):113–140, 2011.

K. Burridge, K. Fath, T. Kelly, G. Nuckolls, and C. Turner. Focal adhesions: Transmembrane junctions between the extracellular matrix and the cytoskeleton. *Annu. Rev. Cell Dev. Biol.*, 4(1):487–525, 1988.

O. M. Cabarcos, C. J. Weinheimer, J. M. Lisy, and S. S. Xantheas. Microscopic hydration of the fluoride anion. *J. Chem. Phys.*, 110(1):5–8, 1999.

H. L. Casal and H. H. Mantsch. Polymorphic phase-behavior of phospholipid-membranes studied by infrared-spectroscopy. *Biochim. Biophys. Acta*, 779(4):381–401, 1984.

E. T. Castellana and P. S. Cremer. Solid supported lipid bilayers: From biophysical studies to sensor design. *Surf. Sci. Rep.*, 61(10):429–444, 2006.

G. Cevc, editor. *Phospholipids Handbook*. Marcel Dekker, Inc., New York, 1993.

C. E. Chan and D. J. Odde. Traction dynamics of filopodia on compliant substrates. *Science*, 322(5908):1687–1691, 2008.

P. Y. Chan, M. B. Lawrence, M. L. Dustin, L. M. Ferguson, D. E. Golan, and T. A. Springer. Influence of receptor lateral mobility on adhesion strengthening between membranes containing LFA-3 and CD2. *J. Cell Biol.*, 115(1):245–255, 1991.

M. Chaplin. Opinion - do we underestimate the importance of water in cell biology? *Nat. Rev. Mol. Cell Biol.*, 7(11):861–866, 2006.

D. Chapman and J. Urbina. Biomembrane phase transitions. studies of lipid-water systems using differential scanning calorimetry. *J. Biol. Chem.*, 249(8):2512–2521, 1974.

B. L. Chen. Wiring optimization can relate neuronal structure and function. *Proc. Natl. Acad. Sci.*, 103(12):4723–4728, 2006.

C.-M. Cheng, P. R. LeDuc, and Y.-W. Lin. Localized bimodal response of neurite extensions and structural proteins in dorsal-root ganglion neurons with controlled polydimethylsiloxane substrate stiffness. *J. Biomech.*, 44(5):856–862, 2011.

J. H. Choi, K. T. Kuwata, Y. B. Cao, and M. Okumura. Vibrational spectroscopy of the $Cl^-(H_2O)_n$ anionic clusters, n = 1 - 5. *J. Phys. Chem. A*, 102(3):503–507, 1998.

S. Chuang. Adjacency matrix gui, 2005. URL `http://www.mathworks.com/matlabcentral/fileexchange/6937-adjacency-matrix-gui`. Retrieved June 05, 2012.

T. Claudepierre, E. Koncina, F. W. Pfrieger, D. Bagnard, D. Aunis, and M. Reber. Implication of neuropilin 2/semaphorin 3F in retinocollicular map formation. *Dev. Dyn.*, 237 (11):3394–3403, 2008.

J. Cocquyt, U. Olsson, G. Olofsson, and P. van der Meeren. Temperature quenched DODAB dispersions: Fluid and solid state coexistence and complex formation with oppositely charged surfactant. *Langmuir*, 20(10):3906–3912, 2004.

J. Cocquyt, U. Olsson, G. Ofsson, and P. van der Meeren. Thermal transitions of DODAB vesicular dispersions. *Colloid Polym. Sci.*, 283(12):1376–1381, 2005.

J. Cohen and A. R. Johnson. Differential effects of laminin and merosin on neurite outgrowth by developing retinal ganglion cells. *J. Cell Sci. Suppl.*, 15:1–7, 1991.

W. D. Comper and T. C. Laurent. Physiological function of connective tissue polysaccharides. *Physiol. Rev.*, 58(1):255–315, 1978.

P. S. Cremer and S. G. Boxer. Formation and spreading of lipid bilayers on planar glass supports. *J. Phys. Chem. B*, 103(13):2554–2559, 1999.

E. Cukierman, R. Pankov, D. R. Stevens, and K. M. Yamada. Taking cell-matrix adhesions to the third dimension. *Science*, 294(5547):1708–1712, 2001.

H. Cuntz, F. Forstner, A. Borst, M. Häusser, and A. Morrison. One rule to grow them all: A general theory of neuronal branching and its practical application. *PLoS Comput. Biol.*, 6(8):e1000877, 2010.

M. A. Deverall, E. Gindl, E.-K Sinner, H. Besir, J. Ruehe, M. J. Saxton, and C. A. Naumann. Membrane lateral mobility obstructed by polymer-tethered lipids studied at the single molecule level. *Biophys. J.*, 88(3):1875–1886, 2005.

M. A. Deverall, S. Garg, K. Lüdtke, R. Jordan, J. Rühe, and C. A. Naumann. Transbilayer coupling of obstructed lipid diffusion in polymer-tethered phospholipid bilayers. *Soft Matter*, 4(9):1899, 2008.

A. J. Diaz, F. Albertorio, S. Daniel, and P. S. Cremer. Double cushions preserve transmembrane protein mobility in supported bilayer systems. *Langmuir*, 24(13):6820–6826, 2008.

E. A. Disalvo, F. Lairion, F. Martini, E. Tymczyszyn, M. Frias, H. Almaleck, and G. J. Gordillo. Structural and functional properties of hydration and confined water in membrane interfaces. *Biochim. Biophys. Acta-Biomembranes*, 1778(12):2655–2670, 2008.

D. E. Discher, P. Janmey, and Y. L. Wang. Tissue cells feel and respond to the stiffness of their substrate. *Science*, 310(5751):1139–1143, 2005.

S. N. Dorogovtsev and J. F. F. Mendes. Evolution of networks. *Adv. Phys.*, 51(4):1079–1187, 2002.

J. H. Downes, M. W. Hammond, D. Xydas, M. C. Spencer, V. M. Becerra, K. Warwick, B. J. Whalley, S. J. Nasuto, and O. Sporns. Emergence of a small-world functional network in cultured neurons. *PLoS Comput. Biol.*, 8(5):e1002522, 2012.

A. Eftekhari-Bafrooei and E. Borguet. Effect of hydrogen-bond strength on the vibrational relaxation of interfacial water. *J. Am. Chem. Soc.*, 132(11):3756–3761, 2010.

V. M. Eguíluz, D. R. Chialvo, G. A. Cecchi, M. Baliki, and A. V. Apkarian. Scale-free brain functional networks. *Phys. Rev. Lett.*, 94(1), 2005.

A. J. Engler, S. Sen, H. L. Sweeney, and D. E. Discher. Matrix elasticity directs stem cell lineage specification. *Cell*, 126(4):677–689, 2006.

E. Evans and E. Sackmann. Translational and rotational drag coefficients for a disk moving in a liquid membrane associated with a rigid substrate. *J. Fluid Mech.*, 194(-1): 553–561, 1988.

D. A. Fair, A. L. Cohen, J. D. Power, N. U. F. Dosenbach, J. A. Church, F. M. Miezin, B. L. Schlaggar, S. E. Petersen, and O. Sporns. Functional brain networks develop from a "local to distributed" organization. *PLoS Comp. Biol.*, 5(5):e1000381, 2009.

D. Falconnet, G. Csucs, H. Michelle Grandin, and M. Textor. Surface engineering approaches to micropattern surfaces for cell-based assays. *Biomaterials*, 27(16):3044–3063, 2006.

Z. Fanti, F. F. De-Miguel, and M. E. Martinez-Perez. A method for semiautomatic tracing and morphological measuring of neurite outgrowth from dic sequences. In *Annual International Conference of the IEEE Engineering in Medicine and Biology Society*, pages 1196–1199, Piscataway, 2008.

Z. Fanti, M. E. Martinez-Perez, and F. F. De-Miguel. Neurongrowth, a software for automatic quantification of neurite and filopodial dynamics from time-lapse sequences of digital images. *Dev. Neurobiol.*, 71(10):870–881, 2011.

E. Feitosa, P. C. A. Barreleiro, and G. Olofsson. Phase transition in dioctadecyldimethylammonium bromide and chloride vesicles prepared by different methods. *Chem. Phys. Lipids*, 105(2):201–213, 2000.

P. L. Felgner, T. R. Gadek, M. Holm, R. Roman, H. W. Chan, M. Wenz, J. P. Northrop, G. M. Ringold, and M. Danielsen. Lipofection - a highly efficient, lipid-mediated dna-transfection procedure. *Proc. Natl. Acad. Sci. U. S. A.*, 84(21):7413–7417, 1987.

L. A. Flanagan, Y. E. Ju, B. Marg, M. Osterfield, and P. A. Janmey. Neurite branching on deformable substrates. *NeuroReport*, 13(18):2411–2415, 2002.

F. Franks. *Water: A Comprehensive Treatise. Vol. 1: The Physics and Physical Chemistry of Water*. Plenum Press, New York and N.Y., 1972.

K. Franze and J. Guck. The biophysics of neuronal growth. *Rep. Prog. Phys.*, 73(9):094601, 2010.

L. C. Freeman. A set of measures of centrality based on betweenness. *Sociometry*, 40(1): 35, 1977.

U. P. Fringeli and H. H. Günthard. Infrared membrane spectroscopy. *Mol. Biol., Biochem. Biophys.*, 31(31):270–332, 1981.

U. P. Fringeli, W. Gasche, Leuzinge.W, H. H. Gunthard, and H. G. Muldner. Structure of lipids and proteins studied by attenuated total-reflection (ATR) infrared spectroscopy. 1. Oriented layers of tripalmitin. *Z. Naturforsch., B: Anorg. Chem., Org. Chem., Biochem., Biophys., Biol.*, B 27(7):780, 1972.

D. R. Gauger, C. Selle, M. Hahn, and W. Pohle. Defining the water content in oriented lipid–films by Karl–Fischer titration. *Anal. Biochem.*, 299:108–110, 2001.

K. Gawrisch, D. Ruston, J. Zimmerberg, V. A. Parsegian, R. P. Rand, and N. Fuller. Membrane dipole potentials, hydration forces, and the ordering of water at membrane surfaces. *Biophys. J.*, 61(5):1213–1223, 1992.

B. Geiger, J. P. Spatz, and A. D. Bershadsky. Environmental sensing through focal adhesions. *Nat. Rev. Mol. Cell Biol.*, 10(1):21–33, 2009.

P. C. Georges, W. J. Miller, D. F. Meaney, E. S. Sawyer, and P. A. Janmey. Matrices with compliance comparable to that of brain tissue select neuronal over glial growth in mixed cortical cultures. *Biophys. J.*, 90(8):3012–3018, 2006.

M. Ghibaudo, A. Saez, L. Trichet, A. Xayaphoummine, J. Browaeys, P. Silberzan, A. Buguin, and B. Ladoux. Traction forces and rigidity sensing regulate cell functions. *Soft Matter*, 4(9):1836, 2008.

M. Girvan and M. E. J. Newman. Community structure in social and biological networks. *Proc. Natl. Acad. Sci.*, 99(12):7821–7826, 2002.

D. F. Gleich. gaimc : Graph algorithms in matlab code: clustercoeffs, 2009. URL `http://www.mathworks.com/matlabcentral/fileexchange/24134`. Retrieved April 26, 2012.

E. Goormaghtigh, V. Raussens, and J. M. Ruysschaert. Attenuated total reflection infrared spectroscopy of proteins and lipids in biological membranes. *Biochim. Biophys. Acta, Rev. Biomembr.*, 1422(2):105–185, 1999.

J. Gradolnik, J. Kidric, and D. Hadzi. Hydration of phosphatidylcholine reverse micelles and multilayers - an infrared spectroscopic study. *Chem. Phys. Lipids*, 59(1):57–68, 1991.

A. Grakoui, S. K. Bromley, C. Sumen, M. M. Davis, A. S. Shaw, P. M. Allen, and Dustin M. L. The immunological synapse: A molecular machine controlling T cell activation. *Science*, 285(5425):221–227, 1999.

J. T. Groves and M. L. Dustin. Supported planar bilayers in studies on immune cell adhesion and communication. *J. Immunol. Methods*, 278(1-2):19–32, 2003.

J. T. Groves, L. K. Mahal, and C. R. Bertozzi. Control of cell adhesion and growth with micropatterned supported lipid membranes. *Langmuir*, 17(17):5129–5133, 2001.

B. M. Gumbiner. Cell adhesion: The molecular basis of tissue architecture and morphogenesis. *Cell*, 84(3):345–357, 1996.

J. W. Gunn, S. D. Turner, and B. K. Mann. Adhesive and mechanical properties of hydrogels influence neurite extension. *J. Biomed. Mater. Res.*, 72(1):91–97, 2005.

B. Guo and W. H. Guilford. Mechanics of actomyosin bonds in different nucleotide states are tuned to muscle contraction. *Proc. Natl. Acad. Sci.*, 103(26):9844–9849, 2006.

L. Guo, J. Y. Har, J. Sankaran, Y. Hong, B. Kannan, and T. Wohland. Molecular diffusion measurement in lipid bilayers over wide concentration ranges: A comparative study. *ChemPhysChem*, 9(5):721–728, 2008.

W.-H. Guo, M. T. Frey, N. A. Burnham, and Y.-L. Wang. Substrate rigidity regulates the formation and maintenance of tissues. *Biophys. J.*, 90(6):2213–2220, 2006.

B. Hamprecht, T. Glaser, G. Reiser, E. Bayer, and F. Propst. Culture and characteristics of hormone-responsive neuroblastoma X glioma hybrid cells. In Lutz Birnbaumer and Bert W. O'Malley, editors, *Methods in Enzymology*, volume 109, pages 316–341. Academic, New York, 1985.

N. J. Harrick. *Internal reflection spectroscopy*. Harrick Scientific Corp., Ossining and N.Y, 1987.

E. D. Hay. Interaction of embryonic cell surface and cytoskeleton with extracellular matrix. *Am. J. Anat.*, 165(1):1–12, 1982.

Y. He, Z. J. Chen, and A. C. Evans. Small-world anatomical networks in the human brain revealed by cortical thickness from MRI. *Cereb. Cortex*, 17(10):2407–2419, 2006.

C. C. Hilgetag and M. Kaiser. Clustered organization of cortical connectivity. *Neuroinformatics*, 2(3):353–360, 2004.

C. C. Hilgetag, G. A. P. C. Burns, M. A. O'Neill, J. W. Scannell, and M. P. Young. Anatomical connectivity defines the organization of clusters of cortical areas in the macaque and the cat. *Philos. Trans. R. Soc. B: Biol. Sci.*, 355(1393):91–110, 2000.

F. Hofmeister. Zur Lehre von der Wirkung der Salze. [Title translation: About the science of the effect of salts.]. *Arch. Exp. Pathol. Pharmakol.*, 24(24):247–260, 1888.

C. J. Honey, O. Sporns, L. Cammoun, X. Gigandet, J. P. Thiran, R. Meuli, and P. Hagmann. Predicting human resting-state functional connectivity from structural connectivity. *Proc. Natl. Acad. Sci.*, 106(6):2035–2040, 2009.

C. J. Honey, J. P. Thivierge, and O. Sporns. Can structure predict function in the human brain? Computational models of the brain. *NeuroImage*, 52(3):766–776, 2010.

S. M. H. Hosseini, F. Hoeft, S. R. Kesler, and R. Lambiotte. GAT: A graph-theoretical analysis toolbox for analyzing between-group differences in large-scale structural and functional brain networks. *PLoS ONE*, 7(7):e40709, 2012.

W. Hübner and A. Blume. Interactions at the lipid-water interface. *Chem. Phys. Lipids*, 96 (1-2):99–123, 1998.

M. D. Humphries, K. Gurney, and T. J. Prescott. The brainstem reticular formation is a small-world, not scale-free, network. *Proc. Roy. Soc. B: Biol. Sci.*, 273(1585):503–511, 2006.

M. D. Humphries, K. Gurney, and O. Sporns. Network 'small-world-ness': A quantitative method for determining canonical network equivalence. *PLoS ONE*, 3(4):e0002051, 2008.

R. Ionov and A. Angelova. Swelling of bilayer lipid membranes. *Thin Solid Films*, 284-285 (284-285):809–812, 1996.

J. N. Israelachvili. *Intermolecular and Surface Forces*. Academic Press Limited, London, 1992.

J. N. Israelachvili, D. J. Mitchell, and B. W. Ninham. Theory of self-assembly of hydrocarbon amphiphiles into micelles and bilayers. *J. Chem. Soc., Faraday Trans. 2*, 72:1525, 1976.

M. J. Janiak, D. M. Small, and G. G. Shipley. Nature of thermal pre-transition of synthetic phospholipids: Dimyristoyllecithin and dipalmitoyllecithin. *Biochemistry*, 15(21):4575–4580, 1976.

P. A. Janmey and R. T. Miller. Mechanisms of mechanical signaling in development and disease. *J. Cell Sci.*, 124(1):9–18, 2011.

P. A. Janmey, J. P. Winer, M. E. Murray, and Q. Wen. The hard life of soft cells. *Cell Motil. Cytoskeleton*, 66(8):597–605, 2009.

X. Jiang, P. C. Georges, B. Li, Y. Du, M. K. Kutzing, Michelle L. Previtera, N. A. Langrana, and B. L. Firestein. Cell growth in response to mechanical stiffness is affected by neuron-astroglia interactions. *Open Neurosci. J.*, 1:7–14, 2007.

S.J Johnson, T. M. Bayerl, D.C McDermott, G.W Adam, A.R Rennie, R.K Thomas, and E. Sackmann. Structure of an adsorbed dimyristoylphosphatidylcholine bilayer measured with specular reflection of neutrons. *Biophys. J.*, 59(2):289–294, 1991.

R. Jordan, K. Martin, H. J. Räder, and K. K. Unger. Lipopolymers for surface functionalizations. 1. Synthesis and characterization of terminal functionalized poly(N-propionylethylenimine)s. *Macromolecules*, 34(26):8858–8865, 2001.

M. Kaiser. Mean clustering coefficients: the role of isolated nodes and leafs on clustering measures for small-world networks. *New J. Phys.*, 10(8):083042, 2008.

M. Kaiser. A tutorial in connectome analysis: Topological and spatial features of brain networks. *NeuroImage*, 57(3):892–907, 2011.

M. Kaiser and C. C. Hilgetag. Nonoptimal component placement, but short processing paths, due to long-distance projections in neural systems. *PLoS Comp. Biol.*, 2(7):805–815, 2006.

E. Kalb, S. Frey, and L. K. Tamm. Formation of supported planar bilayers by fusion of vesicles to supported phospholipid monolayers. *Biochim. Biophys. Acta*, 1103(2):307–316, 1992.

T. Kawai, J. Umemura, T. Takenaka, M. Kodama, Y. Ogawa, and S. Seki. Polarized fourier-transform infrared-spectra and molecular-orientation of a water dioctadecyldimethylammonium chloride system in the coagel and gel phases. *Langmuir*, 2(6):739–743, 1986.

V. Kiessling, J. M. Crane, and L. K. Tamm. Transbilayer effects of raft-like lipid domains in asymmetric planar bilayers measured by single molecule tracking. *Biophysical Journal*, 91(9):3313–3326, 2006.

I.-J. Kim, Y. Zhang, M. Meister, and J. R. Sanes. Laminar restriction of retinal ganglion cell dendrites and axons: Subtype-specific developmental patterns revealed with transgenic markers. *J. Neurosci.*, 30(4):1452–1462, 2010.

S. Kint, P. H. Wermer, and J. R. Scherer. Raman-spectra of hydrated phospholipid-bilayers. 2. Water and headgroup interactions. *J. Phys. Chem.*, 96(1):446–452, 1992.

M. Kleder. Allspath, 2005. URL `http://www.mathworks.com/matlabcentral/fileexchange/8808-all-pairs-shortest-path-graph-solver`. Retrieved April 03, 2012.

T. Kobayashi and M. Sokabe. Sensing substrate rigidity by mechanosensitive ion channels with stress fibers and focal adhesions. *Curr. Opin. Cell Biol.*, 22(5):669–676, 2010.

D. Koch, W. J. Rosoff, J. Jiang, H. M. Geller, and J. S. Urbach. Strength in the periphery: Growth cone biomechanics and substrate rigidity response in peripheral and central nervous system neurons. *Biophys. J.*, 102(3):452–460, 2012.

T. Köchy and T. M. Bayerl. Lateral diffusion coefficients of phospholipids in spherical bilayers on a solid support measured by ^{2}H-nuclear-magnetic-resonance relaxation. *Phys. Rev. E*, 47(3):2109–2116, 1993.

F. Kong, A. J. Garcia, A. P. Mould, M. J. Humphries, and C. Zhu. Demonstration of catch bonds between an integrin and its ligand. *J. Cell Biol.*, 185(7):1275–1284, 2009.

A. Kostic, J. Sap, and M. P. Sheetz. RPTP is required for rigidity-dependent inhibition of extension and differentiation of hippocampal neurons. *J. Cell Sci.*, 120(21):3895–3904, 2007.

T. Kunitake, Y. Okahata, K. Tamaki, F. Kumamaru, and M. Takayanagi. Formation of bilayer membrane from a series of quaternary ammonium-salts. *Chem. Lett.*, (4):387–390, 1977.

W. Kunz. Specific ion effects in colloidal and biological systems. *Curr. Opin. Colloid Interface Sci.*, 15(1-2):34–39, 2010.

B. Ladoux and A. Nicolas. Physically based principles of cell adhesion mechanosensitivity in tissues. *Rep. Prog. Phys.*, 75(11):116601, 2012.

S. E. LaFlamme, S. K. Akiyama, and K. M. Yamada. Regulation of fibronectin receptor distribution. *J. Cell Biol.*, 117(2):437–447, 1992.

L. Lago-Fernández, R. Huerta, F. Corbacho, and J. Sigüenza. Fast response and temporal coherent oscillations in small-world networks. *Phys. Rev. Lett.*, 84(12):2758–2761, 2000.

G. Lamoureux and B. Roux. Absolute hydration free energy scale for alkali and halide ions established from simulations with a polarizable force field. *J. Phys. Chem. B*, 110 (7):3308–3322, 2006.

S. E. Lappi, B. Smith, and S. Franzen. Infrared spectra of $H_2{}^{16}O$, $H_2{}^{18}O$ and D_2O in the liquid phase by single-pass attenuated total internal reflection spectroscopy. *Spectrochim. Acta, Part A*, 60(11):2611–2619, 2004.

R. G. Laughlin, R. L. Munyon, Y. C. Fu, and A. J. Fehl. Physical science of the dioctadecyldimethylammonium chloride water-system. 1. Equilibrium phase-behavior. *J. Phys. Chem.*, 94(6):2546–2552, 1990.

J. Le Digabel, M. Ghibaudo, L. Trichet, A. Richert, and B. Ladoux. Microfabricated substrates as a tool to study cell mechanotransduction. *Med. Biol. Eng. Comput.*, 48(10): 965–976, 2010.

J. B. Leach, X. Q. Brown, J. G. Jacot, P. A. DiMilla, and J. Y. Wong. Neurite outgrowth and branching of PC12 cells on very soft substrates sharply decreases below a threshold of substrate rigidity. *J. Neural Eng.*, 4(2):26–34, 2007.

J. Lee, M. Leonard, T. Oliver, A. Ishihara, and K. Jacobson. Traction forces generated by locomoting keratocytes. *J. Cell Biol.*, 127(6 Pt 2):1957–1964, 1994.

R. N. A. H. Lewis and R. N. McElhaney. Fourier transform infrared spectroscopy in the study of lipid phase transitions in model and biological membranes: practical considerations. In A. Dopico, editor, *Methods in Membrane Lipids*, volume 400 of *Methods in Molecular Biology*, pages 207–226. Humana Press Inc., Totowa and NJ, 2007.

D. F. Liu, G. Ma, L. M. Levering, and H. C. Allen. Vibrational spectroscopy of aqueous sodium halide solutions and air-liquid interfaces: Observation of increased interfacial depth. *J. Phys. Chem. B*, 108(7):2252–2260, 2004.

C.-M. Lo, H.-B. Wang, M. Dembo, and Y.-L. Wang. Cell movement is guided by the rigidity of the substrate. *Biophys. J.*, 79(1):144–152, 2000.

H. F. Lodish. *Molecular cell biology*. W.H. Freeman, New York, 4 edition, 2000.

C. F. Lopez, S. O. Nielsen, M. L. Klein, and P. B. Moore. Hydrogen bonding structure and dynamics of water at the dimyristoylphosphatidylcholine lipid bilayer surface from a molecular dynamics simulation. *J. Phys. Chem. B*, 108(21):6603–6610, 2004.

L. A. Lowery and D. van Vactor. The trip of the tip: understanding the growth cone machinery. *Nat. Rev. Mol. Cell Biol.*, 10(5):332–343, 2009.

Y.-B. Lu, K. Franze, G. Seifert, C. Steinhauser, F. Kirchhoff, H. Wolburg, J. Guck, P. Janmey, E.-Q Wei, J. Kas, and A. Reichenbach. Viscoelastic properties of individual glial cells and neurons in the CNS. *Proc. Natl. Acad. Sci.*, 103(47):17759–17764, 2006.

S. E. Lux. Dissecting the red cell membrane skeleton. *Nature*, 281(5731):426–429, 1979.

V. Luzzati and F. Husson. The structure of the liquid-crystalline phases of lipid-water systems. *J. Cell Biol.*, 12(2):207–219, 1962.

V. Luzzati, T. Gulik-Krzywicki, and A. Tardieu. Polymorphism of lecithins. *Nature*, 218 (5146):1031–1034, 1968.

G. Maheshwari, G. Brown, D. A. Lauffenburger, A. Wells, and L. G. Griffith. Cell adhesion and motility depend on nanoscale RGD clustering. *J. Cell Sci.*, 113(10):1677–1686, 2000.

H. H. Mantsch and R. N. McElhaney. Phospholipid phase-transitions in model and biological-membranes as studied by infrared-spectroscopy. *Chem. Phys. Lipids*, 57(2-3):213–226, 1991.

S. J. Marrink, M. Berkowitz, and H. J. C. Berendsen. Molecular dynamics simulation of a membrane/water interface: the ordering of water and its relation to the hydration force. *Langmuir*, 9(11):3122–3131, 1993.

D. Marsh. *CRC Handbook of Lipid Bilayers*. CRC Press, Boca Raton, FL, 1990.

H. M. McConnell, T. H. Watts, R. M. Weis, and A. A. Brian. Supported planar membranes in studies of cell-cell recognition in the immune system. *Biochim. Biophys. Acta, Rev. Biomembr.*, 864(1):95–106, 1986.

L. McKerracher, M. Chamoux, and C. O. Arregui. Role of laminin and integrin interactions in growth cone guidance. *Mol. Neurobiol.*, 12(2):95–116, 1996.

E. Meijering, M. Jacob, J.-C. F. Sarria, P. Steiner, H. Hirling, and M. Unser. Design and validation of a tool for neurite tracing and analysis in fluorescence microscopy images. *Cytometry*, 58(2):167–176, 2004.

P. Mentré. Water in the orchestration of the cell machinery. Some misunderstandings: a short review. *J. Biol. Phys.*, 38(1):13–26, 2012.

R. Merkel, E. Sackmann, and E. Evans. Molecular friction and epitactic coupling between monolayers in supported bilayers. *J. Phys. France*, 50(12):1535–1555, 1989.

D. Meunier, S. Achard, A. Morcom, and E. Bullmore. Age-related changes in modular organization of human brain functional networks. *NeuroImage*, 44(3):715–723, 2009.

J. Milhaud. New insights into water-phospholipid model membrane interactions. *Biochim. Biophys. Acta-Biomembranes*, 1663(1-2):19–51, 2004.

D. E. Minner. *Design of Biomembrane-Mimicking Substrates of Tunable Viscosity to Regulate Cellular Mechanoresponse*. PhD thesis, Purdue University, Indianapolis (IN), 2010. (30.11.2010).

F. M. Mirabella and N. J. Harrick. *Internal reflection spectroscopy: Review and supplement*. Harrick Scientific Corp., Ossining and NY, 1985.

P. J. Mitchell, J. C. Hanson, A. T. Quets-Nguyen, M. Bergeron, and R. C. Smith. A quantitative method for analysis of *in vitro* neurite outgrowth. *J. Neurosci. Methods*, 164(2): 350–362, 2007.

T. Mitchison and M. Kirschner. Cytoskeletal dynamics and nerve growth. *Neuron*, 1(9): 761–772, 1988.

D. Mitrossilis, J. Fouchard, A. Guiroy, N. Desprat, N. Rodriguez, B. Fabry, and A. Asnacios. Single-cell response to stiffness exhibits muscle-like behavior. *Proc. Natl. Acad. Sci.*, 106(43):18243–18248, 2009.

S. W. Moore and M. P. Sheetz. Biophysics of substrate interaction: Influence on neural motility, differentiation, and repair. *Dev. Neurobiol.*, 71(11):1090–1101, 2011.

S. W. Moore, P. Roca-Cusachs, and M. P. Sheetz. Stretchy proteins on stretchy substrates: The important elements of integrin-mediated rigidity sensing. *Dev. Cell*, 19(2):194–206, 2010.

N. Morissette and S. Carbonetto. Laminin α2 chain (M chain) is found within the pathway of avian and murine retinal projections. *J. Neurosci.*, 15(12):8067–8082, 1995.

O. G. Mouritsen. *Life - as a matter of fat: The emerging science of lipidomics*. Frontiers collection. Springer, Berlin, 2005.

D. A. Myrzakozha, T. Hasegawa, J. Nishijo, T. Imae, and Y. Ozaki. An infrared study of molecular orientation and structure in one-layer Langmuir-Blodgett films of octadecyldimethylamine oxide and dioctadecyldimethylammonium chloride: Dependence of the structures of the Langmuir-Blodgett films on substrates, aging, and pH of water subphase. *Langmuir*, 15(20):6890–6896, 1999.

J. F. Nagle and S. Tristram-Nagle. Structure of lipid bilayers. *Biochim. Biophys. Acta, Rev. Biomembr.*, 1469(3):159–195, 2000.

T. Nakamura, F. G. Hillary, B. B. Biswal, and O. Sporns. Resting network plasticity following brain injury. *PLoS ONE*, 4(12):e8220, 2009.

C. A. Naumann, O. Prucker, T. Lehmann, J. Rühe, W. Knoll, and C. W. Frank. The polymer-supported phospholipid bilayer: Tethering as a new approach to substrate−membrane stabilization. *Biomacromolecules*, 3(1):27–35, 2002.

M. E. J. Newman. The structure and function of complex networks. *SIAM Rev.*, 45(2): 167–256, 2003.

Z. S. Nickolov and J. D. Miller. Water structure in aqueous solutions of alkali halide salts: Ftir spectroscopy of the od stretching band. *J. Colloid Interface Sci.*, 287(2):572–580, 2005.

L. L. Norman and H. Aranda-Espinoza. Cortical neuron outgrowth is insensitive to substrate stiffness. *Cell. Mol. Bioeng.*, 3(4):398–414, 2010.

E. Okamura, J. Umemura, and T. Takenaka. Orientation studies of hydrated dipalmitoylphosphatidylcholine multibilayers by polarized FTIR-ATR spectroscopy. *Biochim. Biophys. Acta - Biomembranes*, 1025(1):94–98, 1990.

K. Okuyama, Y. Soboi, N. Iijima, K. Hirabayashi, T. Kunitake, and T. Kajiyama. Molecular and crystal-structure of the lipid-model amphiphile, dioctadecyldimethylammonium bromide monohydrate. *B. Chem. Soc. Jpn.*, 61(5):1485–1490, 1988.

F. Paesani and G. A. Voth. The properties of water: Insights from quantum simulations. *J. Phys. Chem. B*, 113(17):5702–5719, 2009.

F. Paesani, S. S. Xantheas, and G. A. Voth. Infrared spectroscopy and hydrogen-bond dynamics of liquid water from centroid molecular dynamics with an *Ab Initio*-based force field. *J. Phys. Chem. B*, 113(39):13118–13130, 2009.

M. PasenkiewiczGierula, Y. Takaoka, H. Miyagawa, K. Kitamura, and A. Kusumi. Hydrogen bonding of water to phosphatidylcholine in the membrane as studied by a molecular dynamics simulation: Location, geometry, and lipid-lipid bridging via hydrogen-bonded water. *J. Phys. Chem. A*, 101(20):3677–3691, 1997.

R. J. Pelham and Y.-L. Wang. Cell locomotion and focal adhesions are regulated by substrate flexibility. *Proc. Natl. Acad. Sci.*, 94(25):13661–13665, 1997.

R. Perin, T. K. Berger, and H. Markram. A synaptic organizing principle for cortical neuronal groups. *Proc. Natl. Acad. Sci.*, 108(13):5419–5424, 2011.

H. I. Petrache, T. Zemb, L. Belloni, and V. A. Parsegian. Salt screening and specific ion adsorption determine neutral-lipid membrane interactions. *Proc. Natl. Acad. Sci.*, 103 (21):7982–7987, 2006.

F. Picard, T. Buffeteau, B. Desbat, M. Auger, and M. Pezolet. Quantitative orientation measurements in thin lipid films by attenuated total reflection infrared spectroscopy. *Biophys. J.*, 76(1):539–551, 1999.

W. Pohle and C. Selle. Fourier-transform infrared spectroscopic evidence for a novel lyotropic phase transition occurring in dioleoylphosphatidylethanolamine. *Chem. Phys. Lipids*, 82(2):191–198, 1996.

W. Pohle, C. Selle, H. Fritzsche, and H. Binder. Fourier transform infrared spectroscopy as a probe for the study of the hydration of lipid self-assemblies. i. methodology and general phenomena. *Biospectroscopy*, 4(4):267–280, 1998.

M. Prager-Khoutorsky, A. Lichtenstein, R. Krishnan, K. Rajendran, A. Mayo, Z. Kam, B. Geiger, and A. D. Bershadsky. Fibroblast polarization is a matrix-rigidity-dependent process controlled by focal adhesion mechanosensing. *Nat. Cell Biol.*, 13(12):1457–1465, 2011.

O. Purrucker, A. Förtig, R. Jordan, and M. Tanaka. Supported membranes with well-defined polymer tethers – incorporation of cell receptors. *ChemPhysChem*, 5(3):327–335, 2004.

O. Purrucker, A. Förtig, K. Lüdtke, R. Jordan, and M. Tanaka. Confinement of transmembrane cell receptors in tunable stripe micropatterns. *J. Am. Chem. Soc.*, 127(4):1258–1264, 2005.

J. O. Rädler, I. Koltover, T. Salditt, and C. R. Safinya. Structure of DNA-cationic liposome complexes: DNA intercalation in multilamellar membranes in distinct interhelical packing regimes. *Science*, 275(5301):810–814, 1997.

A. M. Rajnicek. Temporally and spatially coordinated roles for Rho, Rac, Cdc42 and their effectors in growth cone guidance by a physiological electric field. *J. Cell Sci.*, 119(9): 1723–1735, 2006.

A. M. Rajnicek, S. Britland, and C. D. McCaig. Contact guidance of CNS neurites on grooved quartz: influence of groove dimensions, neuronal age and cell type. *J. Cell Sci.*, 110(23):2905–2913, 1997.

R. P. Rand and V. A. Parsegian. Hydration forces between phospholipid bilayers. *Biochim. Biophys. Acta*, 988(3):351–376, 1989.

P. Rauch, P. Heine, B. Goettgens, and J. A. Käs. Forces from the rear: deformed microtubules in neuronal growth cones influence retrograde flow and advancement. *New J. Phys.*, 15(1):015007, 2013.

E. Ravasz and A. L. Barabási. Hierarchical organization in complex networks. *Phys. Rev. E*, 67(2), 2003.

C. A. Reinhart-King, M. Dembo, and D. A. Hammer. The dynamics and mechanics of endothelial cell spreading. *Biophys. J.*, 89(1):676–689, 2005.

E. A. J. Reits and J. J. Neefjes. From fixed to FRAP: measuring protein mobility and activity in living cells. *Nat. Cell Biol.*, 3(6):E145–E147, 2001.

Y. Rezus and H. Bakker. Observation of immobilized water molecules around hydrophobic groups. *Phys. Rev. Lett.*, 99(14), 2007.

J. Riemenschneider, A. Wulf, and R. Ludwig. The effects of temperature and H/D isotopic dilution on the transmission and attenuated total reflection FTIR spectra of water. *Z. Phys. Chem.*, 223(9):1011–1022, 2009.

W. H. Robertson and M. A. Johnson. Molecular aspects of halide ion hydration: The cluster approach. *Annu. Rev. Phys. Chem.*, 54(54):173–213, 2003.

E. Robles and T. M. Gomez. Focal adhesion kinase signaling at sites of integrin-mediated adhesion controls axon pathfinding. *Nat. Neurosci.*, 9(10):1274–1283, 2006.

T. Rog, K. Murzyn, J. Milhaud, M. Karttunen, and M. Pasenkiewicz-Gierula. Water isotope effect on the phosphatidylcholine bilayer properties: A molecular dynamics simulation study. *J. Chem. Phys. B*, 113(8):2378–2387, 2009.

J. R. Roscioli, E. G. Diken, M. A. Johnson, S. Horvath, and A. B. McCoy. Prying apart a water molecule with anionic H-bonding: A comparative spectroscopic study of the $X^- \cdot H_2O$ (X = OH, O, F, Cl, and Br) binary complexes in the 600-3800 cm^{-1} region. *J. Phys. Chem. A*, 110(15):4943–4952, 2006.

M. Rubinov and O. Sporns. Complex network measures of brain connectivity: Uses and interpretations: Computational models of the brain. *NeuroImage*, 52(3):1059–1069, 2010.

E. Sackmann. Supported membranes: Scientific and practical applications. *Science*, 271 (5245):43–48, 1996.

R. Salvador, J. Suckling, M. R. Coleman, J. D. Pickard, D. Menon, and E. Bullmore. Neurophysiological architecture of functional magnetic resonance images of human brain. *Cereb. Cortex*, 15(9):1332–1342, 2005.

C. Sammon, C. Mura, J. Yarwood, N. Everall, R. Swart, and D. Hodge. FTIR-ATR studies of the structure and dynamics of water molecules in polymeric matrixes. A comparison of PET and PVC. *J. Phys. Chem. B*, 102(18):3402–3411, 1998.

M. Santiago-Medina, J. P. Myers, and T. M. Gomez. Imaging adhesion and signaling dynamics in *Xenopus laevis* growth cones. *Dev. Neurobiol.*, 72(4):585–599, 2012.

A. Saupe. Kernresonanzen in kristallinen Flüssigkeiten und in kristallinflüssigen Lösungen. i. *Z. Naturforsch., A: Phys. Sci.*, A19(2):161, 1964.

P. Saveyn, P. van der Meeren, M. Zackrisson, T. Narayanan, and U. Olsson. Subgel transition in diluted vesicular dodab dispersions. *Soft Matter*, 5(8):1735–1742, 2009.

B. Schlosshauer, E. Müller, B. Schröder, H. Planck, and H.-W. Müller. Rat schwann cells in bioresorbable nerve guides to promote and accelerate axonal regeneration. *Brain Res.*, 963(1-2):321–326, 2003.

H. Schmiedel. Ordnungsmatrix und intramolekulare Bewegung in thermotropen Kristallen. *Wissenschaftliche Zeitschrift der Karl-Marx-Universität Leipzig*, Mathematisch-Naturwissenschaftliche Reihe(33):441–449, 1984.

P. C. Schulz, J. L. Rodriguez, F. A. Soltero-Martinez, J. E. Puig, and Z. E. Proverbio. Phase behaviour of the dioctadecyldimethylammonium bromide water system. *J. Therm. Anal. Cal.*, 51(1):49–62, 1998.

G. J. Schütz, H. Schindler, and T. Schmidt. Single-molecule microscopy on model membranes reveals anomalous diffusion. *Biophys. J.*, 73(2):1073–1080, 1997.

U. S. Schwarz and M. L. Gardel. United we stand - integrating the actin cytoskeleton and cell-matrix adhesions in cellular mechanotransduction. *J. Cell Biol.*, 125(13):3051–3060, 2012.

J. M. Seddon and G. Cevc. Lipid polymorphism: Structure and stability of lyotropic mesophases of phospholipids. In G. Cevc, editor, *Phospholipids Handbook*, pages 403–454. Marcel Dekker, Inc., New York, 1993.

J. M. Seddon and R. H. Templer. Chapter 3: Polymorphism of lipid-water systems. In *Structure and Dynamics of Membranes*, volume 1 of *Handbook of biological physics*, pages 97–160. Elsevier, 1995. ISBN 9780444819758. doi: 10.1016/S1383-8121(06)80020-5.

J. Seelig. Deuterium magnetic resonance: theory and application to lipid membranes. *Q. Rev. Biophys.*, 10(03):353–418, 1977.

P. C. Seitz, M. Reif, K. Yoshikawa, R. Jordan, and M. Tanaka. Dissipative structure formation in lipid/lipopolymer monolayers. *J. Phys. Chem. B*, 115(10):2256–2263, 2011.

W. Senaratne, L. Andruzzi, and C. K. Ober. Self-assembled monolayers and polymer brushes in biotechnology: Current applications and future perspectives. *Biomacromolecules*, 6(5):2427–2448, 2005.

O. Shefi, E. Ben-Jacob, and A. Ayali. Growth morphology of two-dimensional insect neural networks: Computational Neuroscience Trends in Research 2002. *Neurocomputing*, 44–46(0):635–643, 2002a.

O. Shefi, I. Golding, R. Segev, E. Ben-Jacob, and A. Ayali. Morphological characterization of *in vitro* neuronal networks. *Phys. Rev. E*, 66(2):021905, 2002b.

A. P. Siegel, M. J. Murcia, M. Johnson, M. Reif, R. Jordan, J. Rühe, and C. A. Naumann. Compartmentalizing a lipid bilayer by tuning lateral stress in a physisorbed polymer-tethered membrane. *Soft Matter*, 6(12):2723, 2010.

J. Silver and J. H. Miller. Regeneration beyond the glial scar. *Nat. Rev. Neurosci.*, 5(2): 146–156, 2004.

K. Simons and E. Ikonen. Functional rafts in cell membranes. *Nature*, 387(6633):569–572, 1997.

S. J. Singer and G. L. Nicolson. The fluid mosaic model of the structure of cell membranes. *Science*, 175(4023):720–731, 1972.

S. W. I. Siu, R. Vacha, P. Jungwirth, and R. A. Böckmann. Biomolecular simulations of membranes: Physical properties from different force fields. *J. Chem. Phys.*, 128(12): 125103, 2008.

J. L. Skinner. Following the motions of water molecules in aqueous solutions. *Science*, 328 (5981):985–986, 2010.

J. D. Smith, C. D. Cappa, K. R. Wilson, R. C. Cohen, P. L. Geissler, and R. J. Saykally. Unified description of temperature-dependent hydrogen-bond rearrangements in liquid water. *Proc. Natl. Acad. Sci. U. S. A.*, 102(40):14171–14174, 2005.

J. Solon, I. Levental, K. Sengupta, P. C. Georges, and P. A. Janmey. Fibroblast adaptation and stiffness matching to soft elastic substrates. *Biophys. J.*, 93(12):4453–4461, 2007.

O. Sporns. The human connectome: a complex network. *Ann. N.Y. Acad. Sci.*, 1224(1): 109–125, 2011.

O. Sporns and J. D. Zwi. The small world of the cerebral cortex. *Neuroinformatics*, 2(2): 145–162, 2004.

O. Sporns, G. Tononi, and G. M. Edelman. Theoretical neuroanatomy: Relating anatomical and functional connectivity in graphs and cortical connection matrices. *Cereb. Cortex*, 10(2):127–141, 2000.

O. Sporns, D. Chialvo, M. Kaiser, and C. Hilgetag. Organization, development and function of complex brain networks. *Trends Cogn. Sci.*, 8(9):418–425, 2004.

C. J. Stam. Characterization of anatomical and functional connectivity in the brain: A complex networks perspective. *Int. J. Psychophysiol.*, 77(3):186–194, 2010.

C. J. Stam and E. C. W. van Straaten. The organization of physiological brain networks. *Clin. Neurophysiol.*, 123(6):1067–1087, 2012.

T. Steiner. The hydrogen bond in the solid state. *Angew. Chem. Int. Ed. Engl.*, 41(1):49–76, 2002.

C. C. Steinmetz, I. Buard, T. Claudepierre, K. Nagler, and F. W. Pfrieger. Regional variations in the glial influence on synapse development in the mouse CNS. *J. Physiol.*, 577 (1):249–261, 2006.

D. A. Stenger, C. J. Pike, J. J. Hickman, and C. W. Cotman. Surface determinants of neuronal survival and growth on self-assembled monolayers in culture. *Brain Res.*, 630 (1-2):136–147, 1993.

E. Stepien, J. Stanisz, and W. Korohoda. Contact guidance of chick embryo neurons on single scratches in glass and on underlying aligned human skin fibroblasts. *Cell Biol. Int.*, 23(2):105–116, 1999.

M. Stobb, J. M. Peterson, B. Mazzag, E. Gahtan, and S. Hayasaka. Graph theoretical model of a sensorimotor connectome in zebrafish. *PLoS ONE*, 7(5):e37292, 2012.

S. H. Strogatz. Exploring complex networks. *Nature*, 410(6825):268–276, 2001.

Y. Sun, Z. Huang, W. Liu, K. Yang, K. Sun, S. Xing, D. Wang, W. Zhang, and X. Jiang. Surface coating as a key parameter in engineering neuronal network structures *In Vitro*. *Biointerphases*, 7(1-4), 2012.

H. G. Sundararaghavan, G. A. Monteiro, B. L. Firestein, and D. I. Shreiber. Neurite growth in 3D collagen gels with gradients of mechanical properties. *Biotechnol. Bioeng.*, 102(2): 632–643, 2009.

D. M. Suter and P. Forscher. Substrate-cytoskeletal coupling as a mechanism for the regulation of growth cone motility and guidance. *J. Neurobiol.*, 44(2):97–113, 2000.

Daniel M. Suter and Kyle E. Miller. The emerging role of forces in axonal elongation. *Prog. Neurobiol.*, 94(2):91–101, 2011.

T. M. Svitkina, A. A. Neyfakh, and A. D. Bershadsky. Actin cytoskeleton of spread fibroblasts appears to assemble at the cell edges. *J. Cell Sci.*, 82:235–248, 1986.

L. K. Tamm and S. A. Tatulian. Infrared spectroscopy of proteins and peptides in lipid bilayers. *Q. Rev. Biophys.*, 30(4):365–429, 1997.

L.K Tamm and H.M McConnell. Supported phospholipid bilayers. *Biophys. J.*, 47(1): 105–113, 1985.

J. L. Tan, J. Tien, D. M. Pirone, D. S. Gray, K. Bhadriraju, and C. S. Chen. Cells lying on a bed of microneedles: An approach to isolate mechanical force. *Proc. Natl. Acad. Sci.*, 100(4):1484–1489, 2003.

M. Tanaka and E. Sackmann. Polymer-supported membranes as models of the cell surface. *Nature*, 437(7059):656–663, 2005.

C. Tanford. The hydrophobic effect and the organization of living matter. *Science*, 200 (4345):1012–1018, 1978.

N. Tawil, P. Wilson, and S. Carbonetto. Integrins in point contacts mediate cell spreading: factors that regulate integrin accumulation in point contacts vs. focal contacts. *J. Cell Biol.*, 120(1):261–271, 1993.

S.-Y. Tee, J. Fu, C. S. Chen, and P. A. Janmey. Cell shape and substrate rigidity both regulate cell stiffness. *Biophys. J.*, 100(5):L25–L27, 2011.

The Histology Guide. Extracellular matrix. University of Leeds. URL `http://www.histology.leeds.ac.uk/tissue_types/connective/connective_groundS.php`. 15.05.2013.

D. P. Tieleman, S. J. Marrink, and H. J.C. Berendsen. A computer perspective of membranes: molecular dynamics studies of lipid bilayer systems. *Biochim. Biophys. Acta, Rev. Biomembr.*, 1331(3):235–270, 1997.

K. J. Tielrooij, D. Paparo, L. Piatkowski, H. J. Bakker, and M. Bonn. Dielectric relaxation dynamics of water in model membranes probed by terahertz spectroscopy. *Biophys. J.*, 97(9):2484–2492, 2009.

L. Trichet, J. Le Digabel, R. J. Hawkins, S. R. K. Vedula, M. Gupta, C. Ribrault, P. Hersen, R. Voituriez, and B. Ladoux. Evidence of a large-scale mechanosensing mechanism for cellular adaptation to substrate stiffness. *Proc. Natl. Acad. Sci.*, 109(18):6933–6938, 2012.

J. Umemura, T. Kawai, T. Takenaka, M. Kodama, Y. Ogawa, and S. Seki. Fourier-transform infrared study on the phase-transitions of a water-dioctadecyldimethylammonium chloride system. *Mol. Cryst. Liq. Cryst.*, 112(3-4):293–309, 1984.

M. P. van den Heuvel and H. E. Hulshoff Pol. Exploring the brain network: A review on resting-state fMRI functional connectivity. *Eur. Neuropsychopharmacol.*, 20(8):519–534, 2010.

M. P. van den Heuvel, C. J. Stam, R. S. Kahn, and H. E. Hulshoff Pol. Efficiency of functional brain networks and intellectual performance. *J. Neurosci.*, 29(23):7619–7624, 2009.

D. van der Spoel, P. J. van Maaren, and H. J.C. Berendsen. A systematic study of water models for molecular simulation: Derivation of water models optimized for use with a reaction field. *J. Chem. Phys.*, 108(24):10220–10230, 1998.

G. van Meer, D. R. Voelker, and G. W. Feigenson. Membrane lipids: where they are and how they behave. *Nat. Rev. Mol. Cell Biol.*, 9(2):112–124, 2008.

A. van Ooyen. Using theoretical models to analyse neural development. *Nat. Rev. Neurosci.*, 12(6):311–326, 2011.

S. Varier, M. Kaiser, and K. J. Friston. Neural development features: Spatio-temporal development of the *Caenorhabditis elegans* neuronal network. *PLoS Comp. Biol.*, 7(1): e1001044, 2011.

L. R. Varshney, B. L. Chen, E. Paniagua, D. H. Hall, D. B. Chklovskii, and O. Sporns. Structural properties of the *Caenorhabditis elegans* neuronal network. *PLoS Comp. Biol.*, 7(2):e1001066, 2011.

S. Y. Venyaminov and F. G. Prendergast. Water (H_2O and D_2O) molar absorptivity in the 1000-4000 cm^{-1} range and quantitative infrared spectroscopy of aqueous solutions. *Anal. Biochem.*, 248(2):234–245, 1997.

V. Vogel and M. Sheetz. Local force and geometry sensing regulate cell functions. *Nat. Rev. Mol. Cell Biol.*, 7(4):265–275, 2006.

V. V. Volkov, D. J. Palmer, and R. Righini. Heterogeneity of water at the phospholipid membrane interface. *J. Chem. Phys. B*, 111(6):1377–1383, 2007.

V. V. Volkov, Y. Takaoka, and R. Righini. What are the sites water occupies at the interface of a phospholipid membrane? *J. Phys. Chem. B*, 113(13):4119–4124, 2009.

M. L. Wagner and L. K. Tamm. Tethered polymer-supported planar lipid bilayers for reconstitution of integral membrane proteins: Silane-polyethyleneglycol-lipid as a cushion and covalent linker. *Biophys. J.*, 79(3):1400–1414, 2000.

G. E. Walrafen. Raman spectral studies of effects of temperature on water structure. *J. Chem. Phys.*, 47(1):114–&, 1967.

L. Wang, C. Yu, H. Chen, W. Qin, Y. He, F. Fan, Y. Zhang, M. Wang, K. Li, Y. Zang, T. S. Woodward, and C. Zhu. Dynamic functional reorganization of the motor execution network after stroke. *Brain*, 133(4):1224–1238, 2010.

N. Wang, J. D. Tytell, and D. E. Ingber. Mechanotransduction at a distance: mechanically coupling the extracellular matrix with the nucleus. *Nat. Rev. Mol. Cell Biol.*, 10(1):75–82, 2009.

D. J. Watts and S. H. Strogatz. Collective dynamics of 'small-world' networks. *Nature*, 393(6684):440–442, 1998.

S. Weigel, T. Osterwalder, U. Tobler, L. Yao, M. Wiesli, T. Lehnert, A. Pandit, A. Bruinink, and R. Zhou. Surface microstructures on planar substrates and textile fibers guide neurite outgrowth: A scaffold solution to push limits of critical nerve defect regeneration? *PLoS ONE*, 7(12):e50714, 2012.

P. Wernet, D. Nordlund, U. Bergmann, M. Cavalleri, M. Odelius, H. Ogasawara, La Naslund, T. K. Hirsch, L. Ojamae, P. Glatzel, L. G.M. Pettersson, and A. Nilsson. The structure of the first coordination shell in liquid water. *Science*, 304(5673):995–999, 2004.

J. G. White, E. Southgate, J. N. Thomson, and S. Brenner. The structure of the nervous system of the nematode *Caenorhabditis elegans*. *Philos. Trans. R. Soc. B: Biol. Sci.*, 314 (1165):1–340, 1986.

L. Woiterski, D. W. Britt, J. A. Käs, and C. Selle. Oriented confined water induced by cationic lipids. *Langmuir*, 28(10):4712–4722, 2012.

L. Woiterski, T. Claudepierre, R. Luxenhofer, R. Jordan, and J. A. Käs. Stages of neuronal network formation. *New J. Phys.*, 15(2):025029, 2013.

F. G. Wu, N. N. Wang, and Z. W. Yu. Nonsynchronous change in the head and tail of dioctadecyldimethylammonium bromide molecules during the liquid crystalline to coagel phase transformation process. *Langmuir*, 25(23):13394–13401, 2009.

G. Wu, Y. Fang, Z. H. Lu, and R. W. Ledeen. Induction of axon-like and dendrite-like processes in neuroblastoma cells. *J. Neurocytol.*, 27(1):1–14, 1998.

M. A. Yorek. Biological distribution. In G. Cevc, editor, *Phospholipids Handbook*, pages 745–775. Marcel Dekker, Inc., New York, 1993.

K. Yoshimura and M. Sokabe. Mechanosensitivity of ion channels based on protein-lipid interactions. *J. R. Soc. Interface*, 7:S307–S320, 2010.

G. Zeck and P. Fromherz. Noninvasive neuroelectronic interfacing with synaptically connected snail neurons immobilized on a semiconductor chip. *Proc. Natl. Acad. Sci.*, 98 (18):10457–10462, 2001.

A. Zemel, F. Rehfeldt, A. E. X. Brown, D. E. Discher, and S. A. Safran. Optimal matrix rigidity for stress-fibre polarization in stem cells. *Nat. Phys.*, 6(6):468–473, 2010.

Y. J. Zhang and P. S. Cremer. Interactions between macromolecules and ions: the Hofmeister series. *Curr. Opin. Chem. Biol.*, 10(6):658–663, 2006.

Y.-P. Zhang, R. N. A. H. Lewis, and R. N. McElhaney. Calorimetric and Spectroscopic Studies of the Thermotropic Phase Behavior of the n-Saturated 1,2-Diacylphosphatidylglycerols. *Biophys. J.*, 72(2):779–793, 1997.

W. Zhao, D. E. Moilanen, E. E. Fenn, and M. D. Fayer. Water at the surfaces of aligned phospholipid multibilayer model membranes probed with ultrafast vibrational spectroscopy. *J. Am. Chem. Soc.*, 130(42):13927–13937, 2008.

Z. G. Zhong, S. Yokoyama, M. Noda, and H. Higashida. Overexpression of adhesion molecule L1 in NG108-15 neuroblastoma X glioma hybrid cells enhances dibutyryl cyclic AMP-induced neurite outgrowth and functional synapse formation with myotubes. *J. Neurochem.*, 68(6):2291–2299, 1997.

I. S. Zuhorn, J. B. F. N. Engberts, and D. Hoekstra. Gene delivery by cationic lipid vectors: Overcoming cellular barriers. *Eur. Biophys. J.*, 36(4-5):349–362, 2007.

Appendices

A. Determination of the IR Order Parameter

In the following, the derivation of the linear dichroism for thick lipid films on ATR crystals is briefly outlined. A detailed description can be found elsewhere (Binder and Schmiedel, 1999; Binder, Dezember 1999). When a lipid film is exposed to polarized electromagnetic radiation, absorption occurs due to the dipolar interaction of the electric field strength $\vec{E}$ with the transition dipole moment $\vec{\mu}$ (cf. figure A.1). The strength of the absorption is defined by the absorbance A as the negative decadic logarithm of the ratio of the intensities of the IR beam before I_0 and after the absorption I:

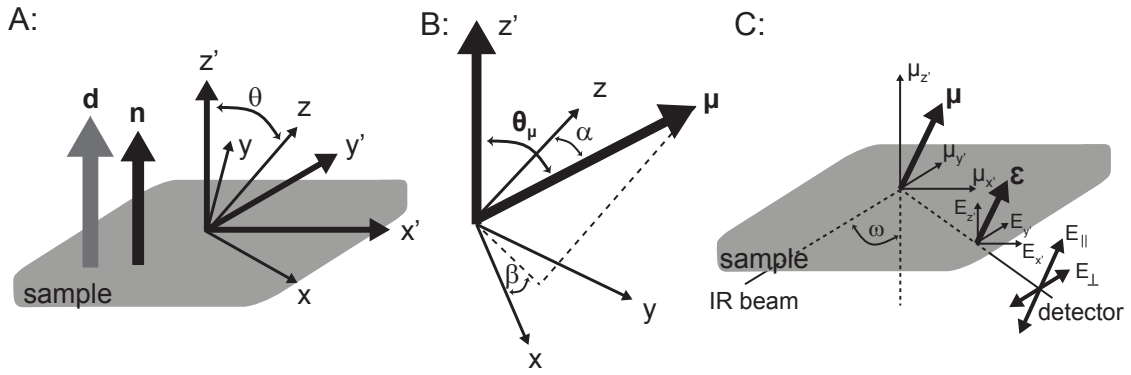

Figure A.1.: *A:* The lipid film in the molecular coordinate system {x,y,z} with director $\vec{d}$ is parallel to the supporting ATR crystal with normal $\vec{n}$. The laboratory coordinate system {x′,y′,z′} is defined such that its z′-axis is parallel to $\vec{n}$ and $\vec{d}$. *B:* Transition dipole moment $\vec{\mu}$ in the molecular coordinate system. *C:* Electric field $\vec{E}$ and $\vec{\mu}$ in the laboratory coordinate system.

$$A = -\log_{10}\left(\frac{I}{I_0}\right). \tag{A.1}$$

Microscopically, the absorbance A_{pol} is proportional to the averaged squared projection of the transition dipole moment on the electric field and can be written as the sum of an isotropic and an anisotropic part depending on the orientation:

$$A_{\mathrm{pol}} = A_{\max} \cdot \langle (\vec{\mu} \cdot \vec{e})^2 \rangle = A_{\mathrm{iso}} + \delta A, \tag{A.2}$$

where $A_{iso} = A_{max}/3$ for an isotropic sample. The orientation dependent part of the absorbance δA can be written as a product of three tensors (Schmiedel, 1984):

$$\delta A = \frac{2}{3} A_{max} \cdot M_{ij} \cdot S_{ijkl} \cdot P_{kl}. \tag{A.3}$$

The indices i, j and k, l correspond to the coordinate axes of the molecular {x,y,z} and laboratory {x',y',z'} frames, respectively. The three tensors describe the orientation of the transition dipole moments M_{ij} in the molecule system as well as the direction of the polarization of the electric field P_{kl} and the average orientation of the molecules S_{ijkl} in the laboratory system, respectively. As M_{ij} and P_{kl} are traceless and symmetric, only five independent components remain for both tensors M_m and P_n ($m, n = 1, \ldots, 5$) (Saupe, 1964; Schmiedel, 1984):

$$\begin{aligned} M_m &\equiv \left(S_\alpha, \frac{1}{\sqrt{3}} D_{\alpha\beta}, \frac{1}{\sqrt{3}} D'_{\alpha\beta}, \frac{1}{\sqrt{3}} C_{\alpha\beta}, \frac{1}{\sqrt{3}} C'_{\alpha\beta} \right) \\ P_n &\equiv \left(S_{\alpha'}, \frac{1}{\sqrt{3}} D_{\alpha'\beta'}, \frac{1}{\sqrt{3}} D'_{\alpha'\beta'}, \frac{1}{\sqrt{3}} C_{\alpha'\beta'}, \frac{1}{\sqrt{3}} C'_{\alpha'\beta'} \right). \end{aligned} \tag{A.4}$$

The elements of the dipole orientation tensor M_m are defined as (P_n can be obtained similarly by exchanging α and β by α' and β'):

$$\begin{aligned} S_\alpha &= \frac{1}{2}(3 \cdot \cos^2\alpha - 1) \\ D_{\alpha\beta} &= \frac{3}{2} \sin^2\alpha \cdot \cos 2\beta, & D'_{\alpha\beta} &= \frac{3}{2} \sin^2\alpha \cdot \sin 2\beta \\ C_{\alpha\beta} &= \frac{3}{2} \sin 2\alpha \cdot \cos\beta, & C'_{\alpha\beta} &= \frac{3}{2} \sin 2\alpha \cdot \sin\beta. \end{aligned} \tag{A.5}$$

The angles (α, β) and (α', β') denote the polar angles of $\vec{\mu}$ and $\vec{\epsilon}$ in the molecular and laboratory coordinate system (see figure A.1, B), respectively. The anisotropic absorbance (equation A.3) becomes:

$$\delta A = \frac{2}{3} A_{max} \cdot M_m \cdot S_{mn} \cdot P_n, \qquad m, n = 1, 2, \ldots, 5 \tag{A.6}$$

The matrix of the molecular orientation S_{mn} can be simplified for the special case of an axial symmetric distribution of transition dipole moments around the z'-axis (see figure A.1). Thus, only tensor elements with $n = 1$ do not vanish (Saupe, 1964). For the special case that the transition dipole moment μ is parallel to the z-axis of the molecular coordinate system $\{x, y, z\}$, one has $\alpha_\mu = 0$ and only one element of M remains: $M_1 = 1$, while $M_2 = M_3 = M_4 = M_5 = 0$. Thus, the absorbance simplifies to:

$$\delta A = \frac{2}{3} A_{max} \cdot S_{11} \cdot P_1 \tag{A.7}$$

The IR order parameter S_{IR} is defined as the tensor element $S_{11} \equiv S_{\mathrm{IR}}$ of the molecular orientation tensor (Saupe, 1964) given by:

$$S_{\mathrm{IR}} = \frac{1}{2}\left\langle 3 \cdot \cos^2\theta_\mu - 1 \right\rangle \tag{A.8}$$

where θ_μ is the angle enclosed by the axis z' in the laboratory system and the transition dipole moment $\vec{\mu}$ (see figure A.1).

For the cases of $\alpha' = 0°$ and $\alpha' = 90°$ which corresponds to the incidence of parallel and perpendicular polarized light, respectively, and using equations A.1, A.4 and A.7, the absorbance in the laboratory system becomes:

$$A_{z'} = A_{\max} \cdot (1 + 2S_{\mathrm{IR}}) \qquad \text{and} \qquad A_{x'} = A_{y'} = A_{\max} \cdot (1 - S_{\mathrm{IR}}) \tag{A.9}$$

The absorbance in the direction of polarization of the incident light can be expressed in dependence on the of vector the electric field strength $\vec{E} = (E_{x'}, E_{y'}, E_{z'})$ and its amplitude E_0:

$$A_{\parallel} = \left(\frac{E_{x'}}{E_0}\right)^2 \cdot A_{x'} + \left(\frac{E_{z'}}{E_0}\right)^2 \cdot A_{z'} \qquad \text{and} \qquad A_{\perp} = \left(\frac{E_{y'}}{E_0}\right)^2 \cdot A_{y'} \tag{A.10}$$

Combining the last two equations, the absorbance can be rewritten as a function of the IR order parameter S_{IR}:

$$A_{\parallel} = k \cdot (K_1 + K_2) \cdot S_{\mathrm{IR}} \qquad \text{and} \qquad A_{\perp} = k \cdot (1 - S_{IR}) \tag{A.11}$$

where K_1 and K_2 are optical constants and k a proportionality constant that depends on the maximum absorbance $A_{\max}$ (Harrick, 1987):

$$K_1 = \frac{E_{z'}^2 + E_{x'}^2}{E_{y'}^2}, \qquad K_2 = \frac{2E_{z'}^2 - E_{x'}^2}{E_{y'}^2} \qquad \text{and} \qquad k = A_{\max} \cdot \left(\frac{E_{y'}}{E_0}\right)^2 \tag{A.12}$$

The dichroic ratio, which can be measured, is then defined as the ratio of the absorbance measured with parallel and perpendicular polarized light, respectively, and can be used to determine the IR order parameter:

$$S_{\mathrm{IR}} = \frac{R - K_1}{R + K_2} \qquad \text{with} \qquad R \equiv \frac{A_{\parallel}}{A_{\perp}}. \tag{A.13}$$

In the experiments carried out for this work, a zinc selenide crystal was used which has $K_1 = 2$ and $K_2 = 2.54$ in the thick film approximation (Harrick, 1987; Binder, 2003).

B. Preparation and Characterization of DODAX

B.1. Synthesis of DODAI, DODAC and DODAF

While DODAB was purchased by Sigma-Adrich, the other lipid analogs could not be obtained commercially or not at adequate purity. Therefore, DODAI and DODAC were produced by ion exchange and DODAF by precipitation of insoluble AgBr.

Chemicals:

- KI ($\geq$ 99.5 %, Roth, 6750.1)
- KCl ($\geq$ 99.5 %, Roth, 6781.3)
- AgF ($\geq$ 99 %, Fluka, 85184)
- DODAB ($\geq$ 98 %, Sigma-Aldrich, D2779)
- $CHCl_3$ ($\geq$ 99.8 %, Merck, 102432)
- Isopropanol ($\geq$ 99.8 % Merck, 100998)

Preparation:

DODAI 5.52 g KI (33.3 mmol, 20-fold excess) solved in 26 mL deionized water (Millipore) were dropwise added under stirring to a solution of 1 g DODAB (1.58 mmol) dissolved in 100 mL isopropanol at room temperature. After addition of 100 mL water and a sufficient amount of $CHCl_3$, the organic phase was separated from the aqueous, subsequently dried over Na_2SO_4, and filtrated. The solvent and traces of water were removed from the filtrate under reduced pressure (1 mbar) at 40 °C. This procedure was repeated for a second time with the raw product DODAI to remove further residues of DODAB. The resulting white powder was finally purified by twofold crystallization from a chloroformic solution at -18 °C and dried in vacuum at room temperature.

DODAC was analogously obtained from 1 g DODAB in 100 mL isopropanol. However, a tenfold excess of aqueous KCl (1.29 g, 17.4 mmol) in 26 mL pure water was used

for the ion exchange to obtain a clear solution of the mixture of DODAB, DODAC, and KCl. The ion exchange procedure was carried out twice and work-up and purification of the raw product were identical to the protocol used for DODAI. The final yield of both products DODAI and DODAC was close to 100 % of the theoretical value. Purity and constitution of the products were confirmed as described in the following subsections.

DODAF 1 mL of an aqueous 0.7894 mM AgF solution (0.1 g AgF in 1 mL pure water) was slowly dropped into a solution of 0.497 g (0.7894 mmol) DODAB in 46.5 mL isopropanol and 15.5 mL pure water. AgBr precipitated quantitatively and was removed by filtration by a glass filter (Por. 3, Rasotherm, Jena, Germany). The remaining DODAF solution was separated from the solvent by rotary evaporation and completely dried in vacuum at 40 °C over night resulting in a yield close to 100 % of the theory. Analytical data related to DODAF following.

B.2. Energy dispersive x-ray (EDX) spectroscopy

EDX spectroscopy was performed to confirm the identity of anions within the produced lipids. Spectra were acquired by a Genesis micro X-ray fluorescence system (EDAX/Ametek, Wiesbaden, Germany) using a SUTW-sapphire detector (tilt 0.00 °, 30 kV for DODAB, 15 kV for the other lipids). The higher voltage for DODAB was used to distinguish bromide from sulfur. DODAF, DODAC, and DODAI samples exhibited peaks corresponding to the expected composition. For all products, contamination by unwanted anions and cations, or other compounds, was not detected by this method. For bromide of DOBAB (educt), a strong absorption peak at 1.48 keV was observed. The results of the peak analysis are summarized in table B.1.

lipid	element	Spectral line	Peak energy (keV)	at %
DODAF	C	K_α	0.277	93.64
	F	K_α	0.676	2.25
DODAC	C	K_α	0.277	96.94
	Cl	K_α	2.62	1.42
DODAB	C	K_α	0.277	97.86
	Br	K_α	11.4	2.14
DODAI	C	K_α	0.277	97.42
	I	L_α	3.93	2.58

Table B.1.: Elemental analysis of the lipids by EDX spectroscopy

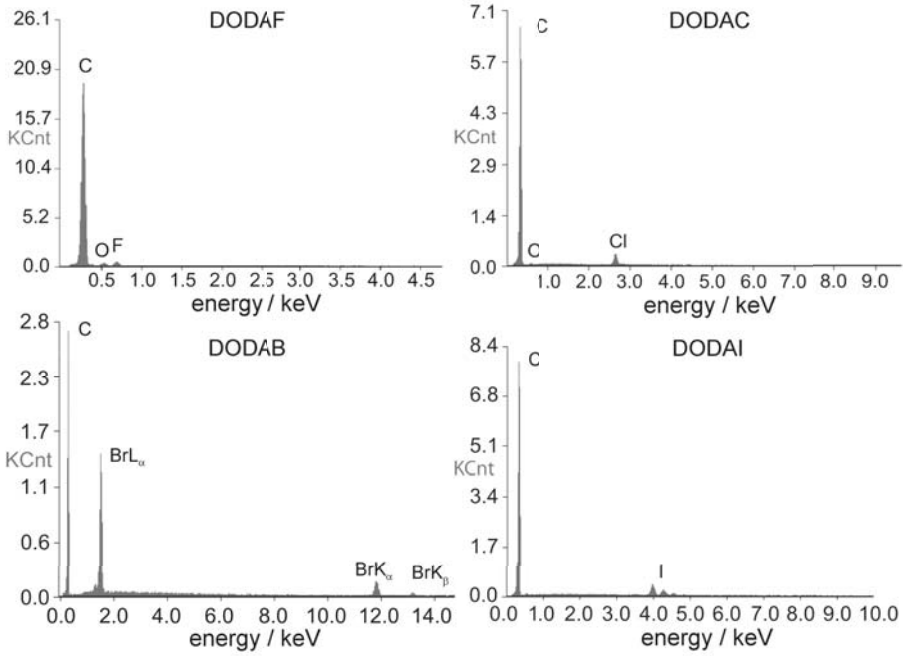

Figure B.1.: Energy dispersive X-ray spectra of DODAX (X = F, Cl, Br, I)

B.3. MALDI-TOF mass spectrometry

The purity of the quaternary ammonium ion was confirmed by MALDI-TOF (matrix assisted laser desorption/ionization-time of flight) mass spectrometry in the positive mode. All chemicals for sample preparation, MALDI-TOF MS (2,5-dihydroxybenzoic acid (DHB)) and solvents ($CHCl_3$, CH_3OH) were obtained in highest commercially available purity from Fluka (Taufkirchen, Germany) and used as supplied. All MALDI-TOF mass spectra were acquired on an Autoflex I mass spectrometer (Bruker Daltonics, Bremen, Germany) with an isotopic resolution. The system utilizes a pulsed 50 Hz nitrogen laser, emitting at 337 nm. The extraction voltage was 20 kV. All spectra were acquired in reflector mode using delayed extraction. The samples were diluted with the matrix (0.5 mol/L DHB) to give 0.2 mg/mL solutions which were directly spotted onto the MALDI target (from aluminum with a gold surface). The signals of the DHB matrix were used for calibration. Spectra were analyzed with the instrument software *Flex Analysis 2.4* (Bruker Daltonics). The peaks at 550.6 m/z correspond to the product cations, smaller contributions with lower intensity are due to isotopic exchange. Other alkyl ammonium ion species were not detected.

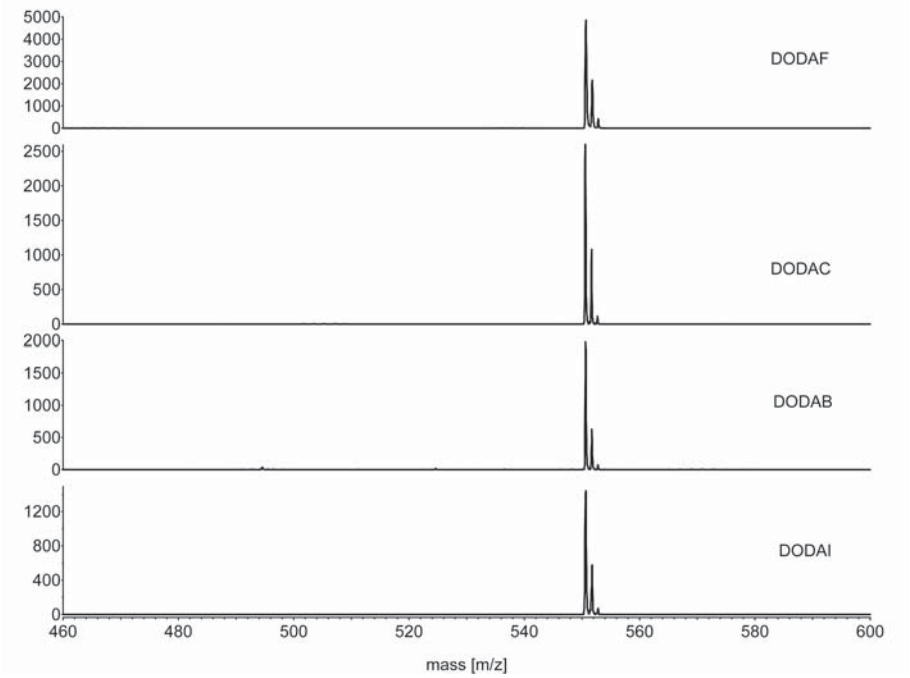

Figure B.2.: MALDITOF mass spectra of DODAX (X = F, Cl, Br, I) acquired in positive mode: Isotopically resolved signals are observed at m/z = 550.6.

B.4. NMR spectroscopy

^{1}H-NMR spectra were acquired using a Bruker 400 MHz spectrometer (Bruker Biospin, Rheinstetten, Germany) to probe the constitution of the lipids. All lipids were dissolved in $CDCl_3$ ($\geq$ 99.8 %, Uvasol, Merck, Darmstadt, Germany) (20 mg/mL). The spectra were recorded at room temperature. The signal of the solvent $CDCl_3$ at 7.26 ppm was used as the reference for the DODAX (X = F, Cl, Br, I) ^{1}H-NMR spectra. Since the EDX spectroscopic peak of fluoride is comparatively small, it led to a considerable error in the quantification. Thus, the amount of fluoride in DODAF was determined by ^{19}F-NMR spectroscopy. Here, a mixture of H_2O/CH_3OH (2:1 volume ratio) and 10 % D_2O ($\geq$ 99.98 %, Chemotrade, Leipzig, Germany) was used as solvent. CFH_2COONa (Fluka, Taufkirchen, Germany) was used as ^{19}F reference and added appropriately. Clear solutions of DODAF or DODAF/CFH_2COONa (as reference) were prepared by adding the solvent at room temperature and sonicating the mixtures at 60 °C for one hour. ^{19}F-NMR spectra were recorded at 50 °C when the solution was clear and homogeneous and scaled with respect to the ^{1}H-NMR spectra. All NMR spectra were analyzed by use of the 1D-WinNMR (Bruker, Germany) software.

Peak analysis of the ^{1}H-NMR ($CDCl_3$, 400 MHz) spectra:

DODAF (MW = 569.6 g/mol):

δ = 0.88 (t, ^{3}J = 6.99 Hz, 6 H, 2x CH_3), δ = 1.25-1.35 (60 H, 2x $(CH_2)_{15}$), δ = 1.67-1.72 (4 H, 2x

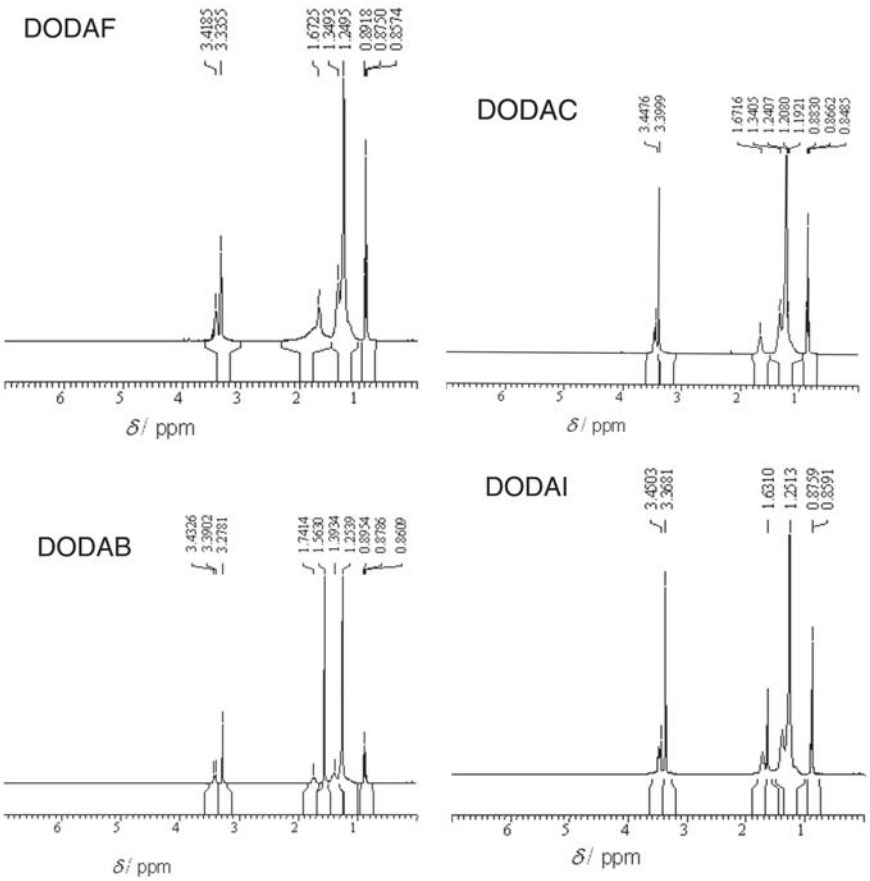

Figure B.3.: ^{1}H-NMR spectra of DODAX dissolved in $CDCl_3$. Peak picking was carried out with 1D-WinNMR (Bruker). The multiplets at 1.32 - 1.35 ppm and 1.67 - 1.74 ppm are attributed to micelles in the solution.

N-$(CH_2)_2$-$(CH_2)_2$, $\delta = 3.4$ (s, 6 H, 2x N-$(CH_3)_2$), $\delta = 3.45$ (m, 4 H, 2x N-$(CH_2)_2$)

DODAC (MW = 586.1 g/mol):

$\delta = 0.87$ (t, $^{3}J = 6.72$ Hz, 6 H, 2x CH_3), $\delta = 1.19$-1.34 (s, 60 H, 2x $(CH_2)_{15}$), $\delta = 1.67$ (m, 4 H, 2x N-$(CH_2)_2$-$(CH_2)_2$, $\delta = 3.34$ (s, 6 H, 2x N-$(CH_3)_2$), $\delta = 3.42$ (m, 4 H, 2x N-$(CH_2)_2$)

DODAB (MW = 630.6 g/mol):

$\delta = 0.88$ (t, $^{3}J = 6.9$ Hz, 6H, 2x CH_3), $\delta = 1.25$-1.39 (60 H, 2x $(CH_2)_{15}$), $\delta = 1.56$-1.74 (4 H, 2x N-$(CH_2)_2$-$(CH_2)_2$), $\delta = 3.39$ (s, 6 H, 2x N-$(CH_3)_2$), $\delta = 3.43$ (m, 4 H, 2x N-$(CH_2)_2$)

DODAI (MW = 677.5 g/mol):

$\delta = 0.88$ (t, $^{3}J = 6.6$ Hz, 6H, 2x CH_3), $\delta = 1.25$-1.37 (60 H, 2x $(CH_2)_{15}$), $\delta = 1.63$-1.71 (4 H, 2x N-$(CH_2)_2$-$(CH_2)_2$), $\delta = 3.37$ (s, 6 H, 2x N-$(CH_3)_2$), $\delta = 3.45$ (m, 4 H, 2x N-$(CH_2)_2$)

The DODAX ^{1}H-NMR spectra exhibited peaks well agreeing with earlier published data and similar compounds (Cocquyt et al., 2004; Aoki and Morimoto, 1995). Impurities were not detected.

Quantification of fluoride in DODAF (reference CFH_2COONa). DODAF and sodium mono-fluoroacetate were mixed together and measured as described above. The resulting ^{19}F-MR spectrum demonstrated two peaks at -126 ppm and -216 ppm, corresponding to the fluoride anion of DODAF and mono-fluoroacetate, respectively. The spectral peak intensities were measured and related to the weighted amounts of substances in the sample as follows:

$$\frac{N_{\mathrm{DODAF}}}{N_{\mathrm{ref}}} = \frac{m_{\mathrm{ref}}}{m_{\mathrm{DODAF}}} \frac{I_{\mathrm{ref}}}{I_{\mathrm{DODAF}}} \frac{M_{\mathrm{ref}}}{M_{\mathrm{DODAF}}} = 1.06 \pm 0.13$$

N: number of ^{19}F nuclei per molecule ($N_{\mathrm{ref}} = 1$), m: weighted sample, I: integral, M: molar weight. Per DODAF molecule, an amount of 1.06 ± 0.13 DODAF fluoride ions was found.

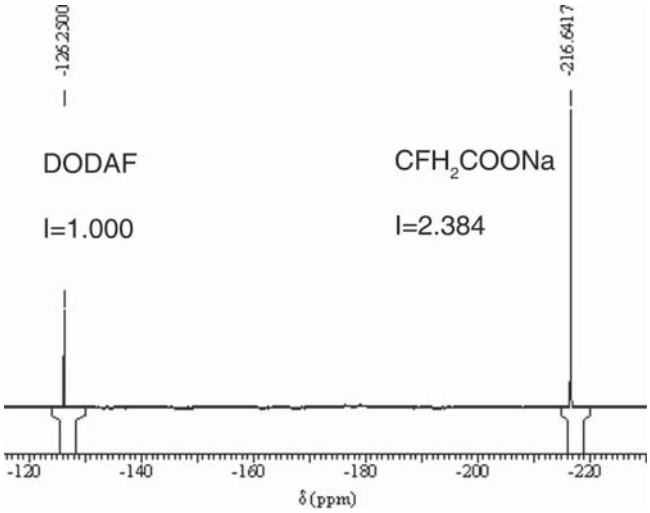

Figure B.4.: ^{19}F-NMR spectra of DODAF and CFH_2COONa dissolved in H_2O/CH_3OH (2:1 volume ratio) and 10 % D_2O.

C. Cell Culture

C.1. NG108-15 culture

NG108-15 cells are cultured in Dulbecco's modified Eagle's medium (DMEM with 4500 mg/L glucose, L-glutamine and sodium bicarbonate) (PAA, E-15810), supplemented with 10 % fetal bovine serum (FBS) (PAA, A15-043, Cöbe, Germany) and 100 U/ml

penicillin-streptomycin (PS) (Sigma-Aldrich, P0781, 10000 U/mL). It is prepared by filtering 450 ml DMEM through a 0.22 µ filter (7-4186, Neolab, Heidelberg, Germany) into a 500 mL sterile bottle and subsequently adding the FBS and the antibiotics. The serum should not be filtered to avoid the removal or denaturation of essential proteins. Neurite outgrowth on experimental dishes was enhanced by lowering the FBS content to 2.5 %.

C.1.1. Thawing

Materials:

- Warm up medium to 37 °C
- 15 mL centrifuge tube, 10 mL pipettes, 1 mL pipettor, sterile pipette tips (all VWR)
- 1 big Petri dish, ∅ 92 mm (VWR, 391-8035)

Method:

1. Remove cells from frozen storage and thaw by gently warming up cryovial.
2. Pipette 8 mL medium into 15 mL centrifuge tube.
3. Add thawed cells to medium in 15 mL centrifuge tube. Rinse cryovial with an additional 1 mL of medium to get residual cells.
4. Balance centrifuge tube and centrifuge 4 min at 800 rpm.
5. Add 9 mL of medium to new Petri dish.
6. Take cells from centrifuge and aspirate medium off pellet to remove DMSO (Dimethyl sulfoxide).
7. Redistribute cells in 1 mL medium and pipette all to new Petri dish.
8. Move dish in cross pattern to spread cells.
9. Investigate under the microscope, label dish (cell line, date, passage number, intitials) and incubate at 37 °C and 5 % CO_2.

C.1.2. Changing the medium

The medium of the NG108 cells has to be exchanged every 2 - 3 days. Therefore, it is warmed up to 37 °C. The dish is tilted and old medium is carefully sucked off on the side of the dish. Then 10 mL of new medium are slowly added to the side of the dish being cautious to not dislodge any cells.

C.1.3. Passaging of NG108-15 cells

NG108 cells grow and divide, thus before overcrowding the Petri dish, i.e. confluency, the cells have to be passaged (approximately every 5 - 7 days). Since NG108 cells are weakly adherent, they can be detached from the Petri dish without trypsinization.
Materials:

- Warm up medium to 37 °C
- 15 mL centrifuge tube, 10 mL pipettes, 1 mL pipettor, sterile pipette tips
- 1 big Petri dish

Method:

1. Aspirate medium of cells on culture dish.
2. Spray 1 mL of medium over the cells to disloge them. Repeat that four times and then move the dish a little back and forth.
3. Pool cells with medium into 15 mL centrifuge tube.
4. Redistribute cells by sucking the medium in and out with the pipette.
5. Pipette 10 mL of medium in new dish.
6. Passage $\approx$ 200 - 500 µL of cells in medium (depending on density) to new dish by dropping them in a spreading pattern.
7. Label dishes (cell line, date, passage number, initials) and incubate

C.1.4. Freezing of cells

Materials:

- Warm up serum and DMSO (Sigma-Aldrich, D2650)
- 15 mL centrifuge tube, cryovials, 10 mL pipettes, 1 mL pipettor, sterile pipette tips
- CoolCell (BCS-136, BioCision, Mill Valley, CA) or polystyrene box

Method:

1. Prepare freezing medium: 90 % normal growth medium and 10 % DMSO (1 mL per cryovial). Note: Do this ahead of time because slightly exothermic mixing of DMSO and serum may damage the cells.
2. Aspirate medium off cells on culture dish.
3. Disloge the cells with 1-2 mL of medium as described for the passaging.

4. Pool cells with medium into a 15 mL centrifuge tube.
5. Passage $\approx 1.5 \cdot 10^6$ cells in medium ($\approx 200\,\mu L$) into each cryovial and slowly add 1 mL freezing medium (over 1 - 2 min).
6. Label cryovials with cell type, passage number, date and initials.
7. Place cryovials in CoolCell. Alternatively, place cryovials in a polystyrene box and wrap in paper towels followed by aluminium foil which insulates the cryovials and assures a slow freezing process (about 1 °C/min).
8. Freeze at -85 °C for a day before transferring to liquid nitrogen storage.

C.2. Primary RGC culture

Retinal ganglion cells (RGCs) were prepared from postnatal (P7) BALB/c mice provided by the animal facility. The mice were killed by decapitation according to institutional guidelines. Retinae were isolated and RGCs purified by first removing microglia and subsequently binding of RGCs to a culture plate as described previously (Claudepierre et al., 2008; Steinmetz et al., 2006). RGCs were cultured in Neurobasal medium (Gibco/Invitrogen, Darmstadt, Germany) supplemented with (all from Sigma-Aldrich, except where indicated) pyruvate (1 mmol/L), glutamine (2 mmol/L; Gibco/Invitrogen), N-acetyl-L-cysteine (60 µg/mL), putrescine (16 µg/mL), selenite (40 ng/mL), bovine serum albumin (100 µg/mL; fraction V, crystalline grade), streptomycin (100 µg/mL), penicillin (100 U/mL), triiodothyronine (40 ng/mL), holotransferrin (100 µg/mL), dibutyryl cyclic AMP (250 µmol/L), insulin (5 µg/mL), progesterone (62 ng/mL), B27 (1:50, Gibco/Invitrogen), D-manose (50 µmol/L), brain-derived neurotrophic factor (BDNF; 25 ng/mL; PeproTech, London, GB), ciliary neurotrophic factor (CNTF; 10 ng/mL; PeproTech) and forskolin (10 µmol/L).

Since primary cells are at the most capable of a few cell divisions, a descrption of the passaging is not necessary. RGCs were freshly prepared for each experiment by Professor T. Claudepierre (Augenklinik, Universität Leipzig, Germany). The cells were kept for transport (not longer than 1 h) in CO_2 independent medium D-PBS (Gibco/Invitrogen, Invitrogen) supplemented with 30% FBS to block trypsin used for detaching the cells. Afterwards, the cell suspension was centrifuged 10 min at 800 rpm. The supernatant D-PBS was aspirated off the pellet and RGCs were redistributed in 1 mL of growth medium under sterile conditions. RGCs were seeded with a cell density of 110 - 200 cells/mm^2 on tBLs coated with laminins (LN-111 and LN-211).

C.2.1. Substrate coating for neuronal growth

Materials:

- 2 small Petri dishes with tBLs (cf. section 3.4)
- 2 mL centrifuge tube (safe-lock, Eppendorf), 10 mL pipettes, 1 mL pipettor, sterile pipette tips (all VWR)
- PBS (Gibco/Invitrogen, 18912-014)
- For NG108s and RGCs: Thaw 12 µL laminin-1 (LN-111) (sc-29012, 1.64 mg/mL, Santa Cruz Biotechnology, Santa Cruz, CA)
- For RGCs only: Thaw 40 µL laminin-2 (LN-211) (CC085, 250 µg/mL, Chemicon, Millipore, Billerica, MA)

Method:

1. Sterilize Petri dishes with tBL with C_2H_5OH.
2. Suck off carefully the Millipore water taking care to keep a thin water film to maintain the bilayer intact.
3. Carefully flush the Petri dishes twice with PBS and set aside.
4. Fill 2 mL of PBS in centrifuge tube, add LN-111 and LN-211 (only for RGCs) and mix by sucking the solution in and out with a pipette.
5. Suck off very careful excess PBS (but still leave a thin PBS film) and pool $\sim$1 mL LN/PBS mixture over tBL.
6. Label dishes (tBL type, coating protein, date, initials) and incubate 1 h at 37 °C.
7. Carefully aspirate LN/PBS off and rinse tBL twice with 1 mL PBS.
8. Immediately add cell suspension, label dishes and incubate for 1 h to allow settling and adhesion of the neurons.
9. Finally, add 5 - 8 ml of culture medium slowly (dropwise) to the Petri dish and incubate at 37 °C and 5 % CO_2, 95 % humidity.

The resulting concentrations of ECM-coating proteins were 1.42 µg/cm^2 for LN-111 and 0.71 µg /cm^2 for LN-211, respectively.

Acknowledgment

As this thesis is drawing to a close, I would like to thank many people for their help, support, encouragement and making life wonderful.

In the first place, I would like to express my gratitude to my supervisor Josef Käs for his encouragement and support. Without him, none of the work would have been possible. He shared his enthusiasm, taught us to always keep in mind the "big picture" and many other important things for life. Furthermore, I want to thank him for encouraging me in times of blind alleys. His inspiration always supported me in finding a back door and discovering unexpected worlds.

Although some time has passed, I want to thank two former lab members who accompanied my way in the first years of my PhD thesis. My deepest thanks go to Carsten Selle, the former head of the "lipid group", for all his support, for performing the MD simulations of the DODAB-water system and for sharing the passion for liquid water as well as Florian Rückerl for discussing and having a great time in lab and office.

I also want to acknowledge the support I received by people from other departments of the Universität Leipzig regarding the analytical characterization of the DODAX lipids used in the first part of this work: Jörg Lenzner and Matthias Findeisen for the EDX and NMR spectroscopic measurements, respectively, as well as Jürgen Schiller for the MALDI-TOF experiments.

Concerning my second project, I want to express my gratitude to Christoph Naumann and Dan Minner (both Indiana University-Perdue University Indianapolis, IN) who introduced me in the Langmuir/Blodgett-Langmuir/Schäfer technique, provided linker molecules for cell adhesion and most importantly for Christoph's support and cooperation in the project of modulating neuronal growth by tethered lipid membranes. This directly brings me to Rainer Jordan (TU Dresden) and Robert Luxenhofer (Julius-Maximilians-Universiät Würzburg) who I want to thank for the synthesis of the lipopolymer for the tethered bilayers. The last piece of the puzzle are the neurons, particularly the primary RGCs, which were kindly provided by Thomas Claudepierre (Universität Leipzig). My heartfelt thanks for the numerous hours of dissecting cells for me, but also

for answering so many questions about cell biology and his fruitful teamwork in our joint publication.

After acknowledging all the support I received from external scientists I want to go over to the great PWM crew. A very warm thank goes to Elke Westphal, Undine Dietrich, Bernd Kohlstrunk and Claudia Brück who solid as a rock keep the lab running and help with advice in many kinds of problems. Then I want to thank Melanie Knorr, Tobias Kießling and Philipp Rauch for their help and advice with Matlab and together with all the other members of the "neuro group" for helpful discussions and especially Paul Heine, but also Melanie, Tobi, Anatol Fritsch, Nadine Große and Jessica Schulz for valuable proofreading.

Special thanks to my dear office mates Susi, Steve and lately also Erik and Saddam for the good time we spent together. Beyond that I have to say that it was a great experience to graduate in the Käs lab: thanks to Melanie, Tobi, Roland, Anatol, Pico, Dan, Franzi, Silke, Valentina, Thomas, David, Jörg, Carsten, Chris, Paul, Sebastian, the "associated member" Christina and the former Käslabbers Claudia and Karla, but also the newer guys.

Beside the biophysicists, I also want to thank the Doppelkopf girls Jessica, Nadine, Eva, Karla, Miriam and Melanie for after work distraction and "inter-scientific" exchange as well as Magdalena for sharing a garden plot with me – growing green can be sometimes as exciting as science.

Most importantly, I want to thank my family and Kai Dietze. Thank you for loving, supporting and encouraging me, for your understanding and for sometimes *not* asking when I will finish.

Curriculum vitae

Personal Information

Lydia Woiterski

Born July 30th, 1980, Prenzlau, Germany

Education

Jan. 2010 - Jul. 2013	Research associate (PhD Thesis), Universität Leipzig, Associated member of the Graduate School "Interdisciplinary Approaches in Cellular Neuroscience "
Aug. 2007 - Dec. 2009	Full member of the Graduate School "Interdisciplinary Approaches in Cellular Neuroscience" (PhD Thesis)
Oct. 2005 - Jul. 2007	Research associate (PhD Thesis), Universität Leipzig
Aug. 2005	Master of Science, Universität Leipzig
Oct. 2000 - Aug. 2005	International Physics Studies Program, Universität Leipzig
Oct. 2002 - Jul. 2003	Graduate studies, Universidad de Granada, Spain
Jun. 2000	Abitur, Carl-Friedrich-Gauß-Gymnasium, Frankfurt (Oder), Germany

Teaching

2005 - 2009	Supervision of the undergraduate laboratory course Physics for Veterinarians